

**AN EXPERIMENTAL AND NUMERICAL STUDY
ON INTERFACIAL CONVECTIVE HEAT
TRANSFER COEFFICIENT AND THERMAL
DISPERSION CONDUCTIVITY OF A PERIODIC
POROUS MEDIUM UNDER MIXED
CONVECTION HEAT TRANSFER**

**A Thesis Submitted to
the Graduate School of Engineering and Science of
İzmir Institute of Technology
in Partial Fulfillment of the Requirements for the Degree of**

DOCTOR OF PHILOSOPHY

in Mechanical Engineering

**by
Hasan ÇELİK**

**July, 2017
İZMİR**

We approve the thesis of **Hasan ÇELİK**

Examining Committee Members:

Assist. Prof. Dr. Ünver ÖZKOL

Department of Mechanical Engineering, İzmir Institute of Technology

Prof. Dr. Aytunç EREK

Department of Mechanical Engineering, Dokuz Eylül University

Assoc. Prof. Dr. Erdal ÇETKİN

Department of Mechanical Engineering, İzmir Institute of Technology

Assist. Prof. Dr. Ziya Haktan KARADENİZ

Department of Mechanical Engineering, İzmir Katip Çelebi University

Assist. Prof. Dr. Murat BARIŞIK

Department of Mechanical Engineering, İzmir Institute of Technology

25 July 2017

Assist. Prof. Dr. Ünver ÖZKOL

Supervisor, Department of Mechanical Engineering, İzmir Institute of Technology

Assoc. Prof. Dr. Moghtada MOBEDI

Co-Supervisor, Faculty of Engineering, Shizuoka University

Prof. Dr. Metin TANOĞLU

Head of the Department of Mechanical Engineering

Prof. Dr. Aysun SOFUOĞLU

Dean of the Graduate School of Engineering and Sciences

ACKNOWLEDGMENTS

Firstly, I would like to thank to my advisers, Assist. Prof. Dr. Ünver ÖZKOL and Assoc. Prof. Dr. Moghtada MOBEDI, for their endless support through my PhD study. Without the opportunities that they provided to me during this thesis, this study may not be possible. Also, I need to acknowledge my sincere gratitude to my PhD Thesis Jury Members, Prof. Dr. Aytunç EREK and Assoc. Dr. Erdal ÇETKİN for sharing their experience and knowledge with me. I am also very thankful to Assist. Prof. Dr. Murat BARIŞIK for his endless support.

I am very thankful to the faculty of the Department of Mechanical Engineering as Prof. Dr. Akira NAKAYAMA, Prof. Dr. Fujishiro KUWAHARA and Assist. Prof. Dr. Yoshiko SANO for their advices for my PhD thesis during my stay in their laboratory. I also would like to give my sincere gratitude to Prof. Dr. Oronzio MANCA from Seconda Universita degli Studi di Napoli for his support.

It is impossible not to mention Tümcen ŞEN and Doğuş ZEREN who were always with me during lunch breaks. Thanks for making each day at IYTE more enjoyable.

I would like to thank to the “*legendary*” old team members of Fluid Mechanics Lab., Egemen AĞAKAY for always having time for a cup of coffee whenever I knocked his door; Ömer Buğra KANARGI for his endless computing source support; Assist. Prof. Dr. Sercan ACARER, Dr. Orçun KOR, Ali AKÇA and Serdar MALAK for their valuable time to listen my tough times during my stay in Japan.

I am honored to acknowledge the Scientific and Technological Research Council of Turkey (TUBITAK) for their support under 2214/A fellowship for my studies.

Last, I would like to thank to my family for their endless support and being part of my journey.

ABSTRACT

AN EXPERIMENTAL AND NUMERICAL STUDY ON INTERFACIAL CONVECTIVE HEAT TRANSFER COEFFICIENT AND THERMAL DISPERSION CONDUCTIVITY OF A PERIODIC POROUS MEDIUM UNDER MIXED CONVECTION HEAT TRANSFER

The need on effective heat transfer enhancement has been increasing day by day. Because of that, researchers/engineers who work on heat transfer are required to obtain new techniques to address raising accumulation of heat transfer. Heat transfer can be enhanced by active and passive methods and passive methods are mostly chosen, as no external power input is required. Porous media is one of the most popular passive heat transfer techniques. Porous media can be divided into periodic and stochastic structures. In this thesis, the analysis of heat and fluid flow in 2D periodic structure and 3D aluminum and ceramic foam structures under mixed and forced convection heat transfer are studied. The governing equations are solved at pore scale and volume-averaged transport parameters as permeability, inertia coefficient, interfacial heat transfer coefficient and thermal dispersion are obtained by using volume averaging of the obtained pore scale velocity, pressure and temperature. For the change of periodic structure, the interfacial heat transfer coefficient and thermal dispersion with respect to Reynolds, Richardson and porosity under mixed convection are studied probably for the first time in literature. For foam structure, the changes of permeability, inertia coefficient, interfacial heat transfer coefficient and thermal dispersion with respect to Re are discussed. The determination of thermal dispersion by using tomography method is probably reported for the first time. For 2D periodic structures, the interfacial convective heat transfer coefficient successfully found while for the thermal dispersion conductivity the Volume Averaging Technique fails for high Richardson numbers under mixed convection. Based on good agreement between the computational values of this study and reported correlation in literature, it is observed that the use of micro-tomography technique for determination of volume-averaged transport parameters yield satisfactory results if properly used. The comprehensive methods for inspection, verification and validation of the obtained computational results for 3D digitally generated foam are suggested.

ÖZET

KARIŞIK TAŞINIMLA ISI TRANSFERİNE MARUZ KALAN PERİYODİK GÖZENEKLİ BİR YAPININ ARAYÜZEY ISI TAŞINIM KATSAYISI VE ISIL DİSPERSİYON İLETİMİ ÜZERİNDE DENEYSEL VE SAYISAL BİR ÇALIŞMA

Teknolojinin ilerlemesiyle beraber, etkin ısı transferi artırımına olan ihtiyaç günden güne artmaktadır. Araştırmacıların/mühendislerin, gelişen teknoloji ile beraber ihtiyacı artan etkin ısı transferi artırımını yapabilmesi için aktif ve pasif olmak üzere iki ana yöntem bulunmaktadır. Gözenekli ortam son zamanlarda popülerliği artan bir pasif ısı transferi yöntemidir. Gözenekli ortamlar periyodik ve stokastik olmak üzere iki ana başlık altında toplanabilir. Bu çalışmada, 2-boyutlu periyodik ve 3-boyutlu alüminyum ve seramik köpük yapılar, zorlanmış ve karışık taşınım altında incelenmiştir. Yürütücü denklemler, gözenek seviyesinde çözülmüş ve elde edilen hız, basınç ve sıcaklık dağılımı kullanılarak, Hacimsel Ortalama Yöntemi ile geçirgenlik, atalet ve arayüzey ısı taşınım katsayısı ile ısı dispersiyon gibi hacimsel ortalama taşınım parametreleri bulunmuştur. Periyodik yapılar, değişik gözeneklilik, Reynolds ve Richardson sayısı değerlerinde, karışık taşınım için, açık literatürde ilk defa incelenmiştir. Köpük yapılar için ise, geçirgenlik, atalet katsayısı ve arayüzey ısı taşınım katsayısı ile ısı dispersiyonun, zorlanmış ve karışık taşınım altında Reynolds sayısı ile değişimi incelenmiştir. Isıl dispersiyon, bilgisayarlı mikro-tomografi kullanılarak literatürde ilk defa elde edilmiştir. 2-boyutlu periyodik yapılarda, arayüzey ısı taşınım katsayısı başarı ile elde edilmiş, ancak ısı dispersiyon hesaplarında Hacimsel Ortalama Yöntemi'nin karışık taşınım altında ve yüksek Richardson değerlerinde istenilen gibi yanıt vermediği görülmüştür. Literatürde yer alan zorlanmış taşınım çalışmaları ile yapılan karşılaştırma sonucunda, bu çalışmanın literatürdeki sonuçları ile iyi bir uyum gösterdiği gözlemlenmiştir. Bu çalışma göstermiştir ki, Hacimsel Ortalama Yöntemi doğru olarak kullanıldığında, mikro-tomografi yöntemi ile hacimsel ortalama taşınım parametreleri başarı ile elde edilebilmektedir. Bilgisayar ortamında mikro-tomografi yöntemi ile elde edilen 3-boyutlu model ve sayısal çözüm sonucu elde edilen yürütücü denklem sonuçlarının incelenmesi, doğruluğunun ve geçerliliğinin ispatlanması için takip edilmesi gereken yol hakkında, bu çalışmadan elde edilen sonuçlar yorumlanarak gelecek çalışmalara fikir verilmesi hedeflenmiştir.

TABLE OF CONTENTS

CHAPTER 1. INTRODUCTION	1
1.1. The Aim of Study	5
1.2. Innovation of the Present Thesis	7
1.3. The Outline of Thesis	8
CHAPTER 2. FUNDAMENTAL CONCEPTS	10
2.1. Porosity	10
2.2. Permeability	10
2.3. Darcy Number	11
2.4. Inertia Coefficient	11
2.5. Stagnant Thermal Conductivity	11
2.6. Interfacial Convective Heat Transfer Coefficient	13
2.7. Tortuosity	13
2.8. Thermal Dispersion	13
2.9. Boussinesq Approximation	14
2.10. Heat and Fluid Flow in Porous Media based on Volume Average Technique	15
2.10.1. Pore Scale Method	15
2.10.2. Volume – Averaged Method	16
2.11. Derivation of General Form of Volume-Averaged Equations	17
2.11.1. Volume – Averaged Conservation of Mass Equation	17
2.11.2. Volume – Averaged Conservation of Momentum Equation	18
2.11.3. Volume – Averaged Conservation of Energy Equation	19
2.12. Determination of Volume-Averaged Transport Parameters	21
2.12.1. Thermal Dispersion	21
2.13. Some Classical Theories for the Analysis of Heat and Fluid Flow in Porous Media	22
2.13.1. Darcy’s Law	22
2.13.2. Brinkman – Extended Darcy’s Law	23
2.13.3. Forchheimer – Brinkman Extended Darcy’s Law	23

CHAPTER 3. LITERATURE REVIEW	25
3.1. Literature Review on 2D Periodic Structure	25
3.1.1. Interfacial Convective Heat Transfer Coefficient.....	25
3.1.2. Thermal Dispersion.....	31
3.2. Literature Review on Foam Structures	39
3.2.1. Permeability and Inertia Coefficient.....	39
3.2.2. Interfacial Convective Heat Transfer Coefficient.....	44
3.2.3. Thermal Dispersion.....	45
 CHAPTER 4. STUDIED POROUS MEDIA	 48
4.1. Studied Porous Media.....	48
4.1.1. 2D Periodic Structure.....	48
4.1.2. Foam Structure.....	49
 CHAPTER 5. GOVERNING EQUATIONS AND BOUNDARY CONDITIONS.....	 55
5.1. 2D Periodic Porous Structure	55
5.1.1. Governing Equation and Boundary Conditions for Mixed Convection Heat Transfer in 2D Periodic Structure	56
5.1.2. Determination of Interfacial Heat Transfer Coefficient	58
5.1.3. Determination of Thermal Dispersion	60
5.2. 3D Foam Structure	61
5.2.1. The Governing Equations and the Boundary Conditions for Heat and Fluid Flow in Foam Structures.....	61
5.2.2. Determination of Permeability.....	62
5.2.3. Determination of Interfacial Convective Heat Transfer Coefficient in Foam	64
5.2.4. Determination of Thermal Dispersion	65
 CHAPTER 6. COMPUTATIONAL DETAILS	 68
6.1. 2D Periodic Structure	68
6.2. 3D Foam Structure	69
 CHAPTER 7. RESULTS AND DISCUSSION.....	 75
7.1. 2D Periodic Structure	75

7.1.1. Interfacial Convective Heat Transfer Coefficient.....	75
7.1.2. Thermal Dispersion.....	86
7.2. 3D Foam Structure: Forced Convection.....	93
7.2.1. Permeability and Inertia Coefficient.....	93
7.2.2. Interfacial Convective Heat Transfer Coefficient.....	100
7.2.3. Thermal Dispersion.....	106
7.3. 3D Foam Structure: Mixed Convection.....	112
CHAPTER 8. CONCLUSION	115
REFERENCES	121
APPENDIX A. DERIVATION OF SLATTERY'S THEOREM	125

LIST OF FIGURES

<u>Figure</u>	<u>Page</u>
Figure 1.1. A sample of porous media.....	1
Figure 1.2. A sample of stochastic and periodic structures (Source: Lu et al., 2013); a) open-cell foam (stochastic), b) closed-cell foam (stochastic), c) tetrahedral lattice (periodic), d) pyramidal lattice (periodic), e) Kagome lattice (periodic), f) diamond textile, g) diamond collinear lattice (periodic), h) square collinear lattice (periodic), i) triangular corrugation (periodic), j) 2D cellular material (periodic), k) 2D cellular material (periodic).....	2
Figure 1.3. Two main approaches employed for heat and fluid flow simulations in porous media; a) Pore Scale Method (PSM), b) Volume-Averaged Method (VAM).....	3
Figure 1.4. Two main approaches for analyzing heat and fluid flow in porous media, a) Local thermal non-equilibrium (LTNE), b) Local thermal equilibrium	5
Figure 2.1. An appropriate selection of REV	16
Figure 3.1. The considered domain in the study of Kuwahara et al. (2001) (Source: Kuwahara et al., 2001)	26
Figure 3.2. The considered domain in the study of Nakayama et al. (2002) (Source: Nakayama et al., 2002).....	27
Figure 3.3. The study of Gamrat et al. (2008) (Source: Gamrat et al., 2008), a) the considered domain, b) the comparison of their results.....	28
Figure 3.4. The considered domain in the study of Yang et al. (2010) (Source: Yang et al., 2010).....	28
Figure 3.5. The considered domain in the study of Pathak and Ghiaasiaan (2011) (Source: Pathak and Ghiaasiaan, 2011).....	29
Figure 3.6. The considered domain in the study of Teruel and Diaz (2013) (Source: Teruel and Diaz, 2013).....	29
Figure 3.7. The study of Ozgumus and Mobedi (2015) (Source: Ozgumus and Mobedi, 2015), a) the considered domain in the study, b) the comparison of their study with the reported studies	30
Figure 3.8. The considered domain in the study of Vu et al. (2014) (Source: Vu et al., 2014).....	31

Figure 3.9. The study of Kuwahara et al. (1996) (Source: Kuwahara et al., 1996) , a) the considered domain, b) the comparison of their results with the reported studies.....	32
Figure 3.10. The comparison of the study of Kuwahara and Nakayama (1999) with the literature (Source: Kuwahara and Nakayama, 1999).....	33
Figure 3.11. The comparison of the study of Nakayama and Kuwahara (2005) with the study of Kuwahara and Nakayama (1999) (Source: Nakayama and Kuwahara, 2005).....	33
Figure 3.12. The considered domains in the study of Saada et al. (2006) (Source: Saada et al., 2006)	34
Figure 3.13. The considered domain in the study of Pedras and de Lamos (2008), (Source: Pedras and de Lamos, 2008).....	35
Figure 3.14. The considered domain in the study of Xu et al. (2010) (Source: Xu et al., 2010)	36
Figure 3.15. The study of Alshare et al. (2010) (Source: Alshare et al., 2010), a) the considered domain, b) the comparison of their study	36
Figure 3.16. The solution domain in the study of Yang and Nakayama (2010) (Source: Yang and Nakayama, 2010).....	37
Figure 3.17. The considered solution in the study of Jeong et al. (2011) (Source: Jeong et al., 2011)	39
Figure 3.18. The foam structure in the study of Petrasch et al. (2008), (Source: Petrasch et al., 2008)	40
Figure 3.19. 2D cut of the foam structure in the study of Magnico (2009) (Source: Magnico, 2009).....	40
Figure 3.20. The considered domain in the study of Akolkar and Petrasch (2012) (Source: Akolkar and Petrasch, 2012)	41
Figure 3.21. The considered geometries in the study of Ranut et al. (2014), (Source: Ranut et al., 2014).....	41
Figure 3.22. The considered samples in the study of Della Torre et al. (2014); a) ideal foam model, b) real foam structure (Source: Della Torre et al., 2014).....	42
Figure 3.23. The considered sample in the study of Zafari et al. (2015), (Source: Zafari et al., 2015)	42
Figure 3.24. The considered samples in the study of Diani et al. (2015), (Source: Diani et al., 2015)	43

Figure 3.25. The considered samples in the study of Ambrosio et al. (2016), (Source: Ambrosio et al., 2016)	44
Figure 3.26. Considered model in the study of Zhang et al. (2015), (Source: Zhang et al., 2015)	46
Figure 3.27. Considered experimental setup in the study of Calmidi and Mahajan (2000), (Source: Calmidi and Mahajan, 2000)	46
Figure 3.28. Considered experimental setup in the study of Vijay et al. (2015), (Source: Vijay et al., 2015).....	47
Figure 4.1. The considered and studied domain when a) $\varepsilon = 0.96$, b) $\varepsilon = 0.51$	49
Figure 4.2. Structural properties of a foam, a) Scanning electron microscope (SEM) image of a foam (Taheri, 2015), b) the same structural properties of a foam built by using micro-tomography technique in the present study	50
Figure 4.3. The metal foam samples considered in this study; a) 10 PPI aluminum foam, b) 20 PPI aluminum foam, c) 20 PPI ceramic foam, d) 40 PPI ceramic foam. The images on the left were taken after scanning step while the images on the right shows after threshold step.....	52
Figure 4.4. The considered 10 PPI and 20 PPI pore density metal foams a) the real structure, b) the domain generated in computer environment (20 PPI)	53
Figure 4.5. The foam samples generated in computer environment; a) 10 PPI aluminum foam, b) 20 PPI aluminum foam, c) 20 PPI ceramic foam, d) 40 PPI ceramic foam.....	53
Figure 4.6. The domain generated in computer environment; a) 10 PPI metal foam, b) 20 PPI metal foam	54
Figure 5.1. A view of the computational domain with boundary conditions	58
Figure 5.2. The considered domain a) with dummy inlet and outlet regions, and boundary conditions (O indicates the origin point), b) dummy regions in each direction.....	62
Figure 5.3. Determination of pore diameter by considering three randomly selected cells. Red line shows cell diameter, blue line shows pore diameter	64
Figure 5.4. Determination of volume-averaged parameters by considering volumes through the domain a) interfacial convective heat transfer coefficient and longitudinal thermal dispersion by 5 volumes, b) determination of transverse thermal dispersion by 5 volumes, c) interfacial convective heat transfer coefficient and longitudinal thermal dispersion by 20 volumes, d)	

determination of transverse thermal dispersion by 20 volumes, e) the considered solid boundary condition for interfacial convective heat transfer coefficient and longitudinal thermal dispersion, f) the considered solid boundary condition for transverse thermal dispersion	66
Figure 6.1. Grid independence study for $Ri = 0.1 - Re = 100$, and $Ri = 10 - Re = 500$ when $\epsilon = 0.96$	69
Figure 6.2. The general flow chart of the code written for evaluating volume averaged transport parameters	71
Figure 6.3. The flow chart considered in the code to calculate permeability and inertia coefficient.....	71
Figure 6.4. The flow chart considered in the code to calculate interfacial convective heat transfer coefficient and longitudinal thermal dispersion.....	72
Figure 6.5. The flow chart considered in the code to calculate transverse thermal dispersion	72
Figure 6.6. Validation of number of image and grids for $Re = 600$; a) the change of permeability in z direction respect to number of images in flow direction, b) the change of permeability in z direction respect to grid number, c) b) the change of inertia coefficient in z direction respect to grid number.....	73
Figure 6.7. The change of the generated structure of aluminum foam with $PPI=20$ with number of grids for the surface with $y = 3L/2$ (black is solid region while gray represents void).	73
Figure 6.8. The change of volume-averaged transport parameters with cell number for 20 PPI aluminum foam, a) interfacial convective heat transfer coefficient, b) effective thermal conductivity.....	74
Figure 7.1. Validation of the obtained results, a) the comparison of present study with reported results for average interfacial Nusselt number of fully developed forced convection, b) comparison of average interfacial Nusselt number with correlation suggested by Ozgumus and Mobedi (2015) when $Ri = 0.0001$ and $Re = 100$	76
Figure 7.2. Streamlines and temperature distribution in porous media with $\epsilon = 0.96$ and $Ri = 0.01$, a) $Re = 100$, b) $Re = 500$	78
Figure 7.3. Streamlines and temperature distribution in porous media with $\epsilon = 0.96$ and $Ri = 10$, a) $Re = 100$, b) $Re = 500$	79

Figure 7.4. Streamlines and temperature distribution in porous media with $\varepsilon = 0.51$ and $Ri = 0.01$, a) $Re = 100$, b) $Re = 500$	80
Figure 7.5. Streamlines and temperature distribution in porous media with $\varepsilon = 0.51$ and $Ri = 10$, a) $Re = 100$, b) $Re = 500$	82
Figure 7.6. The change of local interfacial Nusselt number distribution with porosity, Re and Ri numbers a) $Ri = 0.01$, $\varepsilon = 0.96$, b) $Ri = 10$, $\varepsilon = 0.96$, c) $Ri = 0.01$, $\varepsilon = 0.51$, d) $Ri = 10$, $\varepsilon = 0.51$	83
Figure 7.7. The local interfacial Nusselt number between forced and mixed convection for two values of ε , Re and Ri numbers a) $Ri = 0.01$, $\varepsilon = 0.96$, b) $Ri = 10$, $\varepsilon = 0.96$, c) $Ri = 0.01$, $\varepsilon = 0.51$, d) $Ri = 10$, $\varepsilon = 0.51$	84
Figure 7.8. The change of mean interfacial Nusselt number distribution with porosity and Ri number a) $Re = 100$, b) $Re = 500$	86
Figure 7.9. The change of mean interfacial Nusselt number distribution with Ri and Re numbers a) $\varepsilon = 0.51$, b) $\varepsilon = 0.96$	86
Figure 7.10. The change of the ratio of stagnant, dispersion and effective thermal conductivity to thermal conductivity of the fluid, respectively, with cell number when, a) $Ri = 0.1$, $Re = 100$, b) $Ri = 4$, $Re = 100$, c) $Ri = 0.1$, $Re = 500$, d) $Ri = 4$, $Re = 500$	88
Figure 7.11. The third and 8th rods for the middle of their cells considered for explanation of unexpected behavior of thermal dispersion. Red squares indicate solid rods.	89
Figure 7.12. The change of dimensionless velocity and temperature, dimensionless deviation and the multiplication of the deviation when $Ri = 0.1$, $Re = 500$ for a, b, c) 3th rod, d, e, f) 8 th rod.....	90
Figure 7.13. The change of dimensionless velocity and temperature, dimensionless deviation and the multiplication of the deviation when $Ri = 4$, $Re = 500$ for a, b, c) 3th rod, d, e, f) 8 th rod	91
Figure 7.14. The schematic velocity profiles inside a channel when a) $Ri = 0.1$ and pore scale analysis, b) $Ri = 0.1$ and volume-averaged analysis, c) $Ri = 4$ and pore scale analysis, d) b) $Ri = 4$ and volume-averaged analysis.....	94
Figure 7.15. The change of velocity contour when the flow is in the perpendicular direction to the page, the mid-section slice of the metal foam with 20 PPI, a) $Re = 0.01$, b) $Re = 12$, c) $Re = 26$, d) $Re = 600$	94

Figure 7.16. The change of v velocity component in flow direction though the channel of metal foam with Re = 600 for a) 10 PPI, b) 20 PPI.....	95
Figure 7.17. The change of pressure though the channel of metal foam with Re = 600 for a) 10 PPI, b) 20 PPI.....	96
Figure 7.18. Pathlines inside the computational domain when Re = 600; a) 10 PPI, b) 20 PPI.....	97
Figure 7.19. The change of dimensionless pressure gradient in x, y and z directions with respect to Re number for a) 10 PPI, b) 20 PPI.....	98
Figure 7.20. Comparison of the present study with the reported studies in literature, a) permeability 10 PPI, b) permeability 20 PPI, c) inertia coefficient 10 PPI, d) inertia coefficient 20 PPI	99
Figure 7.21. The change of temperature in flow direction though the channel of metal foam when Re = 600 for a) 10 PPI, b) 20 PPI	101
Figure 7.22. The temperature profiles on the line at the mid-point for 20 PPI metal foam; a) the considered line to plot the velocity profile, b) the temperature profile at the mid-plane for Re = 120, b) the temperature profile at the mid-plane for Re = 600.....	102
Figure 7.23. A sample of temperature distribution along the flow a) the position of the through the flow direction, b) Re=120 c) Re = 600.....	102
Figure 7.24. The change of interfacial Nu number with number of volume in flow direction (The dotted lines shows average values)	103
Figure 7.25. The comparison of interfacial Nu number for the present study with the study of Calmidi and Mahajan (2000) for different Re numbers for a) 10 PPI aluminum metal foam, b) 20 PPI aluminum metal foam.....	105
Figure7.26. The change of the interfacial heat transfer coefficient of 10 and 20 PPI aluminum foams with pore scale Re number.....	105
Figure 7.27. For all the samples considered in this study for different Re numbers a) the change of interfacial convective heat transfer coefficient, b) the change of interfacial Nusselt number	106
Figure 7.28. Directions of heat and fluid flow in a porous media a) longitudinal direction , b) transverse direction.....	107
Figure 7.29. The comparison of present study with the study of Zhang et al. (2015) for different Re numbers for a) k_{dis} / k_f of 10 PPI aluminum metal, b) k_{dis} / k_f of	

20 PPI aluminum metal, c) k_{eff} / k_f of 10 PPI aluminum metal foam, d)	
k_{eff} / k_f of 20 PPI aluminum metal foam	109
Figure 7.30. The change of a) k_{dis} / k_f , b) k_{eff} / k_f , with Re number for ceramic foam samples.....	109
Figure 7.31. Transverse thermal dispersion compared with reported study of Zhang et al. (2015) for 20 PPI aluminum foam, a) k_{dis} / k_f , b) k_{eff} / k_f	111
Figure 7.32. Transverse thermal dispersion with Re number for 20 and 40 ceramic foam samples, a) k_{dis} / k_f , b) k_{eff} / k_f	111
Figure 7.33. The domain considered in mixed convection case.....	113
Figure 7.34. The change of Nu number with Ri number when Re = 30; a) 10 PPI aluminum foam, b) 20 PPI aluminum foam.....	113
Figure 7.35. The change of effective thermal conductivity when Re = 30; a) 10 PPI aluminum foam, Ri = 8.3, b) 20 PPI aluminum foam, Ri = 1.4	113
Figure 7.36. The change velocity and temperature at the mid of the foam when Re = 30, 10 PPI aluminum foam and Ri = 8.3, a) velocity profiles, b) temperature profiles	114

LIST OF TABLES

<u>Table</u>	<u>Page</u>
Table 4.1. The values of structural properties of the considered metal foam samples in this study in x, y and z directions	54
Table 7.1. The properties obtained from 3D model generated in computer environment and the obtained results	99

LIST OF SYMBOLS

a	A dimensionless coefficient defined in Eq. (3.1)
A	Area [m^2]
A_{sf}	Interfacial area between solid and fluid phases [m^2]
A_{ss}	Specific solid – fluid interface area [m^2/m^3]
A^*	Aspect ratio
b	A dimensionless coefficient defined in Eq. (3.1)
C	Forchheimer coefficient
C_p	Specific heat at constant pressure [J/kgK]
D	Dimension of the solid particle in both x and y directions
g	Gravitational acceleration [m/s^2]
Gr	Grashof number
H	Distance between the center points of each square blocks
h_{int}	Local interfacial convective heat transfer coefficient [$\text{W}/\text{m}^2\text{K}$]
k	Thermal conductivity [W/mK]
K	Permeability
L	Length [m]
\overline{Nu}	Average Interfacial Nusselt number
Nu_L	Local Interfacial Nusselt number
Nu_{Lc}	Contribution to Local Nusselt number
p	Pressure [Pa]
P	Dimensionless pressure
Pr	Prandtl number, ν/α
Re	Reynolds number
Ri	Richardson number
T	Temperature [K]
\vec{u}	Velocity vector
u	Velocity in x-direction [m/s]
v	Velocity in y-direction [m/s]

u^*	Dimensionless velocity in x-direction
v^*	Dimensionless velocity in y-direction;
V	Volume [m^3]
w	Width [m]
x,y	Dimensional axial and transverse directions [m]
X, Y	Dimensionless axial and transverse directions

Greek Symbols

α	Thermal diffusivity of the fluid [m^2/s]
β	Thermal expansion coefficient [$1/K$]
ε	Porosity
θ	Dimensionless temperature
μ	Dynamic viscosity [Pas]
ν	Kinematic viscosity [m^2/s]
Π	Dimensionless pressure
ρ	Density [kg/m^3]

Subscripts and Superscripts

dis	Dispersion
eff	Effective
f	Fluid
i	Inlet
int	Interface
L	Local
L_c	Local contribution
s	Solid
sf	Surface
tor	Tortuosity
x	Phase

CHAPTER 1

INTRODUCTION

The demand on efficient heat transfer enhancement techniques increases day by day as the functionality of electronic devices and cooling equipment continue to raise, which accumulates heat in the system distinguishably due to high heat flux rates. Because of that, innovative solutions should be offered and employed by thermal engineers/researchers to address this increase in heat flux rates and heat densities.

As any textbook in heat transfer field explains clearly, heat transfer enhancement methods can be combined under two main headings as active methods and passive methods. Active methods are accomplished by introducing energy with the help of external means such as fan, blower, surface vibration or electrostatic fields. Passive methods rely on extending interface area between solid and fluid phases by extending surface area by fins, coiled tubes or porous media.

The use of porous media may enhance heat transfer in the entire system significantly. Several reasons may be listed for enhancing of heat transfer by use of porous media:

- Firstly, porous media increases surface area and this results in an increase in total heat transfer.
- Secondly, porous media mix flow due to its tortuous path (see Figure 1.1) and create fluctuations.
- Thirdly, high conductive structure of the porous media increases stagnant heat conductivity (explained in Chapter 2) and total heat transfer.



Figure 1.1. A sample of porous media

Porous media can be classified into two groups as stochastic and periodic structure. The main difference between two structures comes from pore connectivity. Stochastic structures contain pores that are connected to each other and form an interconnected network while periodic structures do not contain any interconnected pores. Foam structures are well-known example for stochastic structures. Sandwich panels, lattice truss, textile or honeycomb can be given as an example of periodic structures. Sample of stochastic and periodic structures are given in Figure 1.2.

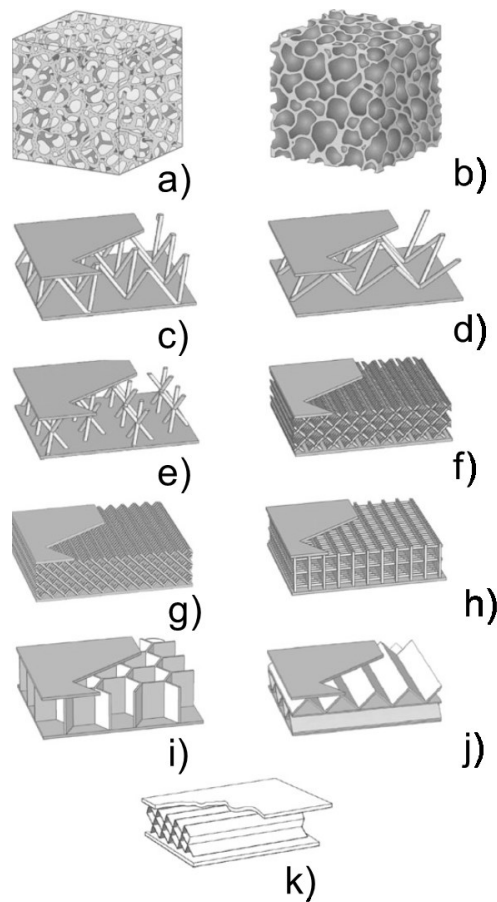


Figure 1.2. A sample of stochastic and periodic structures (Source: Lu et al., 2013); a) open-cell foam (stochastic), b) closed-cell foam (stochastic), c) tetrahedral lattice (periodic), d) pyramidal lattice (periodic), e) Kagome lattice (periodic), f) diamond textile, g) diamond collinear lattice (periodic), h) square collinear lattice (periodic), i) triangular corrugation (periodic), j) 2D cellular material (periodic), k) 2D cellular material (periodic)

Heat and fluid flow in porous media can be analyzed experimentally and theoretically. Many experimental studies have been performed on fluid flow in the porous media. The oldest study might be the study of Darcy (1856) who investigated pressure drop in the porous media. The number of experimental studies on heat transfer

in porous media is also large and many methods have been developed and suggested in literature. Those studies are summarized in the studies of Ozgumus et al. (2011), Ozgumus (2014), Ozgumus and Mobedi (2015), Ozgumus and Mobedi (2016).

Determination of velocity, pressure and temperature fields is a challenging process due to the fact that the flow is very complex in the pores, and the flow field is discontinuous between solid and fluid phases. For this reason, some approaches are required to overcome the difficulties in analyzing heat and fluid flow in porous media. A literature survey shows that two main approaches are employed for heat and fluid flow simulations in porous media. One of these approaches is known as Pore Scale Method (PSM). In this method, the governing equations for the considered problem are solved in pore scale with its every geometrical detail (see Figure 1.3(a)). Even though this method yields accurate results for velocity, temperature and pressure fields in the domain, its application may be very cumbersome and impractical due to substantial number of pores in porous media. To overcome this difficulty, Volume Averaged Method (VAM) is suggested by researchers. VAM is easier compared to PSM since the governing equations are integrated over a representative volume of porous media and volume-averaged governing equations (i.e., macroscopic governing equations) are obtained and discontinuity of phases is removed (see Figure 1.3(b)). Hence, the achieved governing equations can be solved for entire space. The main difficulty of VAM is that additional terms appears in the volume-averaged equations involving volume averaged transport parameters (i.e. permeability, inertia coefficient, ICHTC and thermal dispersion). The volume-averaged transport parameters are needed to be known to apply VAM. The volume-averaged method yields almost accurate results if the values of volume averaged transport parameters are reliable.



Figure 1.3. Two main approaches employed for heat and fluid flow simulations in porous media; a) Pore Scale Method (PSM), b) Volume-Averaged Method (VAM)

Convective heat transfer is a heat transfer mechanism between a solid structure and adjacent working fluid in motion. In convection heat transfer, conduction and fluid motion contributes each other. Faster fluid motion creates better convective heat transfer. Also, if there is no fluid motion, heat is transferred by pure conduction. This nature of the flow is widely used to classify convection heat transfer. If the flow is caused by external means such as fan, pump etc. convection is called forced convection. The buoyancy force, which is a result of density difference occurring due to temperature variation in fluid, can be neglected in forced convection. However, if buoyancy forces cause the motion of fluid, convection is then called natural convection. If the velocity by the flow of external means is small and by buoyancy forces are comparable, then this heat transfer regime is called mixed convection. Mixed convection occurs when the buoyance force considerably affects forced convection. In practice, it takes place (or intentionally appears) when the desired heat cannot be transferred due to reasons such as high heat generation (or heat flux) and/or low required pump/fan power (or small space). Examples for occurrence of mixed convection heat transfer are seen in electronic equipment cooling, in fuel assemblies of nuclear reactor cores, in solar collectors, etc. On the other hand, porous media (particularly high conductive porous media such as metal foams) becomes popular in heat transfer enhancement field due to high volumetric convective heat transfer coefficient and effective thermal conductivity. The analysis of mixed convection in heat transfer has taken the attention of researchers in recent years. Adequate knowledge on both mixed convection and heat transfer in porous media is essential to determine heat transfer rate in porous media under mixed convection.

In addition to PSM and VAM, there are two other approaches for analyzing heat and fluid flow in porous media. The first one is Local Thermal Non-Equilibrium (LTNE) in which there is significant difference between the local volume averaged temperature of solid phase and fluid phase. For the LTNE condition, the heat transfer at the interface of two phases can be modeled by using the interfacial convective heat transfer coefficient. Literature survey shows that studies on determination of interfacial convective heat transfer coefficient were mostly done considering periodic structures. The LTNE may occur in the porous media in initial stages of the flow, high speed flows or the flows inside of high permeable porous media when the interaction time between fluid and solid phases are not high enough and/or surface area between fluid and solid phases are small which limits to bring the temperature of the fluid and solid phases

close each other. For the LTNE condition, the heat transfer at the interface of two phases can be modeled by using the interfacial convective heat transfer coefficient. The method followed to obtain these volume-averaged parameters will be explained in the following chapters.

When the local volume averaged temperature of the solid and fluid phases is close to each other and temperature difference between solid and fluid phases is smaller than volume-averaged (i.e. macroscopic) temperature difference of the domain, Local Thermal Equilibrium (LTE) approach can be used. The use of LTE makes the governing equations simpler to solve. However, it requires that the existence of the LTE in the porous media must be ensured. It should be noted that, when the thermal interaction between the fluid and solid phases is highly effective, one energy equation for both fluid and solid phases can be solved.

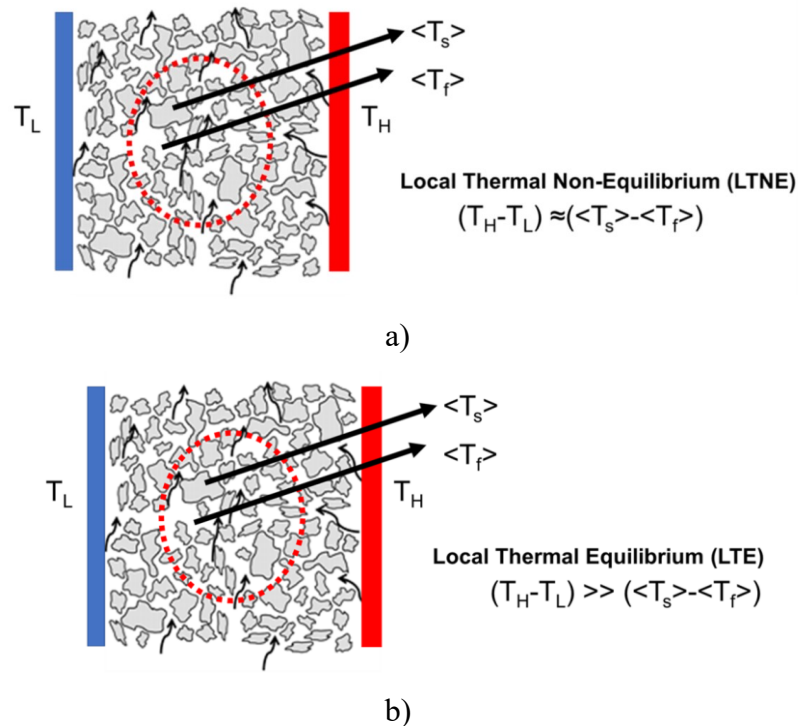


Figure 1.4. Two main approaches for analyzing heat and fluid flow in porous media, a) Local thermal non-equilibrium (LTNE), b) Local thermal equilibrium (LTE)

1.1. The Aim of Study

In this study, obtaining volume-averaged transport parameters that originate from averaging operations such as permeability, inertia coefficient, interfacial convective heat transfer coefficient (ICHTC) and thermal dispersion is aimed for two kinds of porous media:

- Periodic 2D structures
- 3D foam structures

The computational method is used to determine the above transport parameters. The periodic structure consists of solid bars with inline arrangement. As 3D foam structures, ceramic and aluminum foams between 10 and 40 PPI are used.

Literature survey showed that many studies on determination of the transport parameters have been done and reported in literature. However, to the best of our knowledge, number of studies on macroscopic parameters for mixed convection heat transfer in porous media does not exist. This is due to the fact that the dominant physics of the problem not only inertial or buoyant, but involves both effects. Luckily, permeability and inertia coefficients (for definitions see Chapter 2.2 and 2.4) strongly depend on the structure of the flow, hence the same permeability and inertia coefficient suggested for porous media under forced convection can be used also for mixed convection. However, new correlations for ICHTC and thermal dispersion are required. Literature survey showed that most of the studies have been performed under the assumption of LTE and the effect of the thermal dispersion is neglected. For the studies in which the LTNE model is used and the interfacial convective Nusselt number varies between a possible minimum and maximum values and no information was given about the real value of the interfacial convective heat transfer coefficient as discussions made on considering the dimensionless governing parameters. Briefly, a literature survey on local thermal non-equilibrium model of mixed convection heat transfer in porous media shows that there is no clear idea about the value of the interfacial mixed convective heat transfer coefficient. For this reason, it is aimed here to analyze mixed convection in pore scale and to determine not only the ICHTC but also to calculate thermal dispersion coefficients as well. Moreover, volume-averaged transport parameters are obtained for wide range of porosity, Richardson and Reynolds numbers and discussion is made on the change of these transport parameters with the governing parameters.

Foam structures are one of the trending topics in the last decade due to their promising heat enhancement capabilities. Recent studies on foam structures are mostly done for permeability and inertia coefficients. Since micro-tomography can resolve solid structures as small as $1 \mu m$, it is a promising technique to determine solid structure of irregular foam and therefore, it can be used in CFD studies aiming average heat transfer or thermal dispersion coefficients. Developments in computing technologies allow researchers to model foam structures as it is by using x-ray micro-

tomography technique. Very few studies are done for obtaining ICHTC using micro-tomography technique. As for the thermal dispersion, literature survey shows that there are no reported studies in open literature by using micro-tomography technique. Furthermore, some checks should be done for accuracy and correctness of the obtained numerical results. Many useful inspection methods for accuracy of the results are also suggested in this study.

1.2. Innovation of the Present Thesis

The innovation of the present study can be summarized as follow:

- Determination of ICHTC and thermal dispersion of 2D periodic structures for mixed convection is done for the first time. No equation or correlation has been reported in the literature.
- Present study is the first comprehensive study on the inspection of the results and methods used for determination of volume-averaged transport parameters of porous media by using x-ray micro-tomography method. Many methods for checking of the transport parameter values are proposed and explained in detail.
- As the best of our knowledge, no studies have been reported for calculation of thermal dispersion in longitudinal and transverse directions for stochastic porous media by using x-ray micro-tomography method. The only study on transverse thermal dispersion was done on the conduit model. Determination of thermal dispersion both in longitudinal and transverse directions have been described and discussed in the present study.
- As the best of our knowledge, for determination of ICHTC of stochastic structures, only one study has been reported which is not sufficient. In this study, the ICHTC of aluminum and ceramic foams, with pore density between 10 and 40 PPI is investigated.

- For the first time, anomaly (negative thermal dispersion coefficient) is reported for mixed convection. Many runs are performed to check the results for thermal dispersion coefficient for high values of Ri number and no mistake was caught. This study shows that VAM may not be a good approach for mixed convection under dominant buoyancy effect.
- Mixed convection heat transfer analysis for stochastic porous media is done for a geometry obtained by micro-tomography technique for the first time.

1.3. The Outline of Thesis

This thesis consists of eight chapters. Those are:

Chapter 1 is the introduction; the aim of study is explained in this chapter. The importance of the topic and the contribution of the present study to the literature are given in this chapter. Several fundamental concepts are explained briefly.

Chapter 2 covers fundamental concepts of porous media, the methods considered for calculating heat and fluid flow in porous media which are essential for the present study. Moreover, the general forms of the governing equations are derived and classical theories reported in the literature are given.

Chapter 3 reviews reported studies on determination of volume-averaged transport parameters. It is divided into two main parts as 2D periodic structure and foam structure. The material and method of each study are given.

Chapter 4 is concerned with the domain under investigation. The 2D geometry of the domain is given and considered representative elementary volume technique is explained. Following that, considered foam structures are explained and the details related to micro-tomography technique are given.

Chapter 5 gives information about boundary conditions and governing equations. The governing equations under the considered assumptions are reminded and expressed in dimensionless form. Following that, equations for evaluating volume-averaged transport parameters are derived.

Chapter 6 explains the solution technique in detail. Techniques for evaluating volume-averaged parameters are given. Details about numerical method are explained. The grid independency is shown for both 2D periodic and 3D foam structures.

In Chapter 7, the results of 2D periodic and 3D foam structures are given. Firstly, validation and checks needed are explained. Then, the results are discussed and compared with respect to governing parameters of the study. In the first and second parts of this chapter results for ICHTC of the periodic structure under mixed convection and in the third part result for permeability inertia coefficient, ICHTC and thermal dispersion of foam structure are given. The obtained results are plotted and described.

Chapter 8 is the conclusion and the summary of the study. A critique on the findings is done. Finally, areas for further research are identified.

CHAPTER 2

FUNDAMENTAL CONCEPTS

Fundamental concepts for heat and fluid flow analysis in a porous medium are given in this chapter. The chapter starts with the definitions of some key parameters for porous media. Then, Volume Averaging Theory is introduced. Some relations considered in Volume Averaging Theory are given and following that, general form of conservation of mass, momentum and energy equations is derived. Finally, some classical theories on heat and fluid flow in porous media are explained in detail.

2.1. Porosity

The ratio of fluid volume to the total volume of the porous medium is defined as porosity. The voids of the porous media may be connected to each other (open cell porous media) or may not have any connection with each other (closed cell porous media). Generally, heat and fluid flow is investigated in open cell porous media. For this reason, porosity is defined as the ratio of total volume of open voids to the total volume of the porous media. Sometimes, in addition to open voids, porous media may have some closed voids as well. In those cases, an effective porosity is defined where only the total connected volume to the total volume ratio is calculated. The porosity is mostly between 0.2 and 0.6 for natural media such as sand, soil or coal. However, this value approaches to 1 by man-made materials such as solid foams (Nield and Bejan, 2012).

2.2. Permeability

Permeability, K , is the ability of the porous medium to transfer fluid flow with ease. The structure of porous medium determines permeability. The increase in permeability provides a fluid flow like a clear channel. As seen on Eq. (2.1), if the permeability is high, working fluid of the system can flow easily. However, when K is small, the porous medium does not permit flow and thus, high pumping power is necessary for the flow. Estimation of permeability is done for each specific type of porous material. This

comes from the fact that each class of geometry has different structure and different characteristic length.

2.3. Darcy Number

Darcy number is a dimensionless number, which describes the relative effect of the permeability of the medium versus its cross-section area. Darcy number can be formulated as:

$$Da = \frac{K}{H^2} \quad (2.1)$$

where K is permeability and H represents the characteristic length of the considered system.

2.4. Inertia Coefficient

Inertia coefficient (also known as Forchheimer constant) is a dimensionless form-drag constant, which shows the inertial contribution. Darcy (1856) proved that flow in a uniform medium shows proportionality between flow rate and applied pressure difference. However, Forchheimer (1901) realized that by increasing the velocity, in addition to the friction, the collision at high speed of particles between each other and solid surface creates extra pressure drop and inertia becomes important. Therefore, a correction term should be considered to model heat and fluid flow at high speeds. Ward (1964) thought that inertia coefficient should be universal coefficient and its value can be taken as 0.55. However, later studies showed that inertia coefficient is strongly dependent to the nature of the porous medium and it should be obtained for each porous medium separately. Studies show that inertia coefficient can go as low as 0.05 to high as 0.3.

2.5. Stagnant Thermal Conductivity

Heat conduction through the porous medium depends on the structure of the domain and thermal conductivity of the fluid and solid phases strongly. Using the background on heat conduction and by assuming heat transfer between solid and fluid

phases occurs, the stagnant thermal conductivity can be calculated. Many correlations on the stagnant thermal conductivity have been reported in literature but three fundamental correlations are:

- *Series assumption:* In this assumption, thermal conductivities of fluid and solid phases are weighted arithmetically and the stagnant thermal conductivity of porous matrix can be obtained as:

$$k_{stg} = (1 - \varepsilon)k_s + \varepsilon k_f \quad (2.2)$$

- *Parallel Assumption:* Thermal conductivities of fluid and solid phases are weighted harmonic mean. Stagnant thermal conductivity can be calculated as follow:

$$\frac{1}{k_{stg}} = \frac{\varepsilon}{k_f} + \frac{1 - \varepsilon}{k_s} \quad (2.3)$$

- *Power Law Assumption:* In this assumption, stagnant thermal conductivity is calculated as weighted geometric mean of fluid and solid phases as:

$$k_{stg} = k_s^{1 - \varepsilon} k_f^\varepsilon \quad (2.4)$$

However, these relationships may not provide accurate results since the porous medium is much more complicated in nature and some correlation for metal foam and periodic structures are given in the literature. For instance, Calmidi and Mahajan (1999) reported stagnant thermal conductivity as follows:

$$k_{stg} = \left(\left(\frac{2}{\sqrt{3}} \right) \left(\frac{r \left(\frac{b}{L} \right)}{k_f + \left(1 + \frac{b}{L} \right) \frac{(k_s - k_f)}{3}} + \frac{(1 - r) \frac{b}{L}}{k_f + \frac{2}{3} \left(\frac{b}{L} \right) (k_s - k_f)} + \frac{\frac{\sqrt{3}}{2} - \frac{b}{L}}{k_f + \frac{4r}{3\sqrt{3}} \left(\frac{b}{L} \right) (k_s - k_f)} \right) \right) \quad (2.5)$$

where r is 0.09 and the ratio of the bump to half-length of the fiber, b/L, is given by:

$$\frac{b}{L} = \frac{-r + \sqrt{r^2 + 4(1 - \varepsilon) \frac{\sqrt{3}}{2} \left(\left(2 - r \left(1 + \frac{4}{\sqrt{3}} \right) \right) / 3 \right)}}{\frac{2}{3} \left(2 - r \left(1 + \frac{4}{\sqrt{3}} \right) \right)} \quad (2.6)$$

2.6. Interfacial Convective Heat Transfer Coefficient (ICHTC)

Due to the temperature difference between solid and fluid phases, heat transfer occurs in between phases. This heat transfer between two phases can be modeled by interfacial convective heat transfer coefficient. The determination of ICHTC can be done experimentally or numerically. Recent developments in computing technology make it possible to obtain the value of interfacial convective heat transfer coefficient accurately. The details of the technique to obtain interfacial convective heat transfer coefficient is explained in Chapter 5.

2.7. Tortuosity

Tortuosity is defined as the path length between two points that fluid particles travel divided to the length of straight line drawn between those two points. Due to the tortuous path of the porous medium, this ratio is always greater than 1. If one can measure the actual path travelled by fluid particle, usually by CFD method, then tortuosity can be obtained. Similarly, heat also cannot flow straight path. Instead, heat flow is distracted by solid structure and this effect is similarly called thermal tortuosity.

2.8. Thermal Dispersion

Dispersion occurs when convection exists due to the fluctuating motion of fluid. In other words, velocity or temperature fluctuations from the macroscopic point of view result in flow stream splitting and rejoining along the path of the flow, which distributes heat. Thermal dispersion depends on parameters such as Prandtl number, porosity, tortuosity (shape of the porous media) and thermal conductivities of fluid and solid phases. Due to anisotropic nature of many porous structures, dispersivity of heat through all principal axes is not same. Because of that, thermal dispersion is tensor quantity. However, literature survey shows that thermal dispersion in longitudinal direction is much higher compared to transverse direction. The relation of thermal dispersion will be explained in Chapter 5.

2.9. Boussinesq Approximation

Boussinesq approximation is a method, which is used in the field of buoyancy flow. Boussinesq approximation states that inertia is small and the gravity is strong which causes density difference between two points in fluid. If a buoyancy-driven, laminar boundary layer flow is assumed, which is incompressible, steady, 2D with constant thermo-physical properties and under gravity in $-x$ direction, the momentum equation in x direction can be written as:

$$u \frac{\partial u}{\partial x} + v \frac{\partial u}{\partial y} = -\frac{1}{\rho} \frac{dp_{\infty}}{dx} - g + \nu \frac{\partial^2 u}{\partial y^2} \quad (2.7)$$

where $\frac{dp_{\infty}}{dx}$ represents the pressure gradient outside of the boundary layer. The velocity in x -direction, u , is zero at the outside of boundary layer. Therefore, Eq. 2.7 can be written as:

$$\frac{dp_{\infty}}{dx} = -\rho_{\infty} g \quad (2.8)$$

If Eq. (2.8) is substituted into Eq. (2.7), Eq. (2.10) can be obtained:

$$u \frac{\partial u}{\partial x} + v \frac{\partial u}{\partial y} = -\frac{1}{\rho} (-\rho_{\infty} g) - g + \nu \frac{\partial^2 u}{\partial y^2} \quad (2.9)$$

$$u \frac{\partial u}{\partial x} + v \frac{\partial u}{\partial y} = \left(\frac{\rho_{\infty} - \rho}{\rho} \right) g + \nu \frac{\partial^2 u}{\partial y^2} \quad (2.10)$$

The first term on the right side of Eq. (2.10) is called as buoyancy force per unit mass. In natural or mixed convection flows, the density change is related to the temperature difference between points in the fluid. Therefore, buoyancy force may be related to volumetric thermal expansion coefficient, which shows the change of density with the change of temperature at constant pressure:

$$\beta = -\frac{1}{\rho} \left(\frac{\partial \rho}{\partial T} \right)_p \quad (2.11)$$

If we approximate Eq. (2.11) as follows:

$$\beta \approx -\frac{1}{\rho} \frac{\Delta \rho}{\Delta T} = \frac{1}{\rho} \frac{\rho_\infty - \rho}{T_\infty - T} \quad (2.12)$$

Then, Boussinesq approximation can be obtained:

$$(\rho_\infty - \rho) \approx \rho \beta (T_\infty - T) \quad (2.13)$$

2.10. Heat and Fluid Flow in Porous Media based on Volume Average Technique

As aforementioned in Chapter 1, two main approaches are employed for heat and fluid flow simulations in porous media. One of these approaches is known as Pore Scale Method (PSM) and the other one is Volume Averaged Method (VAM). These methods are explained in detail below.

2.10.1. Pore Scale Method

For PSM, the governing equations that should be considered to obtain velocity, pressure and temperature fields in each pore of the domain are the conservation of mass, momentum and energy equations. For a Newtonian fluid under incompressible flow condition and by considering constant thermo-physical properties, conservation of mass, momentum and energy for solid and fluid phases can be written, respectively, as below:

$$\nabla \cdot \vec{u} = 0 \quad (2.14)$$

$$\rho_f \left[\frac{\partial \vec{u}}{\partial t} + \vec{u} \cdot \nabla \vec{u} \right] = -\nabla p + \mu \nabla^2 \vec{u} + \vec{F} \quad (2.15)$$

$$(\rho C_p)_f \left[\frac{\partial T_f}{\partial t} + \vec{u} \cdot \nabla T_f \right] = k_f \nabla^2 T_f \quad (2.16)$$

$$(\rho C_p)_s \left[\frac{\partial T_s}{\partial t} \right] = k_s \nabla^2 T_s \quad (2.17)$$

2.10.2. Volume – Averaged Method

In VAM, the governing equations are integrated over a representative volume of porous media and volume-averaged governing equations (i.e. macroscopic governing equations) are obtained and through which discontinuity of phases is removed. Hence, the achieved governing equations can be solved for entire single-phase space. Due to integration, additional terms appear in governing equations that involves volume averaged transport parameters (i.e. macroscopic transport parameters).

Application of VAM should start with a selection of representative elementary volume (REV). A control volume within porous media should be taken which is larger than the microscopic characteristic length and smaller than the length of control volume as shown in Figure 2.1.

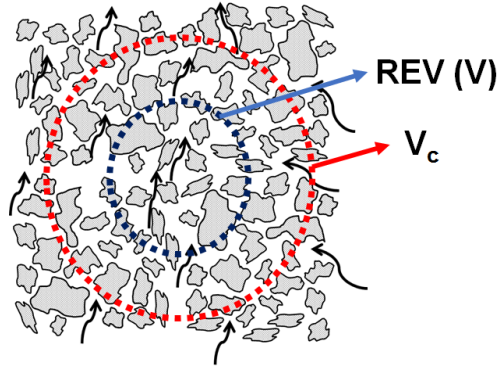


Figure 2.1. An appropriate selection of REV

Two types of volume averaging are reported in the literature. One of them is, considering porous media as continuous domain and obtaining volume-averaged value of any quantity such as ϕ :

$$\langle \phi \rangle = \frac{1}{V} \int_V \phi dV \quad (2.18)$$

The second type of volume averaging is known as intrinsic which can be used to obtain values for fluid and solid phases separately:

$$\langle \phi \rangle^f = \frac{1}{V_f} \int_{V_f} \phi dV \quad (2.19)$$

$$\langle \phi \rangle^s = \frac{1}{V_s} \int_{V_s} \phi dV \quad (2.20)$$

2.11. Derivation of General Form of Volume-Averaged Equations

General form of volume-averaged equations can be derived by taking volume integral of conservation of mass, momentum and energy equations. Before starting to derive the equations, the following relations used to derive the equations should be expressed:

$$\langle \phi_1 \phi_2 \rangle^f = \langle \phi_1 \rangle^f \langle \phi_2 \rangle^f + \langle \phi_1' \phi_2' \rangle^f \quad (2.21)$$

$$\langle \phi_1 \phi_2 \rangle = \frac{1}{\varepsilon} \langle \phi_1 \rangle \langle \phi_2 \rangle + \langle \phi_1' \phi_2' \rangle \quad (2.22)$$

$$\phi' = \phi - \langle \phi \rangle \quad (2.23)$$

$$\left\langle \frac{\partial \phi}{\partial t} \right\rangle = \frac{\partial \langle \phi \rangle}{\partial t} \quad (2.24)$$

where Eq. (2.21) is a relation for intrinsic average of multiplication and Eq. (2.22) is the relation for total volume averaged variables. Also, Eq. (2.23) and (2.24) show rules that are used in VAM. Prime superscript in Eq. (2.21) and (2.22) show the deviation of intrinsic volume-averaged value from pore-scale value, as given in Eq. (2.23). Furthermore, Slattery's Averaging Theorem (see Appendix for its derivation) is also needed for VAM equations derivations:

$$\langle \nabla \phi \rangle = \nabla \langle \phi \rangle + \frac{1}{V} \int_{A_{sf}} \phi dA \quad (2.25)$$

2.11.1. Volume – Averaged Conservation of Mass Equation

Pore scale conservation of mass equation is given in Eq. (2.14). By taking volume integral of Eq. (2.14) using Eq. (2.18):

$$\frac{1}{V} \int_V \nabla \cdot \vec{u} = \langle \nabla \cdot \vec{u} \rangle = 0 \quad (2.26)$$

and using Eq. (2.25), Eq. (2.26) can be expressed in a way:

$$\langle \nabla \cdot \vec{u} \rangle = \nabla \cdot \langle \vec{u} \rangle + \frac{1}{V} \int_{A_{sf}} \vec{u} dA \quad (2.27)$$

Hence, the integral of velocity on the fluid-solid interface is zero, due to no-slip condition, the second term of Eq. (2.27) drops. Therefore, volume-averaged conservation of mass equation can be expressed as:

$$\vec{\nabla} \cdot \langle \vec{u} \rangle = 0 \quad (2.28)$$

2.11.2. Volume – Averaged Conservation of Momentum Equation

To derive volume-averaged conservation of momentum equation, firstly, taking volume of integral of Eq. (2.15) should be done, which yields:

$$\rho_f \left\langle \frac{\partial \vec{u}}{\partial t} \right\rangle + \rho_f \left\langle \vec{u} \cdot \vec{\nabla} \vec{u} \right\rangle = -\langle \nabla p \rangle + \mu_f \left\langle \vec{\nabla}^2 \vec{u} \right\rangle \quad (2.29)$$

Using the rules given in Eqs. (2.21) – (2.24), Eq. (2.29) can be expressed as:

$$\begin{aligned} \rho_f \frac{\partial \langle \vec{u} \rangle}{\partial t} + \rho_f \left[\frac{1}{\varepsilon} \langle \vec{u} \rangle \cdot \langle \vec{\nabla} \vec{u} \rangle + \langle u_i \rangle \cdot \langle \vec{\nabla} u_i \rangle \right] &= -\vec{\nabla} \langle p \rangle - \frac{1}{V} \int_{A_{sf}} p dA \\ &+ \mu_f \left[\nabla^2 \langle \vec{u} \rangle + \frac{1}{V} \int_{A_{sf}} \vec{\nabla} \vec{u} dA + \vec{\nabla} \cdot \frac{1}{V} \int_{A_{sf}} \vec{u} dA \right] \end{aligned} \quad (2.30)$$

As the velocity is zero on the fluid-solid interface, the last term of Eq. (2.30) drops. Also, if pressure term is written as intrinsic value:

$$\rho_f \frac{\partial \langle \vec{u} \rangle}{\partial t} + \rho_f \left[\frac{1}{\varepsilon} \langle \vec{u} \rangle \cdot \langle \vec{\nabla} \vec{u} \rangle + \langle u' \rangle \cdot \langle \vec{\nabla} u' \rangle \right] = -\varepsilon \vec{\nabla} \langle p \rangle^f - \frac{1}{V} \int_{A_{sf}} p dA$$

$$+ \mu_f \left[\vec{\nabla}^2 \langle \vec{u} \rangle + \frac{1}{V} \int_{A_{sf}} \vec{\nabla} \vec{u} dA \right]$$
(2.31)

If we divide each term in Eq. (2.31) to porosity, Eq. (2.32) can be obtained:

$$\rho_f \frac{1}{\varepsilon} \frac{\partial \langle \vec{u} \rangle}{\partial t} + \rho_f \left[\frac{1}{\varepsilon^2} \langle \vec{u} \rangle \cdot \langle \vec{\nabla} \vec{u} \rangle + \frac{1}{\varepsilon} \langle u' \rangle \cdot \langle \nabla u' \rangle \right] = -\nabla \langle p \rangle^f + \mu_f \frac{1}{\varepsilon} \nabla^2 \langle \vec{u} \rangle - \frac{1}{\varepsilon} \frac{1}{V} \int_{A_{sf}} p dA$$

$$+ \frac{1}{V} \frac{1}{\varepsilon} \int_{A_{sf}} \nabla \vec{u} dA - \frac{1}{\varepsilon} \langle \vec{u}' \nabla \cdot \vec{u}' \rangle$$
(2.32)

Following the study of Vafai and Tien (1981), the last three terms of Eq. (2.32) can be rewritten as:

$$S = -\frac{\mu}{\rho K} \langle \vec{u} \rangle - \frac{C}{K^{1/2}} \left| \langle \vec{u} \rangle \right| \langle \vec{u} \rangle$$
(2.33)

Therefore, Eq. (2.33) turns into:

$$\rho \left(\frac{1}{\varepsilon} \frac{\partial \langle \vec{u} \rangle}{\partial t} + \frac{1}{\varepsilon^2} \langle \vec{u} \rangle \cdot \langle \vec{\nabla} \vec{u} \rangle \right) = -\vec{\nabla} \langle p \rangle + \frac{\mu}{\varepsilon} \vec{\nabla}^2 \langle \vec{u} \rangle$$

$$- \frac{\mu}{\rho K} \langle \vec{u} \rangle - \frac{C}{K^{1/2}} \left| \langle \vec{u} \rangle \right| \langle \vec{u} \rangle$$
(2.34)

2.11.3. Volume – Averaged Conservation of Energy Equation

By taking volume integral of Eq. (2.16) and (2.1

7), volume – averaged energy equation for fluid and solid phases can be obtained:

$$\rho_f C p_f \left(\left\langle \frac{\partial T}{\partial t} \right\rangle + \langle \vec{\nabla} \cdot \vec{u} T \rangle \right) = k_f \langle \vec{\nabla}^2 T \rangle$$
(2.35)

$$\rho_s C p_s \left\langle \frac{\partial T}{\partial t} \right\rangle = k_s \left\langle \bar{\nabla}^2 T \right\rangle \quad (2.36)$$

Using the rules given in Eq. (2.21) – (2.25), Eq. (2.35) and (2.36) can be written as follows:

$$\rho_f C p_f \left(\frac{\partial \langle T \rangle}{\partial t} + \bar{\nabla} \cdot \langle \vec{u} T \rangle + \frac{1}{V} \int_{A_{sf}} \vec{u} T dA \right) = k_f \bar{\nabla}^2 T + \bar{\nabla} \cdot \frac{1}{V} \int_{A_{sf}} k_f T dA + \frac{1}{V} \int_{A_{sf}} k_f \bar{\nabla} T dA \quad (2.37)$$

$$\rho_s C p_s \frac{\partial \langle T \rangle}{\partial t} = k_s \bar{\nabla}^2 T + \bar{\nabla} \cdot \frac{1}{V} \int_{A_{sf}} k_s T dA + \frac{1}{V} \int_{A_{sf}} k_s \bar{\nabla} T dA \quad (2.38)$$

The integration in the LHS of Eq. (2.37) vanishes because of the non-slip boundary condition at the solid-fluid interface. Since the temperature in both equations show the temperature of corresponding phases, the representation of intrinsic volume averaged might be better:

$$\begin{aligned} (\rho C p)_f \left(\frac{1}{\varepsilon} \frac{\partial \langle T \rangle^f}{\partial t} \langle \vec{u} \rangle \cdot \bar{\nabla} \langle T \rangle^f \right) &= \bar{\nabla} \cdot \left[k_f \varepsilon \bar{\nabla} \langle T \rangle^f + \frac{1}{V} \int_{A_{int}} k_f T^f dA - (\rho C p)_f \langle T' u' \rangle^f \right] \\ &\quad - \frac{1}{V} \int_{A_{int}} k_f \bar{\nabla} T^f \cdot \vec{n} dA \end{aligned} \quad (2.39)$$

$$\rho_s C p_{s,s} (1 - \varepsilon) \frac{\partial \langle T \rangle^s}{\partial t} = \bar{\nabla} \cdot \left[k_s (1 - \varepsilon) \bar{\nabla} \langle T \rangle^s - \frac{1}{V} \int_{A_{int}} k_s T^s dA \right] - \frac{1}{V} \int_{A_{int}} k_s \bar{\nabla} T^s \cdot \vec{n} dA \quad (2.40)$$

where, the second term on the right-hand side of Eq. (2.39) is thermal tortuosity, the third one is thermal dispersion and last one is interfacial convective heat transfer coefficient.

$$\rho_f c p_f \left(\varepsilon \frac{\partial \langle T \rangle^f}{\partial t} + \langle \vec{u} \rangle \cdot \bar{\nabla} \langle T \rangle^f \right) = k_{eff} \bar{\nabla}^2 \langle T \rangle^f + h_{int} A_{int} (\langle T \rangle^s - \langle T \rangle^f) \quad (2.41)$$

$$\rho_s c_{p_s} (1 - \varepsilon) \frac{\partial \langle T \rangle^s}{\partial t} = k_s (1 - \varepsilon) \bar{\nabla}^2 \langle T \rangle^s - h_{\text{int}} A_{\text{int}} (\langle T \rangle^s - \langle T \rangle^f) \quad (2.42)$$

Also, under thermal equilibrium, in other words, when $\langle T \rangle^s = \langle T \rangle^f$, Eq. (2.41) and (2.42) can be summed into one equation as:

$$\left(\varepsilon \rho_f c_{p_f} + (1 - \varepsilon) \rho_s c_{p_s} \right) \frac{\partial \langle T \rangle}{\partial t} + \frac{1}{\varepsilon} \langle \bar{u} \rangle \cdot \bar{\nabla} \langle T \rangle = k_{\text{eff}} \bar{\nabla}^2 \langle T \rangle \quad (2.43)$$

where k_{eff} in Eq. (2.43) is defined as:

$$k_{\text{eff}} = \varepsilon k_f + (1 - \varepsilon) k_s + k_{\text{dis}} + k_{\text{tor}} \quad (2.44)$$

where k_{dis} is thermal dispersion and k_{tor} is thermal tortuosity.

2.12. Determination of Volume-Averaged Transport Parameters

2.12.1. Thermal Dispersion

As aforementioned in section 2.8, thermal dispersion occurs in different directions in a porous medium due to the non-uniform velocity effects and temperature gradient. The value of the effective thermal conductivity depends on various parameters such as mass flow rate, porosity, shape of pores, and solid and fluid thermal properties. Since heat diffusion occurs in all directions, the effective thermal conductivity is a tensor whose diagonal terms represent longitudinal and transverse effective thermal conductivities of the porous continuum domain. Thermal dispersion can be modeled like gradient-type diffusion:

$$-\rho_f C_{p,f} \bar{\nabla} \cdot \langle T' \bar{u}' \rangle = k_{\text{dis}} \bar{\nabla}^2 \langle T \rangle \quad (2.45)$$

To obtain thermal dispersion in longitudinal direction, the following relation should be used:

$$k_{\text{dis},XX} = - \frac{1}{(\Delta T / L_{\text{ref},XX})} \frac{\rho_f C_{p,f}}{V} \int (T_f - \langle T_f \rangle) (u - \langle u_f \rangle) dV \quad (2.46)$$

Similarly, for transverse direction,

$$k_{dis,YY} = -\frac{1}{(\Delta T / L_{ref,YY})} \frac{\rho_f C_{pf}}{V} \int (T_f - \langle T_f \rangle) (u - \langle u_f \rangle) dV \quad (2.47)$$

As explained in section 2.6, in some situations, thermal equilibrium between solid and fluid phases can be no longer valid. Several problems that can be came across in the literature consist heat transfer from one phase to another. When the temperature at the bounding surface changes significantly with respect to time, and also when thermal conductivities of the solid and fluid phases differ from each other, the local rate of change of temperature for one phase differs significantly from that for the other phase. In those cases, two macroscopic equations for phases should be solved separately to obtain temperature distribution inside the porous medium. Therefore, ICHTC (h_{int}) should be calculated as below:

$$h_{int} = \frac{\frac{1}{V} \int k_f \vec{\nabla} T dA}{\langle T \rangle^s - \langle T \rangle^f} \quad (2.48)$$

2.13. Some Classical Theories for the Analysis of Heat and Fluid Flow in Porous Media

There are several fluid motion equations for studying of fluid flow in a porous medium. These classical theories are explained in this chapter. In the following subsections, these equations are discussed.

2.13.1. Darcy's Law

Henry Darcy's studies into hydrogeology stated that the volume averaged fluid velocity through a column of porous media is directly proportional to the pressure gradient established along the column and the permeability of the space and inversely proportional to the viscosity of the fluid. This equation for mixed convection can be written as:

$$\vec{u} = \frac{\overline{K}}{\mu} \vec{\nabla} p \quad (2.49)$$

2.13.2. Brinkman – Extended Darcy’s Law

Darcy’s Law fails when boundary effects are important. (i.e. internal flows) Therefore, additional terms for boundary conditions are needed to be included into fluid motion equation. Thus, a new variable depends on the fluid and structure of the porous medium, effective dynamic viscosity, should be introduced to the fluid motion equation.

$$\mu_{eff} \vec{\nabla} \vec{u} - \frac{\mu}{K} \vec{u} - \vec{\nabla} p = 0 \quad (2.50)$$

2.13.3. Forchheimer – Brinkman Extended Darcy’s Law

Darcy’s Law may not be appropriate when inertial forces are not negligible because Darcy’s Law is only function of pressure gradient and viscous effects. For high velocity fluid flow in the porous medium, the inertia effect should be included. Thus, a modification is needed to include inertial forces. Forchheimer – Brinkman Extended Darcy’s Law can be written as follows:

$$\mu_{eff} \nabla^2 \vec{u} - \frac{C}{\sqrt{K}} \rho_f \vec{u}^2 - \frac{\mu}{K} \vec{u} - \vec{\nabla} p = 0 \quad (2.51)$$

Eq. (2.34) is also known as Darcy-Brinkman-Forchheimer Law. If we start from Eq. (2.34), to obtain Darcy’s Law, the terms related to momentum change and viscous forces should be neglected as Darcy’s Law only interested in the pressure change along the column. Therefore, the following terms should be cancelled in Eq. (2.34) to obtain Darcy’s Law:

- $\frac{1}{\varepsilon} \frac{1}{\varepsilon^2} \left\langle \vec{u} \right\rangle \cdot \left\langle \nabla \vec{u} \right\rangle$: Change of volume-averaged momentum,
- $\frac{\mu}{\varepsilon} \nabla^2 \left\langle \vec{u} \right\rangle$: Effect of viscous stress,

- $\frac{\mu}{\rho K} \langle \vec{u} \rangle$: Effect of viscous forces,
- $\frac{C}{K^{1/2}} \left| \langle \vec{u} \rangle \right| \langle \vec{u} \rangle$: Effect of inertia forces

Brinkman- Extended Darcy's Law ignores the effect of inertia forces. Therefore, effect of inertia forces should be neglected from Eq. (2.34) to obtain Brinkman-Extended Darcy's Law.

CHAPTER 3

LITERATURE REVIEW

A recent literature review on porous media is given in this chapter. The review is divided into two parts as 2D periodic structure and modeling foam structures by X-Ray micro-tomography technique. Although there are many studies reported on the determination of the volume-averaged transport parameters for forced convection heat transfer, the studies reported on the determination of these transport parameters under mixed convection heat transfer are very limited. It should also be noted that, determination of ICHTC and thermal dispersion using micro-tomography technique both for forced and mixed convection heat transfer cases given in this review are very rare in open literature.

3.1. Literature Review on 2D Periodic Structure

The reported studies on the studied volume averaged transport parameters for 2D structure porous media is given in this section. The studies are divided into two subgroups for ICHTC and thermal dispersion. The governing parameters and the followed method in each study is reported.

3.1.1. Interfacial Convective Heat Transfer Coefficient

Convection in porous media by two-energy model to determine ICHTC is studied by Kuwahara et al. (2001). Figure 3.1 shows the staggered arrangement of the rods studied in their study. For the sake of computational resources, representative elementary volume is selected at the center of the computational domain as reported in Figure 3.1 by dashed lines. Re number is chosen between 0.01 and 1000 and porosity is taken between 0.36 and 0.96. Prandtl number is another governing parameter of their study and it varies between 0.01 and 100. A numerical analysis is employed and a correlation for ICHTC is given in their study. The correlation in their study can be seen in Eq. (3.1):

$$Nu = \left(1 + \frac{4(1-\varepsilon)}{\varepsilon}\right) + \frac{1}{2}(1-\varepsilon)^{1/2} Re_D^{0.6} Pr^{1/3} \quad (3.1)$$

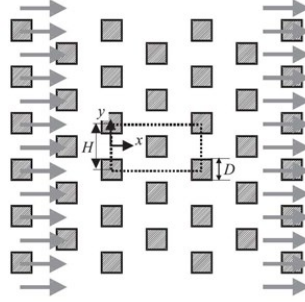


Figure 3.1. The considered domain in the study of Kuwahara et al. (2001)
(Source: Kuwahara et al., 2001)

Nakayama et al. (2002) studied anisotropy effect on the heat and fluid flow through an array of square rods in an infinite medium for different macroscopic flow angles and Reynolds numbers. The study of Nakayama et al. (2002) is very close to the study of Kuwahara et al. (2001) except the alignment of the rods. Nakayama et al. (2002) considered inline arrangement of rods in their study. The considered domain and the chosen REV are shown on Figure 3.2. Re number varied between 1 and 600 in their study and Pr number is taken as 1. Constant temperature different than the fluid temperature is given to the rods as boundary condition in order to simulate infinitely long domain. Furthermore, periodic boundary conditions were applied to the inlet and outlet sections of the domain. The anisotropy was created by changing the vertical distance between the rods. It was observed that the variation of the directional interfacial heat transfer coefficient with respect to the macroscopic flow angle is analogous to that of the directional permeability. The correlation for interfacial convective heat transfer coefficient was given as follows in their study:

$$Nu = \frac{1}{2}(c_{f_1} \cos^2 \alpha + c_{f_2} \sin^2 \alpha) + \frac{d_f^{0.3}}{2^{0.4}} Re_D^{0.6} Pr_f^{1/3} \quad (3.2)$$

When the studies of Kuwahara et al. (2001) and Nakayama (2002) compared, by changing rod arrangement from staggered to inline, Nu number decreases nearly 50% when $Re = 600$, $Pr = 1$ and porosity is 0.75.

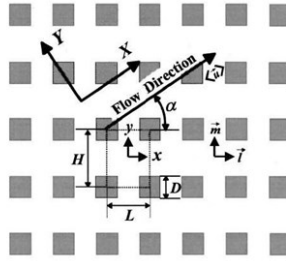


Figure 3.2. The considered domain in the study of Nakayama et al. (2002)
(Source: Nakayama et al., 2002)

Cross-flow heat transfer analysis over bank of rods for small Re numbers are studied by Gamrat et al. (2008). Aligned and staggered arrangements of rods as shown in Figure 3.3(a) are considered in their study. The boundary conditions were chosen as constant rod temperature and constant volumetric heat generation inside the rods. Their considered range for porosity was 0.44 – 0.98 and for Reynolds number was 0.05 – 40, for Pe number was 0.01 – 1000 and Prandtl number was 1 and 100. The effects of porosity, arrangement of the rods, Pr and Re numbers on the Nusselt number was examined. Linear temperature gradient was created in the flow direction for the cases with constant volumetric heat generation thermal boundary condition for solid phase. They proved that Nu number does not change with the change of thermal boundary condition when Re, Pr and porosity at the highest value considered in their study. They also concluded that Nu number was higher at staggered arrangement, especially at low porosity values. They reported correlations for Nu number for both inline and staggered arrangements in their study and these correlations are given in Eq. (3.3) and (3.4):

$$Nu = 3.02(1 - \varepsilon)^{0.278} \exp(2.54(1 - \varepsilon)) + ((1 - \varepsilon)0.44 + 0.092)Re_d^{0.5} Pr^{0.2} \quad (3.3)$$

$$Nu = 3.02(1 - \varepsilon)^{0.278} \exp(2.54(1 - \varepsilon)) + ((1 - \varepsilon)1.093 + 0.092)Re_d^{0.5} Pr^{0.2} \quad (3.4)$$

Compared their results with the results of Kuwahara et al. (2001) and Nakayama et al. (2002), as seen in Figure 3.3(b), Gamrat et al. (2008) over estimate the results under the same conditions as the comparison of their results given in Figure (3.3b). This difference may arise due to grid number difference between two studies.

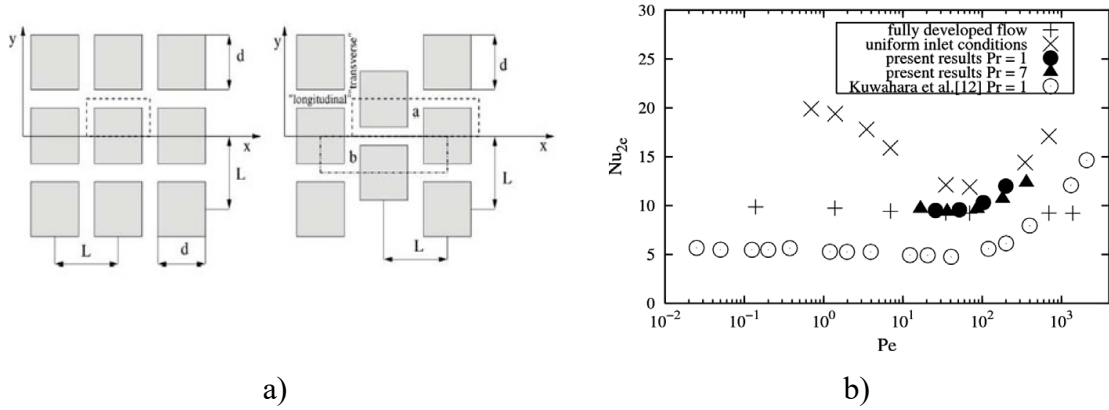


Figure 3.3. The study of Gamrat et al. (2008), a) the considered domain, b) the comparison of their results. (Source: Gamrat et al., 2008)

Yang et al. (2010) obtained ICHTC for spherical and ellipsoidal particles inside a structural packed bed numerically. The domain of their study is shown in Figure 3.4. Pr number is taken as 0.7 and Re number varies between 10 and 6000 in their study. They considered k- ϵ turbulence model. Walls of the channel are insulated and constant temperature was taken as boundary condition of the solid-phase. REV consists of 8 unit-cells was considered. The effects of packing form and particle shape are studied in detail and the flow and heat transfer performances in uniform and non-uniform packed beds are also compared with each other. They observed highest Nu number for spherical particles. A correlation is suggested for Nu number in their study. For instance, the correlation for face centered cubic spherical particles was given as:

$$Nu = 1.60 + 0.41Pr^{1/3} Re^{0.67} \left(\frac{d_p}{d_h} \epsilon \right)^{0.67} \quad (3.5)$$

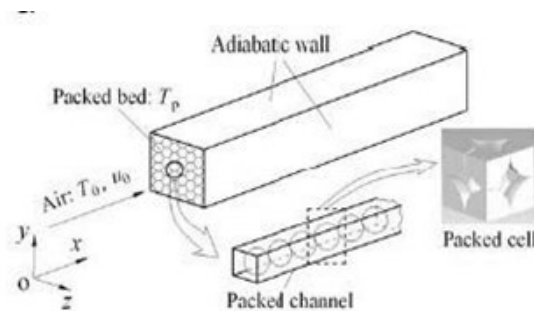


Figure 3.4. The considered domain in the study of Yang et al. (2010) (Source: Yang et al., 2010)

Pathak and Ghiaasiaan (2011) obtained interfacial convective heat transfer coefficient for a periodic porous media by considering laminar pulsating flow,

numerically. The parameters considered in their study were porosity, between 0.64 – 0.84, frequency, which varies between 0 and 100 Hz, and Re number between 70 and 980. They considered 8 - 12 unit cells in their domain to obtain periodic state solution due to pulsating flow as shown in Figure 3.5. One of the outcomes of their study was that the thermal dispersion is highly influenced by porosity. Also, they showed that Nu number increases by increase in frequency. Nearly 16% increase in Nu number can be observed by changing frequency from 20 Hz to 60 Hz.

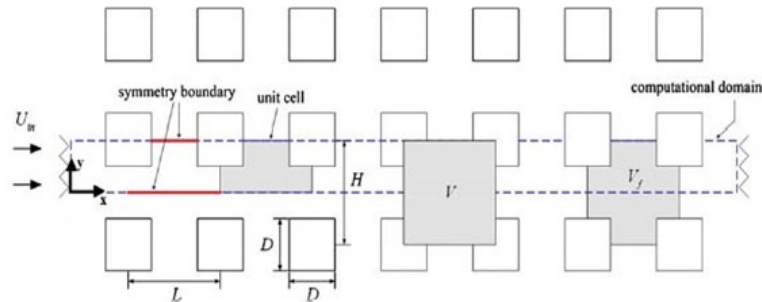


Figure 3.5. The considered domain in the study of Pathak and Ghiaasiaan (2011)
(Source: Pathak and Ghiaasiaan, 2011)

Teruel and Diaz (2013) considered laminar steady flow regime for a domain shown in Figure 3.6 and the range for their study was for Peclet numbers is 1– 103 and for porosity was between 0.55 and 0.95. Staggered alignment was studied by Teruel and Diaz (2013). They proved that selection of REV is very important. Their study shows that by selecting different REV, the obtained results may differ the results of Nu number nearly 100%. Moreover, they concluded that concept of logarithmic mean to carry out interfacial Nusselt number calculations was not an appropriate choice for a macroscopic study as volume-averaged quantities are not known in priori.

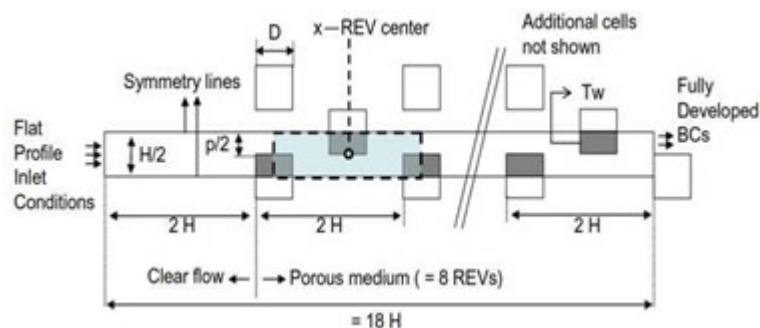


Figure 3.6. The considered domain in the study of Teruel and Diaz (2013)
(Source: Teruel and Diaz, 2013)

Ozgumus and Mobedi (2014) studied the effects of pore to throat size ratio ($H/(H-D_y)$ shown on Figure 3.7) on the interfacial heat transfer coefficient for a periodic porous media containing inline array of rectangular rods. The study was performed numerically. The considered domain is shown in Figure 3.7(a). Due to the periodicity, they considered a unit cell as it is shown in Figure 3.7(a). The study is performed for pore to throat size ratios between 1.63 and 7.46, porosities from 0.7 to 0.9 and Reynolds numbers between 1 and 100. They considered uniform temperature on solid walls. They concluded that, in addition to porosity and Reynolds number, the parameter of pore to throat size ratio plays a vital role on the heat transfer in porous media. They also reported in their study that the increase of pore to throat size ratio causes the mixing of the fluid in the voids between the particles and consequently the interfacial Nusselt number increases. As shown in Figure 3.7(b), results of Ozgumus and Mobedi (2014) shows a good agreement between the reported studies in the literature. The correlation given in their study can be seen at Eq. (3.6):

$$Nu = (a_0 \varepsilon + a_1) + (a_2 \varepsilon + a_3) Re^{0.6} Pr^{1/3} \quad (3.6)$$

The values of a in the equation 3.6 is given in the Table 2 of the study of Ozgumus and Mobedi (2014).

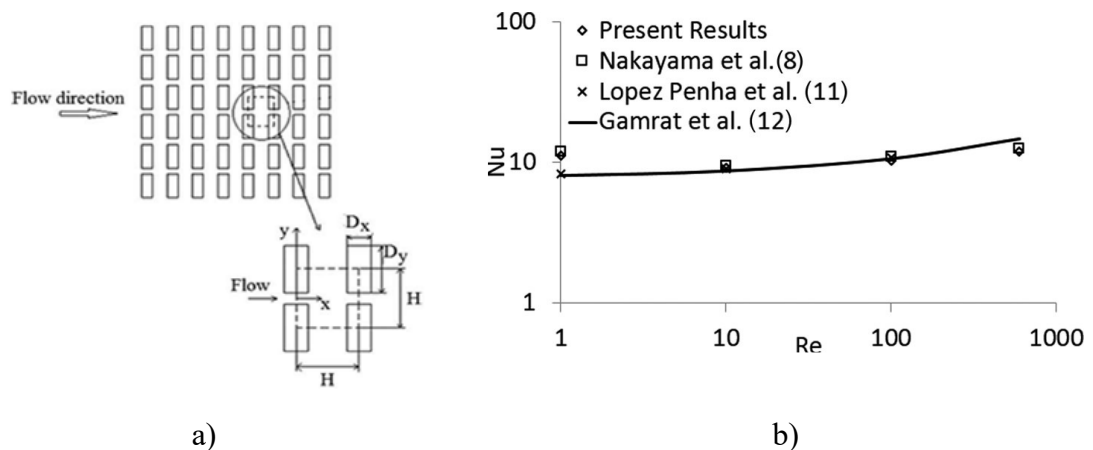


Figure 3.7. The study of Ozgumus and Mobedi (2015), a) the considered domain in the study, b) the comparison of their study with the reported studies (Source: Ozgumus and Mobedi, 2015)

Vu et al. (2014) studied forced convection of air through networks of square rods or cylinders embedded in microchannel as shown in Figure 3.8. Their considered representative elementary volume is shown in dashed lines on the Figure 3.8. They considered volumetric heating on the solid phase. They showed that the dynamically

developing length was found very short in comparison with the channel length due to the low Reynolds number flow. For this reason, a developed flow field may be predicted after one unit cell. They also concluded that Forchheimer and thermal dispersion effects are negligibly small when Reynolds number is very low.

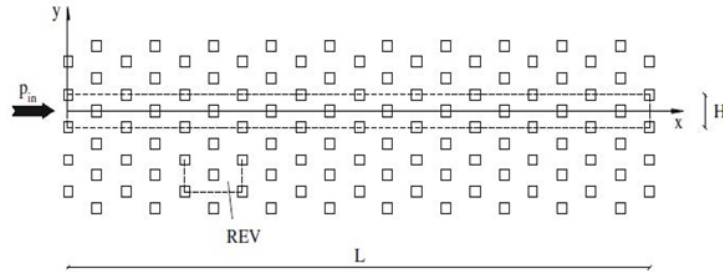


Figure 3.8. The considered domain in the study of Vu et al. (2014)
(Source: Vu et al., 2014)

3.1.2. Thermal Dispersion

Kuwahara et al. (1996) investigated transverse thermal dispersion (check the direction of volume-averaged temperature in Figure 3.9(a)) for 2D periodic porous structure numerically as shown in Figure 3.9. Square rods placed regularly and linear temperature gradient was imposed which is perpendicular to the flow direction. In their study, Re varies between 0.01 and 1000, porosity is between 0.1 and 0.9. Pr number is taken as 0.71. Thermal conductivity ratio is taken between 2 and 100. REV consists of one unit cell was taken and periodic boundary conditions were applied to create periodicity. Governing equations solved at pore level and volume averaging method employed. They proved that thermal dispersion influences temperature pattern highly, especially for the high Reynolds number flows. A correlation in terms of Re and porosity were reported. They observed a good agreement with experimental data for high Peclet numbers as seen in Figure 3.9(b). Their study may differ from experimental data at low Peclet numbers due to several numerical or digit errors. The correlation for determining transverse thermal dispersion can be seen in Eq. (3.7) and (3.8):

$$\frac{k_{dis,tr}}{k_f} = 0.022 \frac{Pe_D^{1.7}}{(1-\varepsilon)^{1/4}} \quad \text{when } Pe < 10 \quad (3.7)$$

$$\frac{k_{dis,tr}}{k_f} = 0.052(1-\varepsilon)^{1/2} Pe_D \text{ when } Pe > 10 \quad (3.8)$$

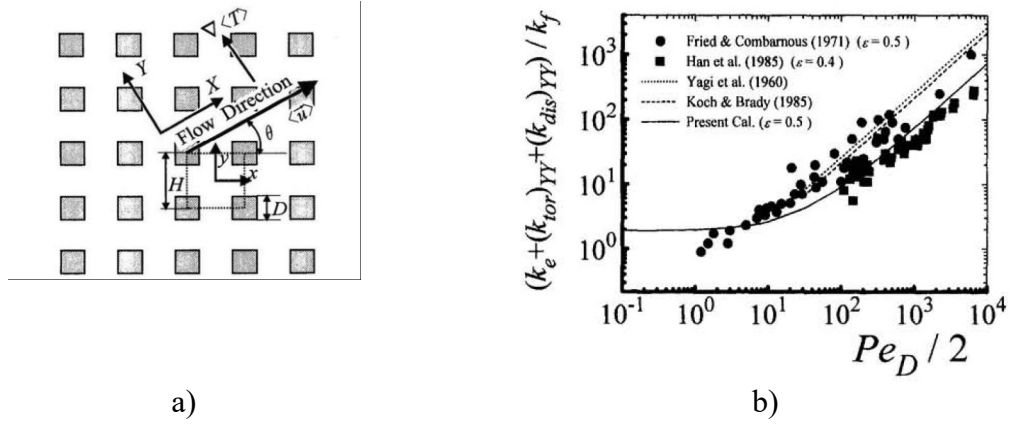


Figure 3.9. The study of Kuwahara et al. (1996), a) the considered domain, b) the comparison of their results with the reported studies. (Source: Kuwahara et al., 1996)

Kuwahara and Nakayama (1999) determined longitudinal thermal dispersion coefficients numerically by studying same periodic porous structure with Kuwahara et al. (1996). The considered domain is same with Nakayama et al. (2002), as well. Re number and other governing parameters were selected in the same range with Kuwahara et al (1996). The comparison of their study with the reported studies is given in Figure 3.10. As seen, the predicted apparent conductivities agree well with the experimental data. Moreover, compared to the study of Kuwahara et al. (1996), the present numerical study confirms that transverse thermal dispersion can be neglected compared to longitudinal dispersion, if Figure 3.9(b) and 3.10 compared. The correlations for obtaining longitudinal thermal dispersion, given in their study, can be seen in Eq. (3.9) and (3.10):

$$\frac{k_{dis,long}}{k_f} = 0.022 \frac{Pe_D^2}{(1-\varepsilon)^{1/4}} \text{ when } Pe < 10 \quad (3.9)$$

$$\frac{k_{dis,long}}{k_f} = 2.7 \frac{Pe_D}{\varepsilon^{1/2}} \text{ when } Pe > 10 \quad (3.10)$$

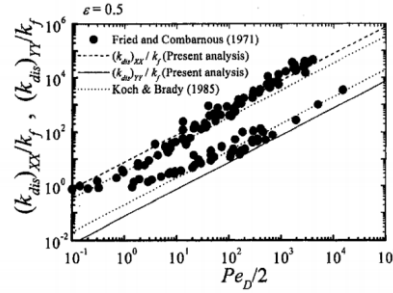


Figure 3.10. The comparison of Kuwahara and Nakayama (1999) with the literature (Source: Kuwahara and Nakayama, 1999)

Nakayama and Kuwahara (2005) developed algebraic porous model for thermal dispersion heat flux in porous media. Pore scale and volume-averaged governing equations considered and dispersion heat flux was expressed as transport equation. Their algebraic model was consistent with the gradient-type diffusion hypothesis of Kuwahara and Nakayama (1999) and the results agree very well with the gradient type model, as shown in Figure 3.11. The correlation to determine algebraic type thermal dispersion was given as in Eq. (3.11) in their study:

$$\frac{k_{dis, long}}{k_f} = \frac{4.5 \left(\frac{\varepsilon}{150(1-\varepsilon)^{1/2}} \right) Pe_d^2}{Pr + \left(\frac{1.75}{150(1-\varepsilon)} \right) Pe_d} \quad (3.11)$$

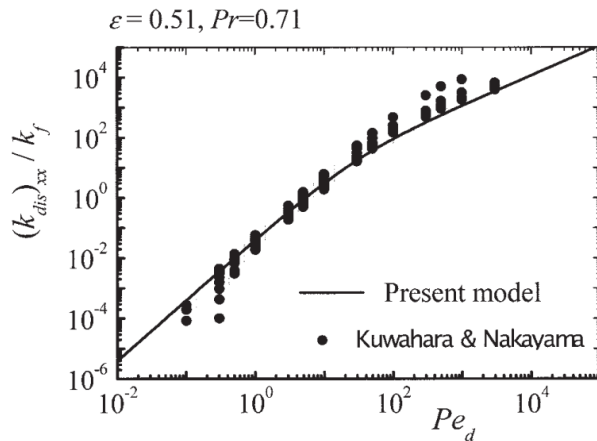


Figure 3.11. The comparison of the study of Nakayama and Kuwahara (2005) with the study of Kuwahara and Nakayama (1999) (Source: Nakayama and Kuwahara, 2005)

Analysis of hydrodynamic and thermal dispersion in porous media by means of a local approach is conducted by Saada et al. (2006) as shown in Figure 3.12. A pore scale analysis was implemented in this numerical study to investigate the behavior of microscopic inertia and thermal dispersion in a porous medium with a periodic structure. Re number was taken till 150 in their study, while Pe varies between 1 and 103, porosity was between 0.1 and 0.9 and thermal conductivity ratio of solid and fluid phases was between 0.1 and 103. The flow field at a pore scale was computed using the continuity and Navier–Stokes equations. The macroscopic characteristics of the flow field were obtained by an averaging technique of local velocities in conjunction with the Darcy – Forchheimer model. They considered different Peclet and solid – fluid thermal conductivity values in their study. They computed transverse and longitudinal dispersion conductivities for various porosities, Re, Pe numbers and solid-to-fluid conductivity ratio values. Longitudinal thermal dispersion is observed higher for inline arrangement while transverse thermal dispersion is higher for staggered arrangement under same conditions and in the range considered in their study.

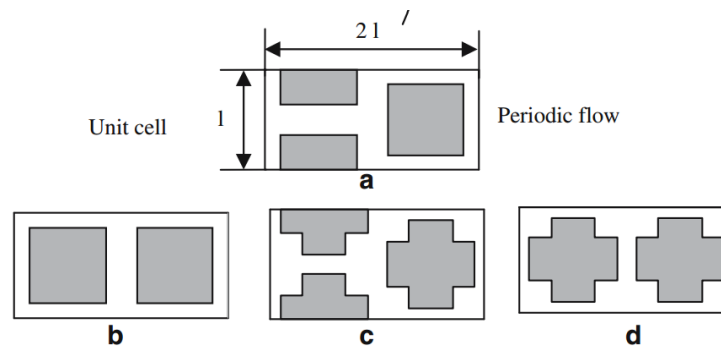


Figure 3.12. The considered domains in the study of Saada et al. (2006)
(Source: Saada et al., 2006)

Pedras and de Lamos (2008) considered an infinite periodic array of elliptic rods in a numerical study as given in Figure 3.13. Two different thermal conductivity ratios between the solid and fluid phases were used for analyzing their effect on the thermal dispersion tensor, following a systematic analysis of several porous media modeled by different unit-cell geometry. Turbulence was assumed to exist within the fluid phase and a low Reynolds $k - \varepsilon$ closure was used to model it. They concluded that the type of boundary condition does not change the longitudinal thermal dispersion value significantly and only a slight effect on transverse thermal dispersion. Longitudinal dispersion was found to be less sensitive to the variations of porosity, conductivity ratio and porous structure. However, the results of their correlation for longitudinal thermal

dispersion disagrees with the results of Nakayama and Kuwahara (1999). Correlations for longitudinal and transverse thermal dispersion were given as:

$$\frac{k_{dis, long}}{k_f} = 3.52 \times 10^{-2} Pe_H^{1.65} \quad (3.12)$$

$$\frac{k_{dis, tr}}{k_f} = 1.55 \times 10^{-4} Pe_H^{0.94} \quad (3.13)$$

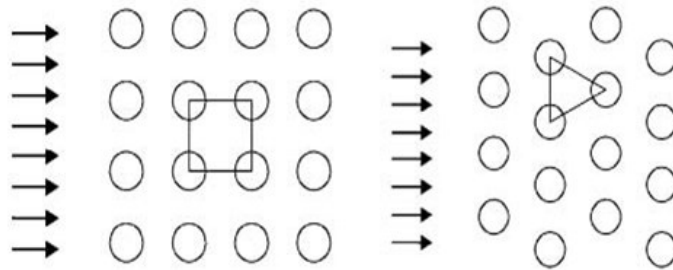


Figure 3.13. The considered domain in the study of Pedras and de Lamos (2008)
(Source: Pedras and de Lamos, 2008)

An analytical study on the determination of thermal dispersion in parallel plates was studied by Xu et al. (2010) as in Figure 3.14. Three different cases were considered in their study. Firstly, a transient heat transfer analysis due to an arbitrary initial temperature distribution within the fluid was done. Then, a steady heat transfer with constant heat flux on all plate surfaces was completed. Following that, a steady heat transfer with constant wall temperatures was considered. Velocity non-uniformity and temperature non-uniformity were studied. They concluded that the thermal dispersion in parallel plate arrays is caused by the non-uniformity of heat flux distribution at the pore level. Molecular diffusion and hydraulic dispersion is found as a function of pore morphology, porosity and the underlying fluid flow. They also concluded that a value of thermal dispersion obtained under one thermal boundary condition might differ significantly when thermal boundary condition is changed. Therefore, the value of thermal dispersion obtained considering different boundary condition should be used carefully.

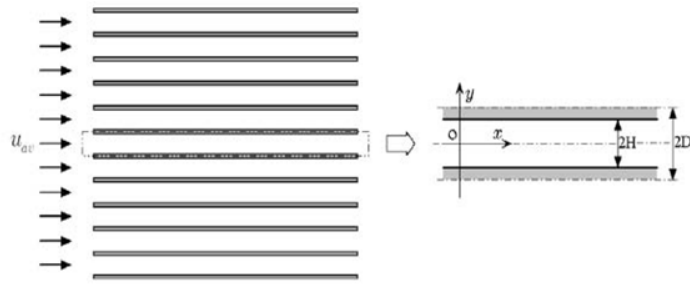


Figure 3.14. The considered domain in the study of Xu et al. (2010)
(Source: Xu et al., 2010)

Alshare et al. (2010) studied thermal dispersion in isotropic and anisotropic porous media using unit cell scale. They considered both steady and unsteady solution in their study. They considered periodic array of rectangular rod, as shown in Figure 3.15. They applied constant heat flux to fluid-solid interface. They carried out their research for $1 < \text{Re} < 1000$. It is concluded that thermal dispersion depends on rod arrangement more than shape of the particles. Moreover, they showed that their results of longitudinal thermal dispersion have an acceptable good agreement with Saada et al. (2006), as reported in Figure 3.15(b).

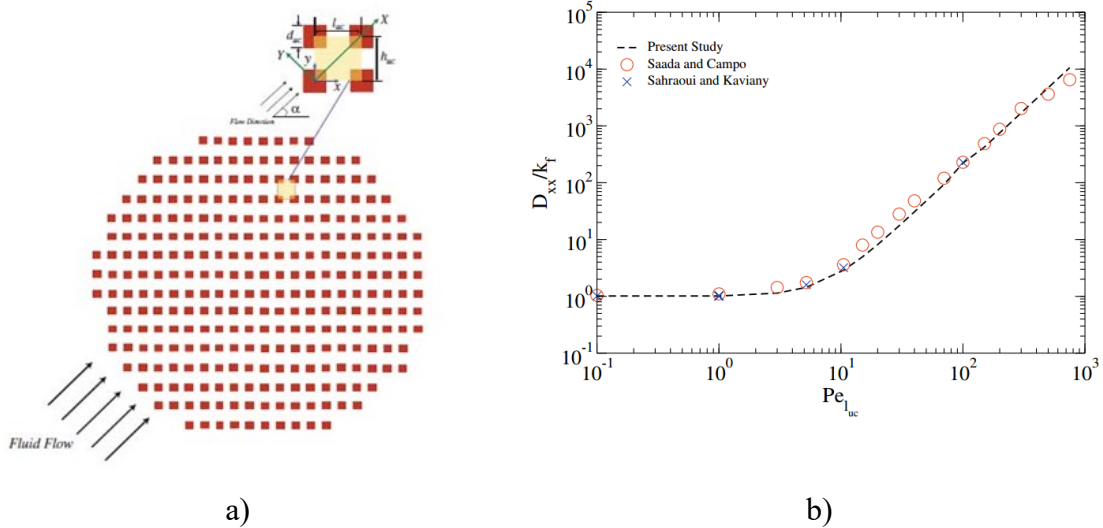


Figure 3.15. The study of Alshare et al. (2010), a) the considered domain, b) the comparison of their study. (Source: Alshare et al., 2010)

Another study on the thermal dispersion was made by Yang and Nakayama (2010) for a geometry given in Figure 3.16. Using thermal non-equilibrium method,

they derived an expression for longitudinal and transverse thermal dispersion, respectively, as:

$$\frac{k_{dis, long}}{k_f} = 0.15 \frac{Pe_D^2}{2.0 + 1.1Pe_D^{0.6} / Pr^{0.27}} \quad (3.14)$$

$$\frac{k_{dis, long}}{k_f} = 0.0075 \frac{Pe_D^2}{2.0 + 1.1Pe_D^{0.6} / Pr^{0.27}} \quad (3.15)$$

They observed a connection between interfacial heat transfer coefficient and thermal dispersion in a way that interfacial heat transfer at the local non-thermal equilibrium influences the macroscopic temperature and this causes an effect on thermal dispersion, as well.

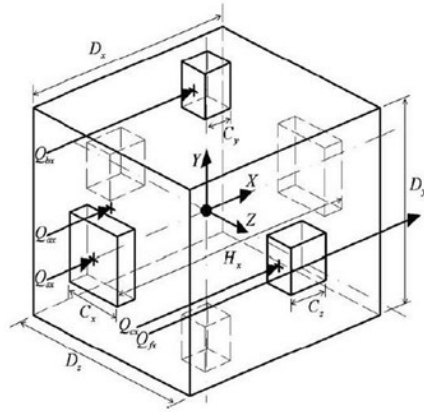


Figure 3.16. The solution domain in the study of Yang and Nakayama (2010)
(Source: Yang and Nakayama, 2010)

Pathak and Ghiaasiaan (2011), like their interfacial convective heat transfer coefficient study given in Figure 3.5, also studied thermal dispersion numerically for a laminar pulsating flow. Same range with their interfacial convective heat transfer coefficient for porosity, frequency and Re considered. Similar to Yang and Nakayama (2010), they also showed that the connection between interfacial convective heat transfer coefficient and thermal dispersion term. Moreover, in addition to the study of Yang and Nakayama (2010), they reported that the porosity is also effective on thermal dispersion. Empirical correlation was given for the longitudinal thermal dispersion term in their study as follows:

$$\frac{k_{dis, long}}{k_f} = (A \ln(\text{Re}_L) - 37.7) \frac{(1 - 0.0000000 W_L^2 - 0.00008 W_L)}{(1.2558 + 0.0004 \text{Re}_L)^{((\varepsilon - 0.64)0.11)}} \quad (3.16)$$

$$W_L < 2700: A = 10.35$$

$$W_L > 2700: A = 10.8$$

Estimation of the thermal dispersion in a porous medium of complex structures using a lattice Boltzmann method was studied by Jeong et al. (2011) for the domain shown in Figure 3.17. Lattice Boltzmann Method (LBM) is known as CFD method in which Boltzmann Equation, which describes the statistical behavior of a thermodynamic system under non-equilibrium, is solved instead of Navier-Stokes Equations. In addition to obtaining transport parameters for 2D and 3D domains, to obtain the flow fluid in the narrow pores effectively, LBM is chosen in their study. They considered two-dimensional arrays of uniformly distributed circular and square cylinders, and uniformly distributed spherical and cubical inclusions. They solved for fluid flow and heat transfer for various Prandtl and Reynolds number combinations. Re number varies between 0.1 and 100, Pr number is between 0.1 and 20 and porosity is between 0.44 and 0.85. They showed that for both 2D and 3D cases, the dispersivity is found to increase with the Peclet number raised and the in-line arrangement yields higher dispersivity than the staggered arrangement, however, the dispersivity is independent of the inclusion shape except for the 3D staggered cases. They also obtained new correlations for dispersivity for 2D and 3D cases. For instance, for inline arrangement, a correlation in terms of Peclet number, porosity, and the fluid–solid diffusivity ratio can be given as:

$$\frac{k_{dis, long}}{k_f} = \exp(-C_2) Pe_L^{1.75} \quad (3.17)$$

where C_2 is :

$$C_2 = \exp(a_2) (k_s / k_f)^{a_1}$$

$$a_1 = -0.1554 + 0.1595\varepsilon$$

$$a_2 = 1.783 - 1.775\varepsilon + 1.716\varepsilon^2$$

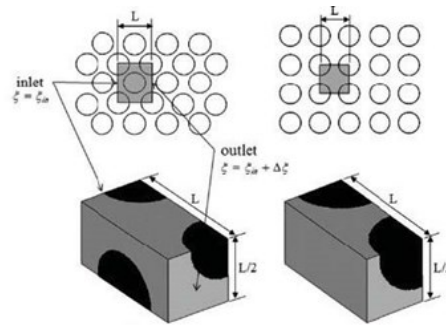


Figure 3.17. The considered solution in the study of Jeong et al. (2011)
(Source: Jeong et al., 2011)

Ozgumus and Mobedi (2016) studied the effect of pore to throat size ratio on thermal dispersion by considering the same domain of Ozgumus and Mobedi (2015). The considered domain in their study was given in Figure 3.7. They found that there is a threshold value of pore to throat size ratio for maximum longitudinal thermal dispersion coefficient while the transverse thermal dispersion increases with the increasing of values of pore to throat size ratio.

3.2. Literature Review on Foam Structures

Modeling foam structures using x-ray micro-tomography is one of the recent methods to study volume-averaged transport parameters. It is a popular method around the researchers/engineers as it allows modeling the foam structure as its geometrical details without making any assumptions. All of the reported studies are on forced convection cases, where no reported studies are found for mixed convection in the open literature.

3.2.1. Permeability and Inertia Coefficient

One of reported studies on determining permeability and inertia coefficient of metal foams using micro-tomography technique was done by Petrasch et al. (2008). The considered structure in their study is shown in Figure 3.18. They studied on determination of permeability and inertia coefficient of reticulate porous ceramics by using micro-tomography technique. The pore scale Re number was changed from 2 and 200 in their study. The porosity of their structure is 0.85. As a leading study, Petrasch et al. (2008) showed that micro-tomography method could be applicable to any material that can be resolved through micro-tomography device (i.e. x-ray opaque). Their study

showed that, instead of obtaining macroscopic transport parameters by considering expensive experimental setups, those parameters could be obtained within the limits of the numerical truncation error and the accuracy of geometrical representation.

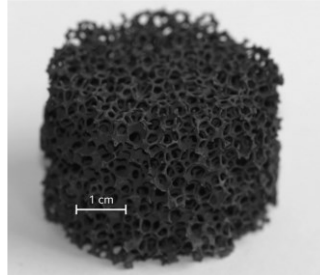


Figure 3.18. The foam structure in the study of Petrasch et al. (2008)
(Source: Petrasch et al., 2008)

Magnico (2009) analyzed determination of permeability tensor by CFD from creeping flow to inertial flow regime for isotropic and anisotropic metallic foams. They considered nickel-chrome foams with pore density of 17 – 23 PPI, with porosity of 0.873. Re number in the study of Magnico (2009) was changed between 0.001 and 40. The cut of the structure in the study of Magnico (2009) is shown in Figure 3.19. It was concluded that Darcy–Forchheimer law is valid for $Re > 1$ and similar with the permeability, the inertial coefficient might be an asymmetric tensor quantity. Magnico (2009) might be the first researcher in the open literature to report this behavior.

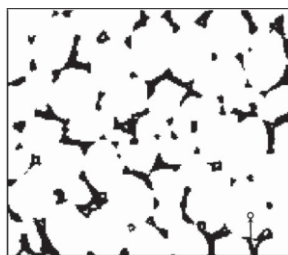


Figure 3.19. 2D cut of the foam structure in the study of Magnico (2009)
(Source: Magnico, 2009)

Akolkar and Petrasch (2012) studied two kinds of porous media that are reticulated porous ceramic foam and packed bed of CaCO_3 particles by pore scale analysis. The solution domain of their study is given in Figure 3.20. They considered Re number between 0.1 and 200. Porosity in their study changed between 0.727 and 0.913 for reticulated porous ceramic foam while for CaCO_3 particles, it changed between 0.329 and 0.824. The permeability and the Forchheimer coefficients were determined

and different prediction models, such as Ergun equation and Ward correlation, for predicting of permeability are compared. They found that the Forchheimer coefficient obtained by Ergun equation differ 13% from their results while Ward correlation fails to predict their result with adequate accuracy.

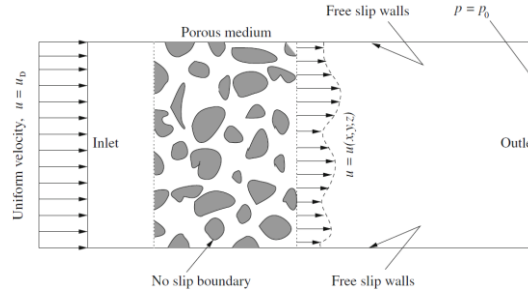


Figure 3.20. The considered domain in the study of Akolkar and Petrasch (2012)
(Source: Akolkar and Petrasch, 2012)

Micro-tomography based CFD simulation of flow and heat transfer for three different open-cell aluminum foams (10 and 30 PPI) were studied by Ranut et al. (2014). From CFD simulations, hydraulic permeability and effective stagnant thermal conductivity were calculated. Porosity varies between 0.929 and 0.944 in their study. They have concluded that flow and thermal simulations have an isotropic behavior for 30 PPI foam. On the contrary, a directional dependence in the computed flow permeability and effective thermal conductivity has been evinced for the 20 and 10 PPI foams. This effect should be investigated in detail as it might be a new phenomenon or just due to image-processing errors. Moreover, they also observed same effect with Magnico (2009) for inertia coefficient. The considered geometries in the study of Ranut et al. (2014) are given in Figure 3.21.

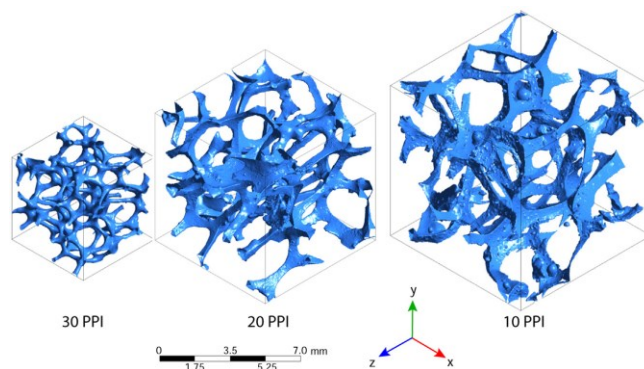


Figure 3.21. The considered geometries in the study of Ranut et al. (2014)
(Source: Ranut et al., 2014)

CFD characterization of flow regimes inside the open cell aluminum foams as shown in Figure 3.22 was done by Della Torre et al. (2014). The transition of flow from the laminar to the turbulent regime in idealized foam by means of unsteady numerical simulations were studied. They used 40 PPI aluminum metal foam and modified pore density into 10, 20 and 80 PPI from the original 40 PPI sample by using dilation of the geometry. The porosity changed between 0.897 and 0.956 in their study. They also modeled foam structure by considering ideal foam theory and obtained a good agreement between both micro-tomography and ideal foam method. They observed the connection between porosity and permeability can be assumed exponential.

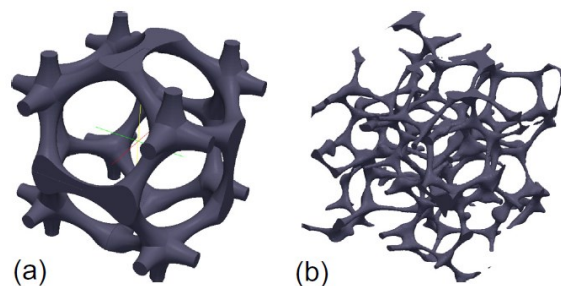


Figure 3.22. The considered samples in the study of Della Torre et al. (2014); a) ideal foam model, b) real foam structure (Source: Della Torre et al., 2014)

Micro-tomography based numerical simulation of fluid flow in open cell metal foams was done by Zafari et al. (2015). The porosity varied between 0.85 and 0.90 in their study. A typical geometry considered by Zafari et al. (2015) is given in Figure 3.23. They observed lower pressure drop due to lower resistance by increasing the porosity.

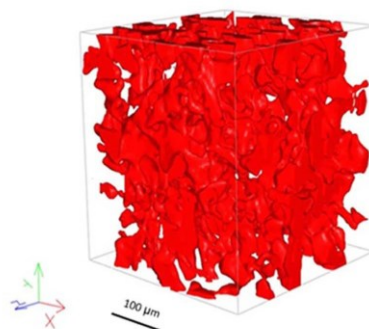


Figure 3.23. The considered sample in the study of Zafari et al. (2015) (Source: Zafari et al., 2015)

Pressure drop and heat transfer through metal foams were numerically investigated by Diani et al. (2015). Copper foams with 5, 10, 20 and 40 PPI, given in Figure 3.24, were considered in their study. The porosity in their study changes between 0.935 and 0.936. They showed a good agreement with the micro-tomography methodology and experimental and theoretical results. They compared their study with the experimental results of Mancin et al. (2013) and their results predict pressure gradient around 4% absolute deviation with the results of Mancin et al. (2013).

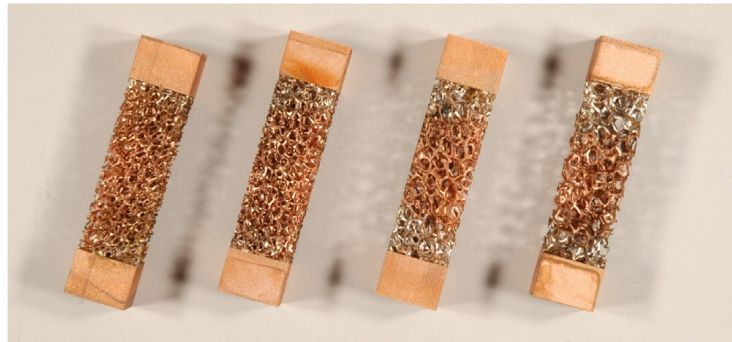


Figure 3.24. The considered samples in the study of Diani et al. (2015)
(Source: Diani et al., 2015)

The effects of strut shape of open-cell metal foams on interfacial convection heat transfer and pressure drop were studied by Ambrosio et al. (2016). Their model is given in Figure 3.25. Three aluminum metal foam samples with porosities of 0.88, 0.94 and 0.97 were considered in their study. They also generated ideal foam structure of the metal foams they considered in their study. They concluded that Nusselt number might be predicted accurately by using ideal foam theories when the strut shape of metal foams can be extracted. They concluded that the convex strut shape maximizes the convection heat transfer and minimizes the pressure drops, for any porosity and velocity considered in their study.

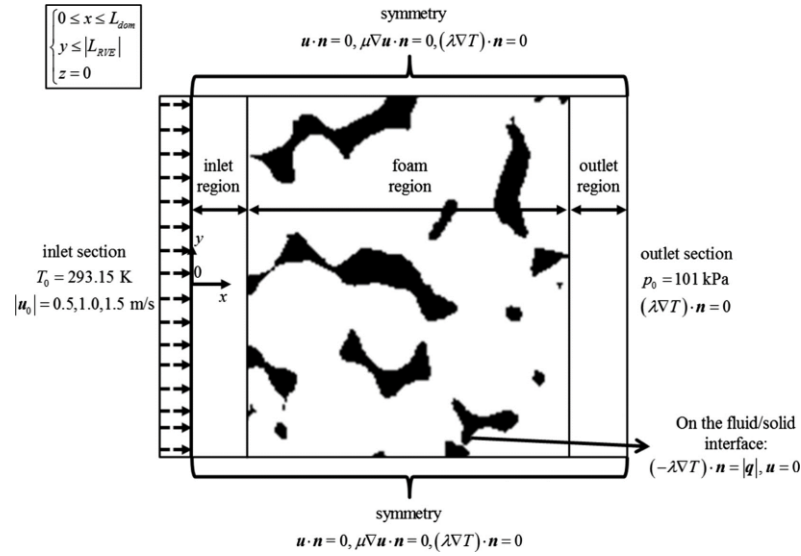


Figure 3.25. The considered samples in the study of Ambrosio et al. (2016)
(Source: Ambrosio et al., 2016)

3.2.2. Interfacial Convective Heat Transfer Coefficient

Determination of the interfacial convective heat transfer coefficient for real foam structures are a challenging task as modeling the foam structure in computer environment can be very cumbersome. Recent developments in micro-tomography technique allow researchers to extract the real structure of the domain by taking slice images and rendering the foam structure by using image-processing software. The reported studies on the determination of interfacial convective heat transfer coefficient by micro-tomography technique are still very limited due to the fact that the need on high computing sources. For instance, Vijay et al. (2015) obtained porosity, pore diameter, strut diameter and specific surface area by considering micro-tomography method and evaluated ICHTC using homogenization method and they supposed correlation by the correlation of Zukauskas (1987) taking as base model and they reported their correlation as:

$$\frac{h_v d_c}{a_s k_f} = C_t \text{Re}^{0.5} \text{Pr}_{f_e}^{0.37} \quad (3.18)$$

where C_t is a constant and it changes with PPI (and porosity, consequently).

In addition to their permeability and inertia coefficient study, Zafari (2015) also studied on heat flow and reported interfacial convective heat transfer coefficient by employing micro-tomography technique. Their considered domain was given in Figure 3.23. They considered local non-equilibrium thermal condition between solid and fluid

in their simulations. They showed that by changing the solid material from aluminum to copper, a significant increase in the effective stagnant thermal conductivity takes place, however they did not report exact increase in their study. They reported a correlation for obtaining interfacial convective heat transfer coefficient:

$$Nu_K = 0.0016 + 0.16\varepsilon^{-3} Re_K^{0.28} \quad (3.19)$$

where Re and Nu numbers are evaluated based on permeability and porosity. This correlation was obtained numerically.

Calmidi and Mahajan (2000) analyzed heat transfer in metal foams both numerically and experimentally. They considered different pore density and porosities in aluminum metal foams. They showed that for foam-air combinations, the transport enhancing effect of thermal dispersion is extremely low due to the relatively high conductivity of the solid matrix. However, for foam-water combinations, their results indicate that thermal dispersion can be very high and accounts for bulk of the transport. They reported a correlation for interfacial convective heat transfer coefficient as:

$$Nu_v = 8.72(1 - \varepsilon)^{1/4} \left(\frac{1 - e^{-(1-\varepsilon)/0.04}}{\varepsilon} \right)^{1/2} \left(\frac{\langle u \rangle d_m}{\nu} \right)^{1/2} Pr^{0.37} \quad (3.20)$$

3.2.3. Thermal Dispersion

Reported studies on the determination of thermal dispersion of foam structures are also very limited. Moreover, determination of thermal dispersion by using microtomography technique is not reported in the open literature. Zhang et al. (2015) analyzed thermal dispersion considering VAM analytically and numerically and reported a correlation for thermal dispersion for metal foams. Their model is shown in Figure 3.26. They obtained volume- averaged governing equations for convection in nanofluid-saturated metal foams. They analyzed nanofluid in their study and considered Buongiorno model to analyze nanofluid effects. They obtained relations for both longitudinal and transverse thermal dispersion. This study is the only reported study on longitudinal thermal dispersion. They reported the following correlations for both longitudinal and transverse thermal dispersion:

$$\frac{\varepsilon k_{dis_{yy}}}{k_f} = \frac{3}{8} \frac{\left(\frac{\rho c \langle u \rangle d_m}{k_f} \right) \text{Pr}^{0.13}}{8.72(1-\varepsilon)^{1/4} \left(\frac{1 - e^{-(1-\varepsilon)/0.04}}{\varepsilon} \right)^{1/2}} \quad (3.21)$$

$$\frac{\varepsilon k_{dis_{xx}}}{k_f} = \frac{3}{15^2 * 8} \frac{\left(\frac{\rho c \langle u \rangle d_m}{k_f} \right) \text{Pr}^{0.13}}{8.72(1-\varepsilon)^{1/4} \left(\frac{1 - e^{-(1-\varepsilon)/0.04}}{\varepsilon} \right)^{1/2}} \quad (3.22)$$

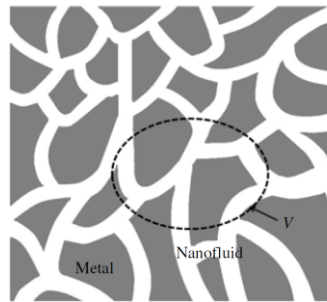


Figure 3.26. Considered model in the study of Zhang et al. (2015)
(Source: Zhang et al., 2015)

Calmidi and Mahajan (2000) also studied transverse thermal dispersion experimentally, their setup was given in Figure 3.27. Similar to their study reported under section 3.2.2, they obtained transverse thermal dispersion values for the same studied aluminum alloy foams. They obtained a correlation for transverse thermal dispersion as:

$$\frac{k_{disp}}{k_f} = 0.06(\text{Re}_K \text{Pr}_e) \frac{u}{u_o} \quad (3.23)$$

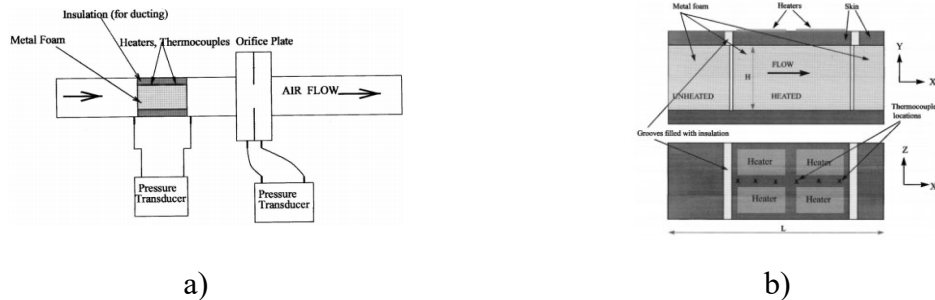
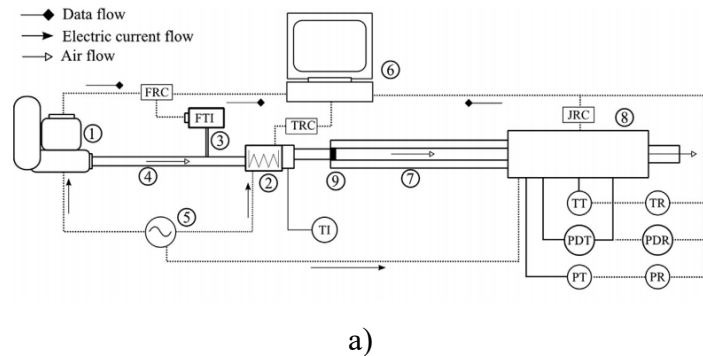


Figure 3.27. Considered experimental setup in the study of Calmidi and Mahajan (2000), (Source: Calmidi and Mahajan, 2000)

In addition to their ICHTC study, Vijay et al. (2015) also studied transverse thermal dispersion experimentally. Similarly, they considered alumina foam structures with porosity between 0.80 and 0.87. They considered thermal non-equilibrium model in their study. Their experimental setup is given in Figure 3.28. They compared their results with the reported theoretical studies and they reported good agreement with the reported studies.



a)
Figure 3.28. Considered experimental setup in the study of Vijay et al. (2015)
(Source: Vijay et al., 2015)

This literature survey shows that, on metal foams, permeability and inertia coefficients differ significantly between studied foam structures. In order to make sure the results are correct, several checks, which will be shown in the following chapters, should be done. Moreover, micro-tomography technique can be a good method to obtain volume averaged transport parameters such as interfacial convective heat transfer coefficient, longitudinal and transverse thermal dispersion values more accurately.

CHAPTER 4

STUDIED POROUS MEDIA

Since a porous geometry can be very complicated, some simplifications are considered in literature. Modeling foam as 2D rods is one of these approaches. In this chapter, a similar simplification is done and a 2D periodic structure is studied. Additionally, recent developments in computing technologies allow researchers to model real 3D foam structures in computer environment and perform 3D flow simulations. The studied ceramic and metal foams are also described in this chapter and related geometrical parameters are presented.

4.1. Studied Porous Media

The considered domain for 2D periodic structure studies is a square rod, while the considered domain of 3D studies are aluminum and ceramic foams. These structures are explained below.

4.1.1. 2D Periodic Structure

The schematic view of the geometry is shown in Figure 4.1. The studied domain consists of infinite square blocks in horizontal direction while number of rods in vertical direction is only 10. The axial length of rods in z-direction is assumed to be large and therefore, two-dimensional flow assumption can be employed. A representative elementary volume (REV) bounded by dash line is shown in Figure 4.1, can be studied to obtain results for entire domain. The radiation heat transfer and viscous dissipation are neglected and gravity acts in $-y$ direction. To prevent computational difficulties at the outlet boundary of the porous media (due to possible reverse flows), an extension region is considered on the top of blocks. The ratio between L and H (i.e. L/H as shown in Figure 5.1) is 19. The local and average interfacial heat transfer coefficient between the solid rods and the surrounding fluid is obtained for five porosity values (0.51, 0.64, 0.75, 0.84 and 0.96) and for Ri number in the range of from 0.01 to 10 and Re number

in the range of from 100 to 500. The study is performed for air with Prandtl number of 0.71.

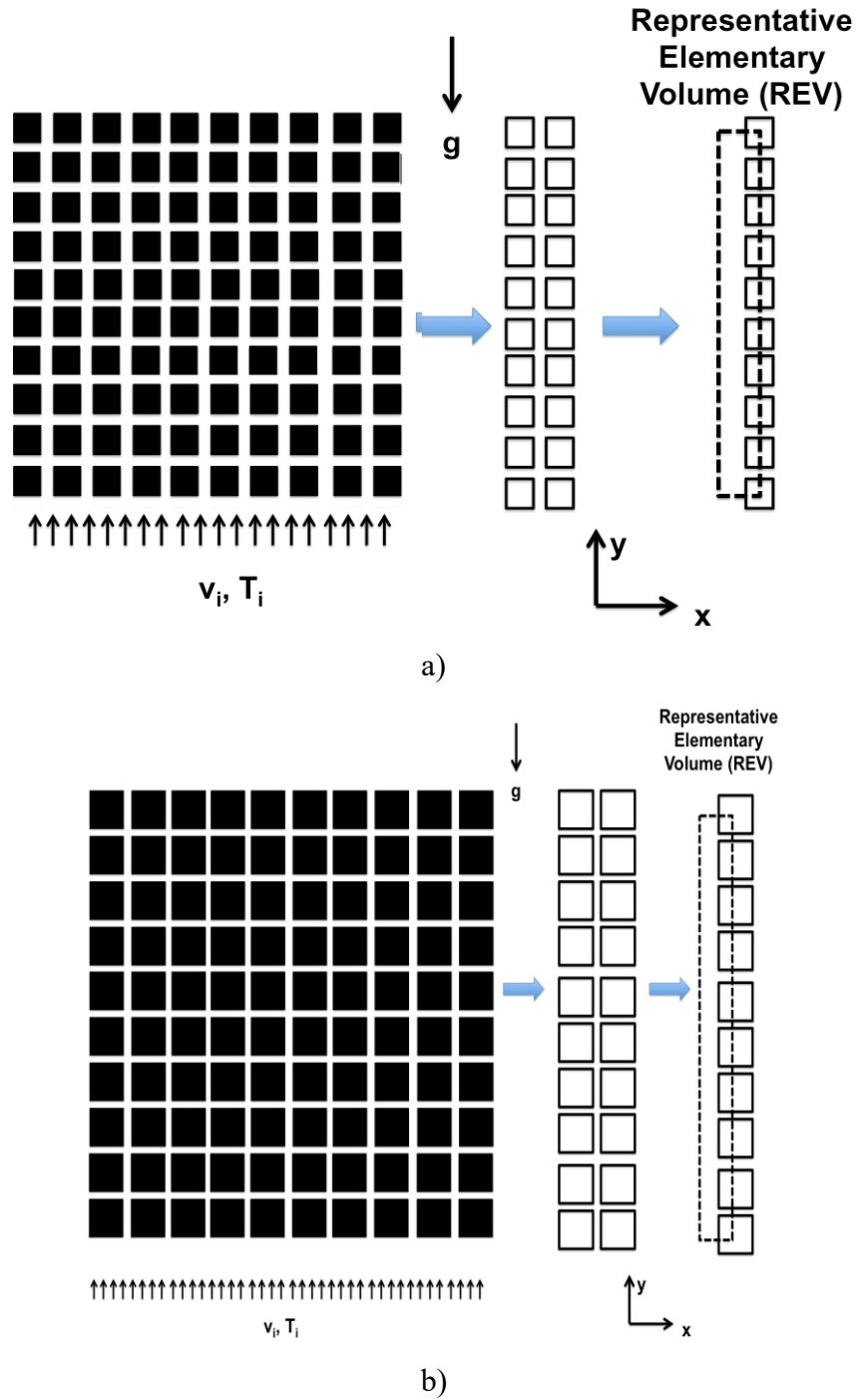


Figure 4.1. The considered and studied domain when a) $\varepsilon = 0.96$, b) $\varepsilon = 0.51$

4.1.2. Foam Structure

Some structural properties of foams, some typical geometrical features can be identified as ligaments, pores and cells, are given in Figure 4.2.

The structural parameters of metal foams are briefly defined below:

- PPI (Pores Per Inch): PPI is known as the number of pores per one inch of metal foam. It is also called as pore density or pore count. PPI of metal foams is a significant parameter for classification of metal foams.
- Strut: Strut (ligament) can be defined as the arms connecting cells of the metal foam. Ligaments are the metal rods that form the cellular structure of metal foams.
- Cell: Cells are defined as the void volumes surrounded by these ligaments.
- Pore: Metal foams consist of cells and solid arms connect them to each other. Open faces called as pores connect the voids inside the cells to each other.

Based on the performed literature survey, most of the researchers preferred to use porosity and PPI as structure indicator parameters of a metal foam. However, due to increasing number of metal foam manufacturers, it is observed that even if the porosity and PPI of two metal foams are identical, their ligaments or pore shapes might be different. For this reason, additional geometrical parameters should also be employed to specify metal foam precisely.

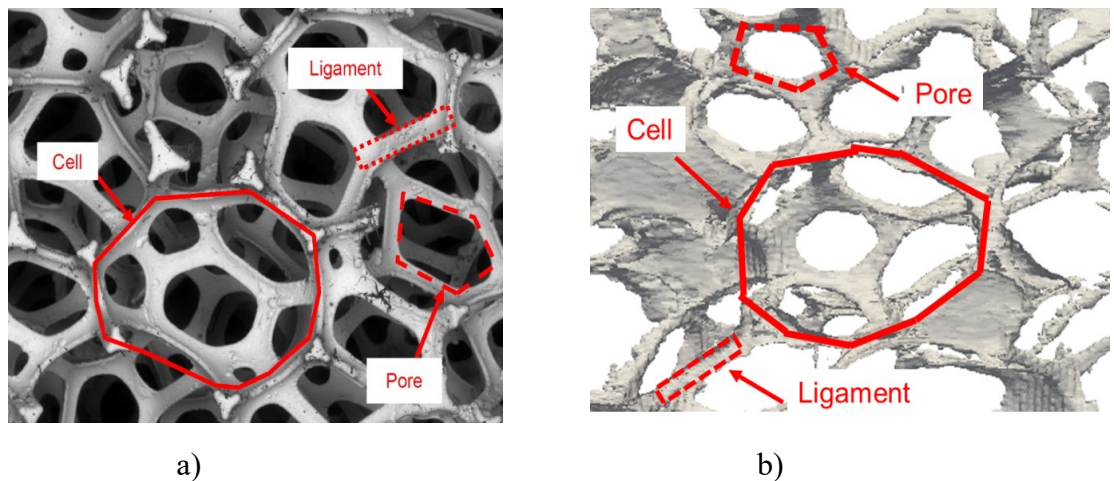
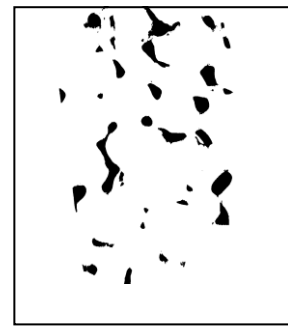
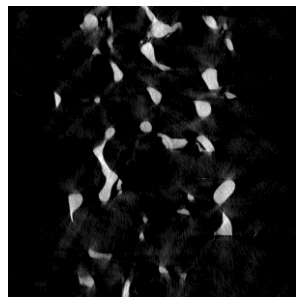


Figure 4.2. Structural properties of a foam, a) Scanning electron microscope (SEM) image of a foam (Taheri, 2015), b) the same structural properties of a foam built by using micro-tomography technique in the present study

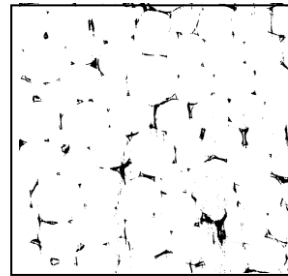
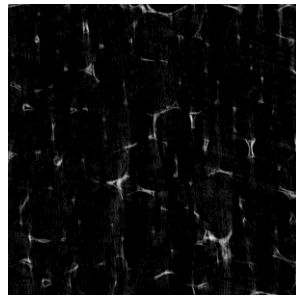
X-ray computed micro-tomography is one of the widely used non-destructive methods for analyzing structure of materials. In a micro-CT scanner, X-ray beam cone passes through the sample and is collected by a detector. The sample is rotated

providing a series of 2D projection images at different angles. After completing scanning process, the digital structure of sample may be obtained in computer environment from these 2D images. Some typical sample images were shown in Figure 4.3. To reduce the noise in the images and to distinguish fluid and solid phases clearly, a color threshold step is adjusted.

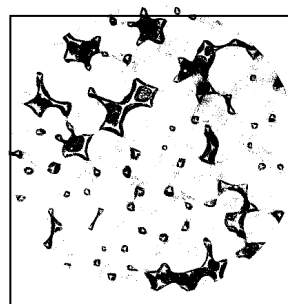
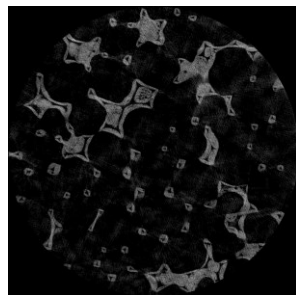
In this study, the aluminum and ceramic foam samples with pore density of 10, 20 and 40 PPI and with dimensions of 40x40x35 mm³ were received from a manufacturer as shown in Figure 4.4(a). Since, the numerical solution of velocity and pressure for the entire samples is expensive due to the limited computational resources, the tomography images obtained only for Representative Elementary Volume (REV) with size of 12x12x12 mm³ as shown in Figure 4.4(b), and shown that this is satisfactory for our purposes. The studied REV is scanned by 9x9 μm as pixel size and 13.6 μm as voxel length which means that the number of pixels in both x and y directions are 1400 and the number of images is 927. Following that, the obtained images are processed by imageJ software and 3D domain is obtained as StereoLithography (STL) file. The obtained STL files for each aluminum and ceramic foam structure analyzed in this study is shown in Figure 4.5. Structural properties of the analyzed foams such as surface area and ligament thickness are given in Table 4.1. After obtaining STL file, snappyHexMesh mesh generator of OpenFOAM CFD package is used to generate hexahedral mesh for the obtained 3D domain in computer environment. As a sample, the generated mesh for aluminum foam with 10 and 20 PPI is shown in Figure 4.6.



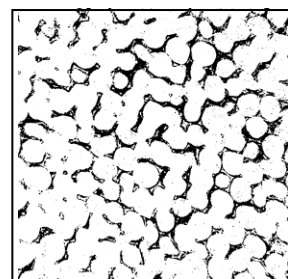
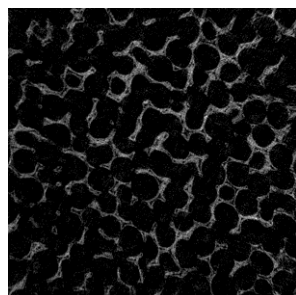
a)



b)



c)

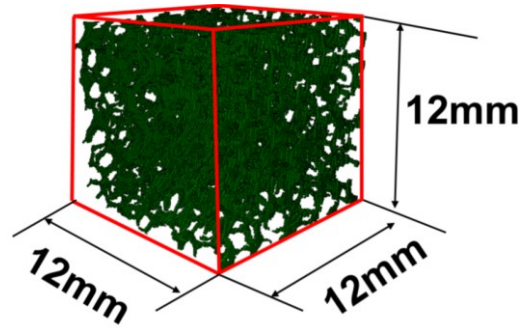


d)

Figure 4.3. The metal foam samples considered in this study; a) 10 PPI aluminum foam, b) 20 PPI aluminum foam, c) 20 PPI ceramic foam, d) 40 PPI ceramic foam. The images on the left were taken after scanning step while the images on the right shows after threshold step.

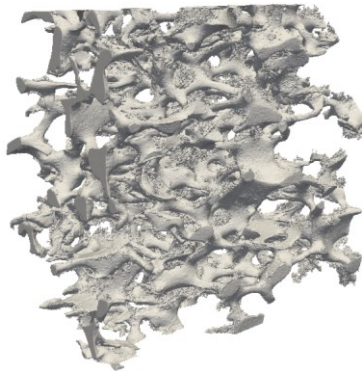


a)

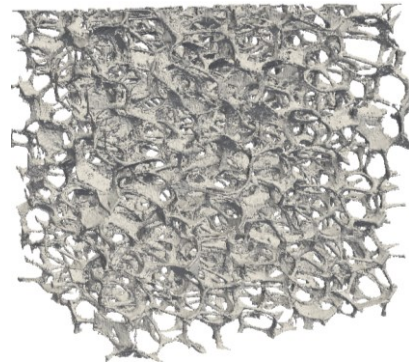


b)

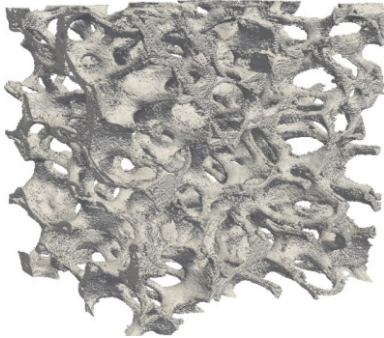
Figure 4.4. The considered 10 PPI and 20 PPI pore density metal foams a) the real structure, b) the domain generated in computer environment (20 PPI)



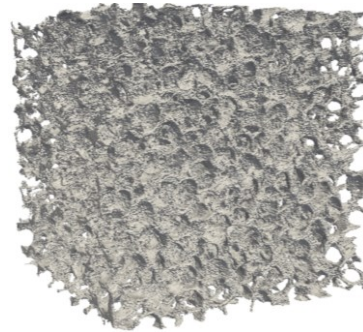
a)



b)



c)



d)

Figure 4.5. The foam samples generated in computer environment; a) 10 PPI aluminum foam, b) 20 PPI aluminum foam, c) 20 PPI ceramic foam, d) 40 PPI ceramic foam

Table 4.1. The values of structural properties of the considered metal foam samples in this study in x, y and z directions

Sample No #	1	2	3	4
Pore Density	10	20	20	40
Material	Aluminum	Aluminum	Alumina	Alumina
Porosity	0.90	0.95	0.84	0.84
Cell Diameter [m]	0.0044	0.0023	0.0021	0.0011
Strut Diameter [m]	0.00028	0.00019	0.00027	0.00027
Surface Area [m ²]	0.001500	0.002770	0.003764	0.006731

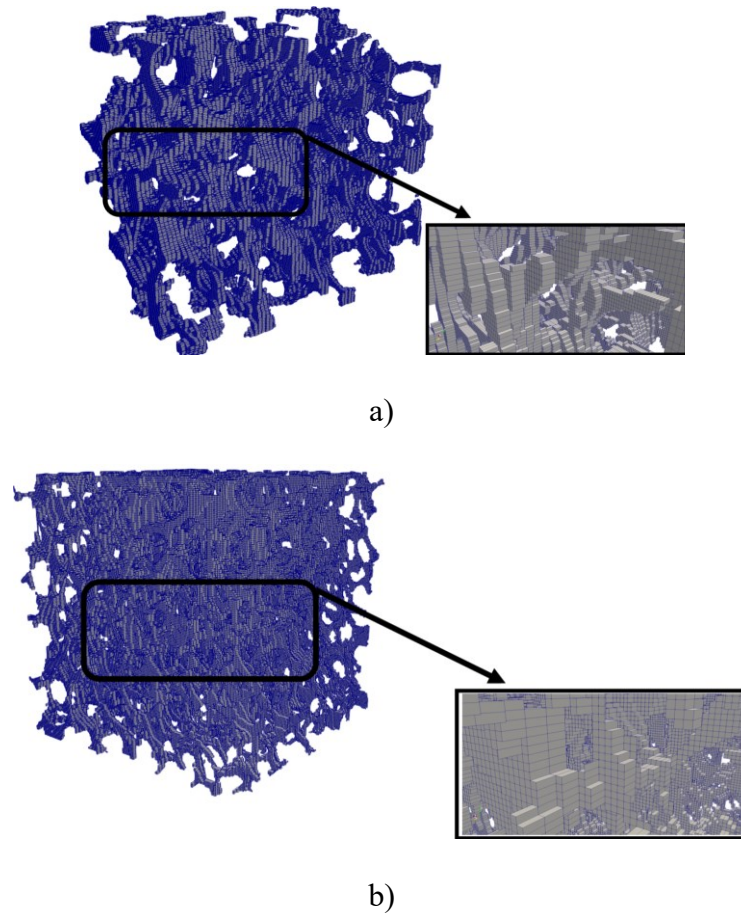


Figure 4.6. The domain generated in computer environment; a) 10 PPI metal foam, b) 20 PPI metal foam

After obtaining the mesh for aluminum foam with 10 and 20 PPI, and validating the results with the obtained studies, which will be explained in Chapter 6 and 7, the techniques considered generating mesh for aluminum metal foams will be repeated for ceramic foam structures, as well.

CHAPTER 5

GOVERNING EQUATIONS AND BOUNDARY CONDITIONS

Although the general forms of the governing equations were presented in Chapter 2, discussion on those equations and the boundary conditions for 2D and 3D domains are explained in this section. The assumptions considered in this study are explained in detail. The dimensionless form of the equations is derived. Determination of interfacial heat transfer coefficient and longitudinal and transverse thermal dispersion conductivity are given and discussed for both foam and periodic structures are given.

5.1. 2D Periodic Porous Structure

Pore level governing equations are considered in this study and following the obtaining the velocity, pressure and temperature fields, volume-averaged transport parameters will be evaluated. As a reminder, pore level governing equations given in general form in Chapter 2 are:

$$\vec{\nabla} \cdot \vec{u} = 0 \quad (2.14)$$

$$\rho_f \left[\frac{\partial \vec{u}}{\partial t} + \vec{u} \cdot \nabla \vec{u} \right] = -\vec{\nabla} p + \mu \vec{\nabla}^2 \vec{u} + \vec{F} \quad (2.15)$$

$$(\rho C_p)_f \left[\frac{\partial T_f}{\partial t} + \vec{u} \cdot \vec{\nabla} T_f \right] = k_f \nabla^2 T_f \quad (2.16)$$

$$(\rho C_p)_s \left[\frac{\partial T_s}{\partial t} \right] = k_s \nabla^2 T_s \quad (2.17)$$

The governing equations are conservation of mass (Eq. 2.14), conservation of momentum (Eq. 2.15), and conservation of energy equations (Eq. 2.16 and 2.17) for fluid and solid phases correspondingly. The governing equations under the considered assumptions in this study are given in the following parts.

5.1.1. Governing Equations and Boundary Conditions for Mixed Convection Heat Transfer in 2D Periodic Structure

Pore scale governing equations, including Boussinesq approximation, can be written as follows:

$$\vec{\nabla} \cdot \vec{u} = 0 \quad (5.1)$$

$$\rho_f (\vec{u} \cdot \vec{\nabla}) \vec{u} = -\vec{\nabla} p + \mu \vec{\nabla}^2 \vec{u} + \vec{g} \beta (T^f - T_{ref}^f) \quad (5.2)$$

$$(\rho C_p)_f (\vec{u} \cdot \vec{\nabla}) T^f = k_f \vec{\nabla}^2 T^f \quad (5.3)$$

$$\vec{\nabla}^2 T^s = 0 \quad (5.4)$$

where T^s and T^f represent solid and fluid temperature, respectively. The dimensionless form of the pore scale governing equations is solved to obtain velocity and temperature field in the voids. The dimensionless pore scale governing equations are:

$$\vec{\nabla}^* \cdot \vec{u}^* = 0 \quad (5.5)$$

$$\vec{u}^* \cdot \vec{\nabla}^* \vec{u}^* = -\vec{\nabla}^* p^* + \frac{1}{\text{Re}} \vec{\nabla}^{*2} \vec{u}^* + \text{Ri} \theta^* \vec{j} \quad (5.6)$$

$$\vec{u}^* \cdot \vec{\nabla}^* \theta_f^* = \frac{1}{\text{Re Pr}} \vec{\nabla}^{*2} \theta_f^* \quad (5.7)$$

$$\vec{\nabla}^{*2} \theta_s^* = 0 \quad (5.8)$$

where the dimensionless parameters used to obtain the above equations are defined as:

$$\text{Re} = \frac{\langle v_i \rangle w}{\nu \varepsilon}; Gr = \frac{g \beta \Delta T w^3}{\nu^2}; \vec{\nabla}^* = \nabla / H, \vec{u}^* = \vec{u} / v, P = \frac{pH}{\nu_i \mu_f}; \theta = \frac{T - T_i}{T_s - T_i}; \text{Ri} = \frac{Gr}{\text{Re}^2} \quad (5.9)$$

P and θ are the dimensionless pressure and temperature of the fluid, $\langle v_i \rangle$ is the averaged inlet Darcy velocity. H and w are the width and length of a cell and they are equal in this study. Re , Ri and ε are the main parameters which their effects are investigated in this study while Pr is taken constant as 0.71. The relation to calculate interfacial convective heat transfer coefficient is given in Chapter 2 as:

$$h_{\text{int}} = \frac{\frac{1}{V} \int_A k_f \nabla T dA}{\langle T \rangle^s - \langle T \rangle^f} \quad (2.48)$$

As can be seen from Eq. (2.48), the interfacial heat transfer coefficient is found based on temperature difference between $\langle T \rangle^s$ and $\langle T \rangle^f$. For a particle in porous media the pore scale Biot number can be defined as:

$$Bi = \frac{h_{\text{int}} l}{k_s} \quad (5.10)$$

where h_{int} , l and k_s are defined as solid-fluid surface interfacial heat transfer coefficient, characteristic length of particle and thermal conductivity of solid phase. The value of l (which can be particle size) is small and k_s is high for many solids in practical applications such as metals (in metal foams) and stones (in rock). Hence, Bi number takes small values (i.e. $Bi \ll 1$) permitting researchers to apply constant temperature assumptions for solid phase. Hence, there might be no need to solve heat conduction equation for solid. The same assumption has been used by many researchers such as Nakayama (2002), Ozgumus and Mobedi (2015) and Saito and de Lamos (2006).

Figure 5.1 shows the computational domain. By considering, $\vec{u}^* = u^* \vec{i} + v^* \vec{j}$ where u^* and v^* are dimensionless velocity components, the boundary conditions for the set of Eq. (5.5-5.8) mathematically can be expressed as follows:

For solid-fluid interface boundary:

$$u^* = v^* = 0; \theta = 1 \quad (5.11)$$

For left and right symmetry boundaries:

$$\frac{\partial u^*}{\partial X} = \frac{\partial v^*}{\partial X} = \frac{\partial \theta}{\partial X} = 0 \quad (5.12)$$

For inlet boundary:

$$u^* = 0; v^* = 1; \theta = 0 \quad (5.13)$$

For outlet boundary:

$$\frac{\partial u^*}{\partial Y} = \frac{\partial v^*}{\partial Y} = \frac{\partial \theta}{\partial Y} = 0 \quad (5.14)$$

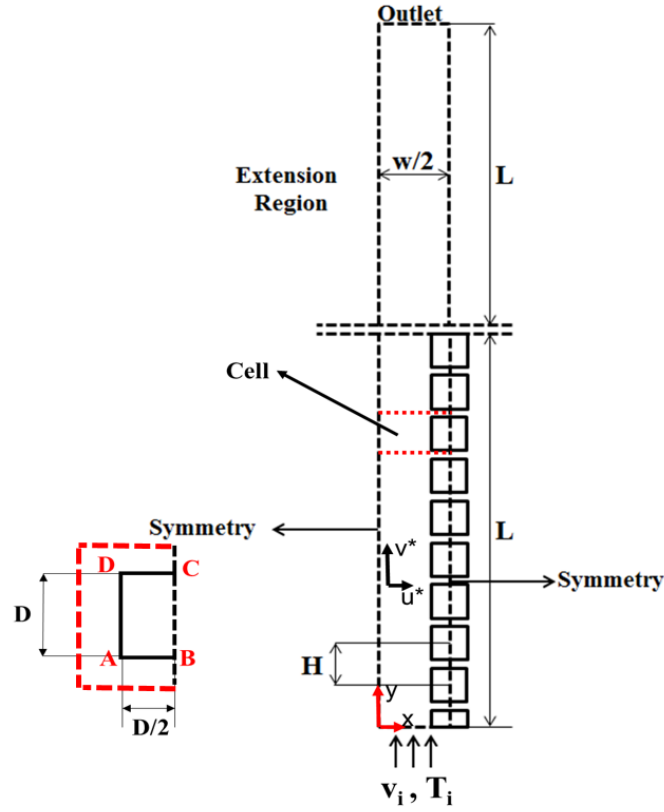


Figure 5.1. A view of the computational domain with boundary conditions

5.1.2. Determination of Interfacial Heat Transfer Coefficient

After determination of dimensionless temperature, the velocity and pressure under the above boundary conditions, Eq. (2.19) is used to obtain intrinsic volume average of quantity $\langle T \rangle^f$ for each cell, schematically shown in Figure 5.1. Furthermore, it is possible to rewrite Eq. (2.48) in the following form by using dimensionless temperature defined in Eq. (5.9):

$$\frac{h_{int} H}{k} \frac{(\langle T \rangle^f - \langle T_i \rangle^f)}{(\langle T \rangle^s - \langle T_i \rangle^f)} = \frac{l}{A_{sf}^*} \int_{A_{sf}^*} \frac{\partial \theta}{\partial n^*} dA^* \quad (5.15)$$

where A^* and n^* are dimensionless area and dimensionless normal direction. After some mathematical manipulations, the dimensionless local interfacial Nusselt number for a rod of the porous media can be obtained as:

$$Nu_L = \frac{\frac{1}{A_{sf}^*} \int_{A_{sf}^*} \frac{\partial \theta}{\partial n^*} dA^*}{1 - \langle \theta \rangle^f} \quad (5.16)$$

Furthermore, the local Nusselt number for three different surfaces of rods (\overline{Nu}_{Lc}) in REV is also calculated to find out the weighted effect of each surface on the heat transfer coefficient. \overline{Nu}_{Lc} is called as face local interfacial Nusselt number in this study. For instance, for surface which is shown by AB in Figure 5.1, mathematically, it can be defined as:

$$\overline{Nu}_{Lc} \Big|_{AB} = \frac{\frac{1}{|AB|} \int_A^B \frac{\partial \theta}{\partial n^*} dA^*}{1 - \langle \theta \rangle^f} \quad (5.17)$$

where $\overline{Nu}_{Lc} \Big|_{AB}$ is the average of Nusselt number on the surface of AB. If the same equation is applied to the surface of BC and CD of Figure 5.1, the summation of the obtained values will be equal to the result of Eq. (5.16) since the denominator is defined based on the volume averaged-temperature between fluid and solid in the cell and it is identical with the summation of face local interfacial Nu number of three surfaces:

$$\overline{Nu}_L = \overline{Nu}_{Lc} \Big|_{AB} + \overline{Nu}_{Lc} \Big|_{BC} + \overline{Nu}_{Lc} \Big|_{CD} \quad (5.18)$$

The above equation is used only to show the effect of each surface of the rods on the local Nusselt number and does not have any practical usage. The average interfacial Nu number of porous media is calculated by taking the arithmetical average of the local Nusselt number values of each rod from 2 to 10 in y-direction and it can be expressed as:

$$\overline{Nu} = \frac{\sum_{i=2}^{i=10} Nu_L(i)}{N} \quad (5.19)$$

where N is number of blocks in fully developed region. N is considered as 9 in this study, which is number of rods from 2nd to 10th.

5.1.3. Determination of Thermal Dispersion

Determination of thermal dispersion is explained in Chapter 2. As a reminder, the relations to obtain thermal dispersion in longitudinal direction is given as:

$$k_{dis,XX} = -\frac{1}{(\Delta T / L_{ref,XX})} \frac{\rho_f C_{pf}}{V} \int (T_f - \langle T_f \rangle) (\mathbf{v} - \langle \mathbf{v}_f \rangle) dV \quad (2.46)$$

In this study, only longitudinal thermal dispersion is calculated for 2D periodic structure. In Eq. (2.46), ΔT is the temperature difference between the inlet and the outlet of each cells, $L_{ref,XX}$ is the height of the cell, V is the total volume of the cell, ρ_f is density of the fluid and $C_{p,f}$ is the specific heat of the fluid at constant pressure, $\langle T_f \rangle$ and $\langle \mathbf{v}_f \rangle$ are volume-averaged temperature and velocity, respectively, while T_f and \mathbf{v}_f are pore level temperature and velocity. Thermal dispersion should be obtained by subtracting volume-averaged temperature and velocity from pore level temperature and velocity.

By considering dimensionless parameters given in Eq. (5.9), the relations for thermal dispersion can be obtained in dimensionless form as:

$$\frac{k_{dis}}{k_f} = -\frac{RePr}{\Delta\theta} \int (\theta - \theta_{avg}) (\mathbf{v}^* - \mathbf{v}_{avg}^*) dV^* \quad (5.20)$$

Like the evaluation of interfacial convective heat transfer coefficient, thermal dispersion both in longitudinal and transverse directions is obtained for each cell. After that, the average thermal dispersion of the porous media is calculated by taking the

arithmetical average of the local thermal dispersion values of each rod from 2 to 10 in y-direction and it can be expressed as:

$$\frac{\overline{k_{eff}}}{k_f} = \frac{\sum_{i=2}^{i=10} k_{eff}(i)}{N} \quad (5.21)$$

where N is number of blocks in fully developed region. N is considered as 9 in this study, which is number of rods from 2nd to 10th.

5.2. 3D Foam Structure

Like the 2D structure study, volume-averaged transport parameters are obtained for foam structures, as well. Permeability, interfacial convective heat transfer coefficient and thermal dispersion are evaluated. The techniques followed in this study are explained in this subheading.

5.2.1. The Governing Equations and the Boundary Conditions for Heat and Fluid Flow in Foam Structures

Following the mesh generation, flow in pore scale can be analyzed computationally. Air is considered as a Newtonian working fluid and flow is steady state. The effect of gravity is neglected. Under these assumptions, the governing equations of conservation of mass and momentum are solved to find velocity and pressure in the voids can be expressed as Eq. (2.14) – (2.17).

The considered boundary conditions are given in Figure 5.2. A uniform velocity is applied for the inlet section and the boundary condition of zero-gradient for velocity and temperature is applied for outlet referring to the negligible diffusion transport. A slip boundary condition is applied for the lateral walls of the channel to reduce the effect of wall on the flow field. The computational domain and boundary conditions are also shown in Figure 5.2(a). Although in Figure 5.2(a), the computational domain is shown for flow in y direction, similar domains can be employed for x and z directions to find out that the degree of isotropic feature of metal foam. Similarly, the same boundary conditions for the flow in y direction are also applied for the flow in x or z directions, as

shown in Figure 5.2(b). This means that the velocity and pressure fields in the same voids but for different principal flow directions obtained separately. In Volume Average Method, the volume averaged conservation of mass and momentum equations are used to find volume averaged velocity and pressure. The properties of air are taken to be 293.15K and Pr number is 0.71. The thermal conductivity of aluminum foam is 167 W/mK, and ceramic alumina foam is 18 W/mK.

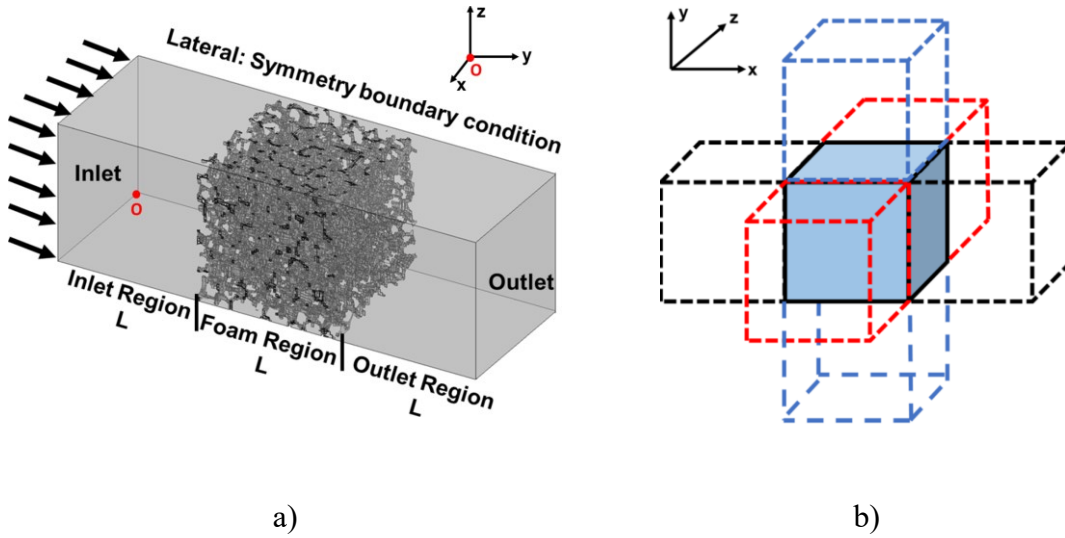


Figure 5.2. The considered domain a) with dummy inlet and outlet regions, and boundary conditions (O indicates the origin point), b) dummy regions in each direction

5.2.2. Determination of Permeability

Darcy – Brinkman – Forchheimer equation is considered for the evaluation of permeability. This equation is given in Chapter 2. For reminding, this equation can be rewritten here as:

$$\frac{1}{\varepsilon^2} \langle \vec{v} \rangle \cdot \nabla \langle \vec{v} \rangle = -\frac{1}{\rho_f} \nabla \langle p \rangle^f + \frac{\mu}{\varepsilon} \nabla^2 \langle \vec{v} \rangle - \frac{\mu}{\rho_f \overline{\overline{K}}} \langle \vec{v} \rangle - \frac{C}{\sqrt{\overline{\overline{K}}}} |\langle \vec{v} \rangle| \langle \vec{v} \rangle \quad (2.34)$$

where $\overline{\overline{K}}$ is permeability tensor and C is the inertia coefficient. In many porous media applications, the effects of the term in left hand side (convection term) and the second term in right hand side (which represents the effects of volume averaged pure viscous forces) are minor compared to other terms of Eq. (2.34). If a unidirectional flow is

considered, Eq. (2.34) takes the following form, which is usually called as Darcy – extended Forchheimer equation:

$$\langle \nabla p \rangle^f = -\frac{\mu}{K} \langle u \rangle - \frac{C}{\sqrt{K}} \rho \langle u \rangle^2 \quad (5.22)$$

Eq. (5.22) can be expressed in dimensionless form as follows:

$$\Pi = A + B \text{Re} \quad (5.23)$$

The dimensionless parameters of A, B and Π are defined as:

$$\Pi = -\frac{d_c^2}{\langle u \rangle \mu_f} \frac{d \langle p \rangle^f}{dx} \quad A = \frac{d_c^2}{K} \quad B = C \left(\frac{d_c^2}{K} \right)^{1/2} \quad \text{Re} = \frac{\rho_f \langle u \rangle d_c}{\mu_f} \quad (5.24)$$

where d_c is the cell diameter selected as characteristic length. Both cell and pore diameters can be selected as characteristic length, where in this study cell diameter is chosen. For determination of average pore and cell diameters, the diameter of some typical random cells in the metal foam in computer environment is measured. The average of measured values is accepted as pore or cell size. The average cell diameters were found to be 2.2 mm for 20 PPI and 4.5 mm for 10 PPI. A sample of the cell for which the pore diameter measured is shown in Figure 5.3.

For determining the values of K and C, two methods as Linear (or dimensionless linear) and Parabolic Approaches are used in the literature. Dimensionless Linear Approach enabling the prediction of the critical Reynolds number for separation of Darcy from non-Darcy region is used in this study (Ucar et al., 2015). In this method, firstly, the volume-averaged velocity and pressure drop at cross-sections perpendicular to the flow direction is calculated. Then, the change of pressure drop in flow direction is drawn to obtain the pressure gradient in flow direction by employing a proper curve fitting method and the dimensionless pressure drop for the specified Re number can be obtained from Eq. (5.23). The same method can be employed to determine dimensionless pressure drop for different Reynolds numbers. Then, the dimensionless pressure can be plotted against Re number and finally by applying a proper curve fitting

method, the Eq. (5.23) and consequently the coefficients of A and B can be found. Finally, the permeability and inertia coefficients can be easily obtained from A and B values.

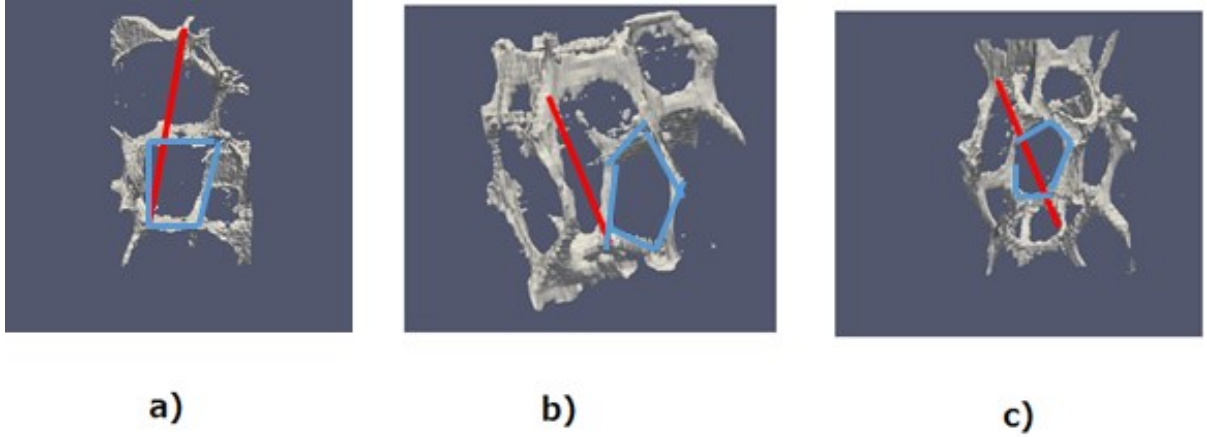


Figure 5.3. Determination of pore diameter by considering three randomly selected cells. Red line shows cell diameter, blue line shows pore diameter

5.2.3. Determination of Interfacial Convective Heat Transfer Coefficient in Foam

For determining interfacial convective heat transfer coefficient, Eq. (2.48) given in Chapter 2 should be considered. Interfacial convective heat transfer coefficient, h_{int} , can be obtained by using:

$$h_{\text{int}} = \frac{\frac{1}{V} \int_{A_{sf}} k_f \nabla T dA}{\langle T \rangle^s - \langle T \rangle^f} \quad (2.48)$$

It should be reminded that, $\langle T_f \rangle$ and $\langle T_s \rangle$ are volume-averaged temperatures of fluid and solid phases, respectively. As it is shown in Figure 5.4(a) and (c), the number of control volume may be increased by slicing the domain into thinner pieces. In this study, 5 and 20 control volumes are considered and the values of $\langle T_f \rangle$ and $\langle T_s \rangle$ are obtained. In Eq. (2.48), A_{sf} is the interface area (wet area) between solid and fluid phases. While evaluating interfacial convective heat transfer coefficient, constant solid temperature is taken; therefore, $\langle T_s \rangle$ is constant for this particular study.

5.2.4. Determination of Thermal Dispersion

Recalling Eq. (2.45) as a starting point, thermal dispersion can be calculated by following Energy equations for XX direction:

$$-\rho_f C_{p,f} \nabla \cdot \langle T' \vec{u}' \rangle = k_{dis} \nabla^2 \langle T \rangle \quad (2.45)$$

$$k_{dis,XX} \frac{d\langle T_f \rangle}{dx} = -\frac{\rho_f C_{pf}}{V} \int (T_f - \langle T_f \rangle) (u - \langle u_f \rangle) dV \quad (5.25)$$

if we assume a linearly changing macroscopic temperature in one space direction then, it is possible to write:

$$\frac{d\langle T_f \rangle}{dx} = \frac{\Delta T_{xx}}{L_{ref,x}} \quad (5.26)$$

and from this assumption, it is possible to find thermal dispersion as below:

$$k_{dis,XX} = -\frac{1}{(\Delta T_{xx} / L_{ref,x})} \frac{\rho_f C_{pf}}{V} \int (T_f - \langle T_f \rangle) (u - \langle u_f \rangle) dV \quad (5.27)$$

Similarly, assuming a linear temperature gradient through YY direction:

$$\frac{d\langle T_f \rangle}{dy} = \frac{\Delta T_{yy}}{L_{ref,y}} \quad (5.28)$$

and transverse thermal dispersion can be obtained as:

$$k_{dis,YY} = -\frac{1}{(\Delta T_{YY} / L_{ref,y})} \frac{\rho_f C_{pf}}{V} \int (T_f - \langle T_f \rangle) (u - \langle u_f \rangle) dV \quad (5.29)$$

In this study, the temperature of the solid structure is taken as constant. A linear temperature in transverse direction is generated to make sure heat is only transferred in

transverse direction. The procedure followed to generate sub-volumes is explained in Figure 5.4.

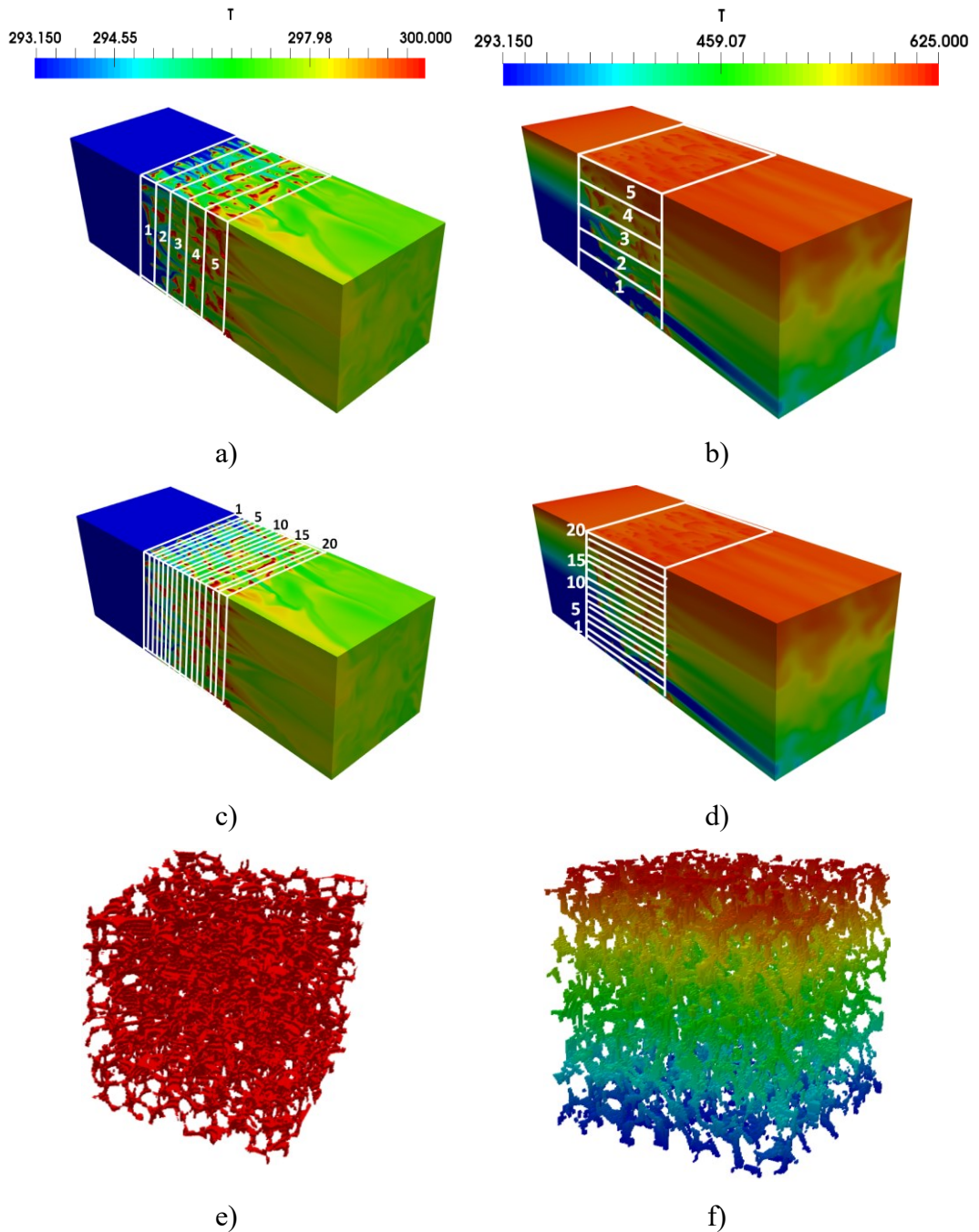


Figure 5.4. Determination of volume-averaged parameters by considering volumes through the domain a) interfacial convective heat transfer coefficient and longitudinal thermal dispersion by 5 volumes, b) determination of transverse thermal dispersion by 5 volumes, c) interfacial convective heat transfer coefficient and longitudinal thermal dispersion by 20 volumes, d) determination of transverse thermal dispersion by 20 volumes, e) the considered solid boundary condition for interfacial convective heat transfer coefficient and longitudinal thermal dispersion, f) the considered solid boundary condition for transverse thermal dispersion

The temperature contour of the solid structure in this study is shown in Figure 5.4(e) and 5.4(f) for longitudinal and transverse thermal dispersion calculation, respectively. It should be reminded that, while evaluating longitudinal thermal dispersion, volumes will be taken through the flow direction, as shown in Figure 5.4(a) and (c). For calculating transverse thermal dispersion, the volumes are chosen perpendicular to the flow direction and the volumes are shown in Figure 5.4(b) and (d).

CHAPTER 6

COMPUTATIONAL DETAILS

The solution technique followed to obtain volume-averaged parameters for 2D periodic structure and 3D foam structures are explained separately at the sections below in this chapter. For 2D periodic structure, the details of the computational method, in terms of such as the scheme considered and convergence criteria, are described. Following that, grid independency technique will be explained. For 3D foam structures, like the 2D periodic structure, firstly, the scheme and the grid details are explained. Then, the written computer code is explained to evaluate volume-averaged transport parameters.

6.1. 2D Periodic Structure

Pore scale governing equations are solved for the considered REV shown in Figure 4.1, by a commercial Finite Volume code, ANSYS Fluent 15.0. The power law scheme is employed for the discretization of the convection terms in the momentum and energy equations. Semi-Implicit Method for Pressure Linked Equations (SIMPLE) is widely used pressure–velocity coupling scheme; which is suitable for incompressible flows. The absolute convergence criterion is set to 10^{-7} for continuity and the momentum equations, 10^{-12} for the energy equation. Furthermore, the velocity and temperature profiles at $Y = 3, 6$ and 9 are checked for different iteration steps and the solution is accepted as converged when residuals between two iteration steps are less than 10^{-6} for these profiles is observed. As it was mentioned before an extension region is considered downstream of the porous region to prevent computational difficulties at the outlet of porous region due to reverse flows. Our computational experience showed that the length of L is sufficient for the length of this dummy region.

Grid independency study is done for two limit cases of this study as ($Ri = 0.01$, $Re = 100$) and ($Ri = 10$, $Re = 500$) and for porosity of 0.96 , since this configuration has the most complex flow for the considered problem. The grid number in x -direction is taken from 10 to 260 while in Y direction it changes from 190 to 4560 respectively. The interfacial Nu number is calculated and compared for the considered different number

of grids. The results are presented in Figure 6.1. The average interfacial Nu number does not highly change after grid number of 220x4180. It is observed that the grid number of 260x4940 is sufficient to obtain accurate results and observe flow reversals in the channel in details.

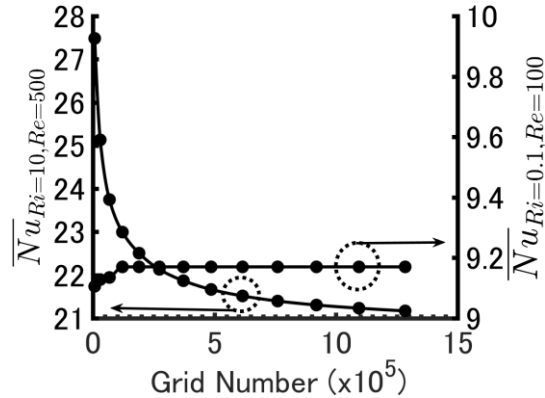


Figure 6.1. Grid independence study for $Ri = 0.1 - Re = 100$, and $Ri = 10 - Re = 500$ when $\varepsilon = 0.96$

6.2. 3D Foam Structure

Determination of volume-averaged properties is lengthy procedure. Firstly, the domain should be generated using micro-tomography images. The obtained images are processed using imageJ software. Firstly, obtained images are segmented into fluid and solid phases. This process is done using black and white regions given in Figure 4.3. After that, the generated 3D domain is used to solve the governing equations.

Like 2D periodic structure part, pore scale governing equations are solved for REV given in Figure 4.4(b). Dummy regions are added to the computational domain upstream and downstream of the metal foam section to reduce the inlet and outlet effects as shown in Figure 5.2(a). The dimensions of this region are taken the same as the length of metal foam region. OpenFOAM 2.3.1 is used to solve the continuity and momentum equations for the flow in the voids of metal foams. This code has been written based on the finite volume approach. The coupling of velocity and pressure is treated by SIMPLE algorithm. The convergence criterion is set to 10^{-6} for all the terms in the governing equations.

For the evaluation of volume-averaged transport parameters, a separate computer code in Python language, which offers an easy maintenance and the required flexibility, is written. The written code is considered in 3 parts. The general flow-chart of the code is given in Figure 6.2. The open-source post-processing software of

OpenFOAM, ParaView, also offers Python shell. Therefore, the code written can be applied to all case files considered in this study. First part of the code is developed for permeability (Figure 6.3), the second and the third part of the code are written for longitudinal and transverse thermal dispersion respectively (Figure 6.4 and Figure 6.5).

The image processing on a computer environment is a challenging task. High amount of RAM and CPU resources are required to obtain high quality 3D views. The number of images slices taken through the domain sets the voxel length (i.e. the distance between two slices). No doubt that the decrease of distance between the images increases the accuracy of the results, however, the high number of images considerably affects the required computational resources to process images. For this reason, the number of slices must be chosen wisely for the sake of computational resources. In this study, the effect of the number of images on the results is studied and an obtained result for $Re = 600$ is given in Figure 6.6(a). As can be seen, for small number of images (15 images) the permeability in flow direction changes by increasing number of images, however; after a reasonable number of images, increasing the number further does not influence the results. It is seen that 309 images per 12.32 mm (i.e., $40 \mu m$ as voxel length) might be sufficient to obtain acceptable permeability and inertia coefficient values for the problem considered in this study.

The permeability and inertia coefficient values are calculated for grid numbers from $24 \times 24 \times 24$ to $250 \times 250 \times 250$ number and the changes for $Re = 600$ are shown in Figure 6.6(b) and 6.6(c), respectively. As it can be seen, the cell number around 7000000 is sufficient to have sufficient accurate results.

In addition to the grid check explained in Figure 6.6, another check for the grid can be done considering the change of digital porous structure with number of grids in transverse direction, as shown in Figure 6.7. By changing of grids from $48 \times 48 \times 48$ to $148 \times 148 \times 148$, the generated structure considerably changes. Not only the size but also the location of solid phase and voids change. However, by changing of grids from $148 \times 148 \times 148$ to $192 \times 192 \times 192$ or $250 \times 250 \times 250$, the size and location of ligaments do not vary indicating independency of generated structure from the mesh.

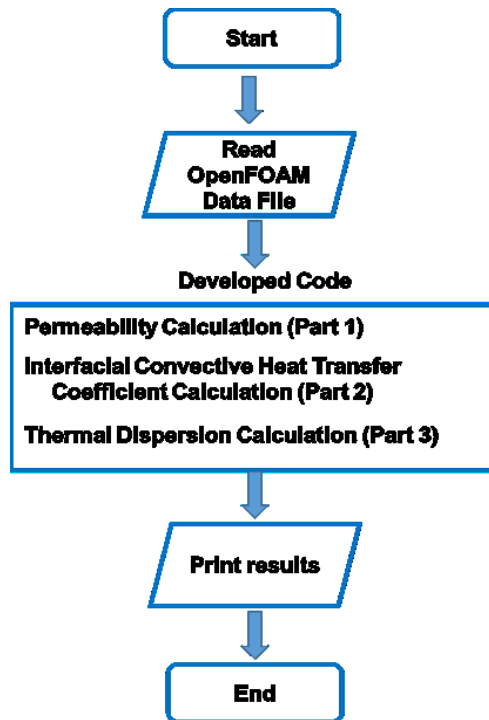


Figure 6.2. The general flow chart of the code written for evaluating volume averaged transport parameters

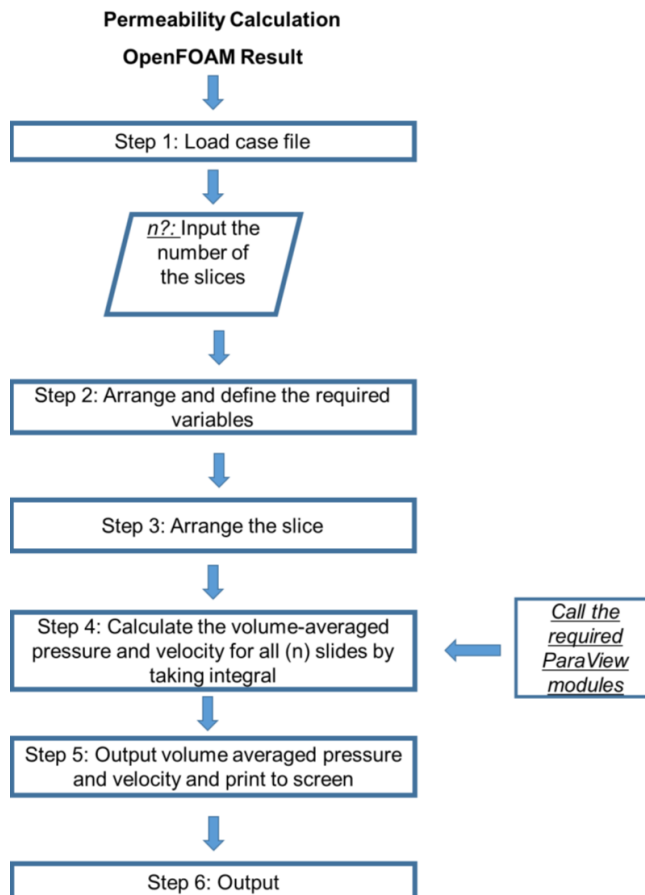


Figure 6.3. The flow chart considered in the code to calculate permeability and inertia coefficient

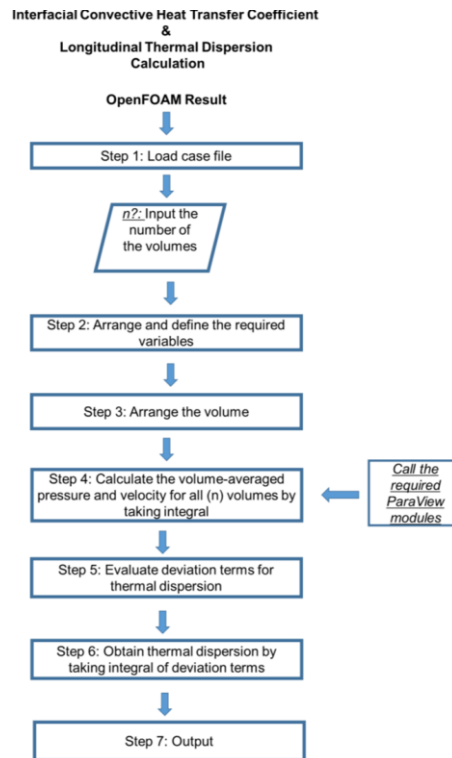


Figure 6.4. The flow chart considered in the code to calculate interfacial convective heat transfer coefficient and longitudinal thermal dispersion

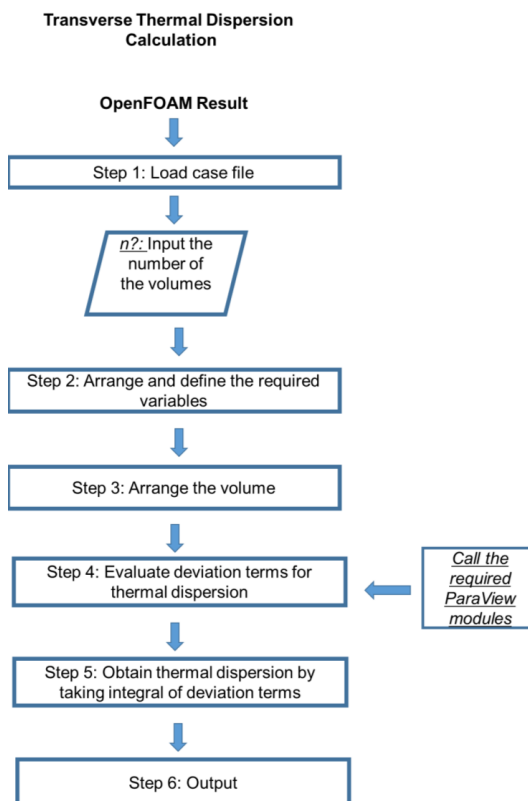
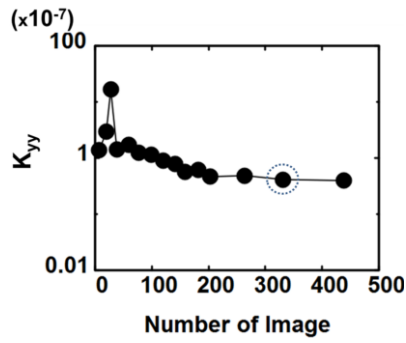
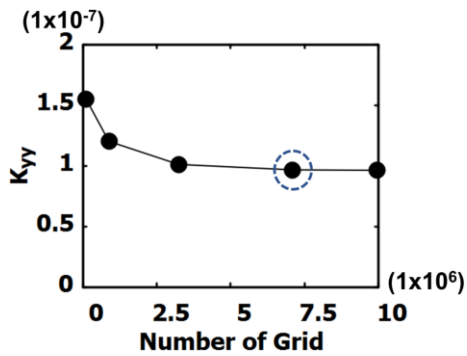


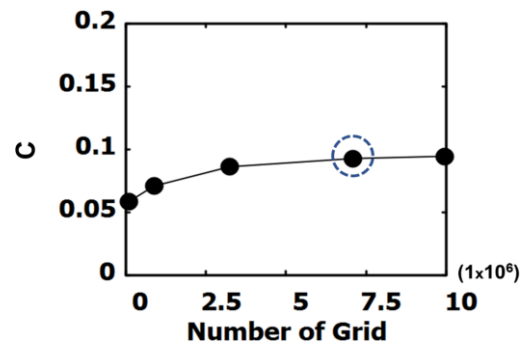
Figure 6.5. The flow chart considered in the code to calculate transverse thermal dispersion



a)



b)



c)

Figure 6.6. Validation of number of image and grids for $Re = 600$; a) the change of permeability in z direction respect to number of images in flow direction, b) the change of permeability in z direction respect to grid number, c) b) the change of inertia coefficient in z direction respect to grid number.

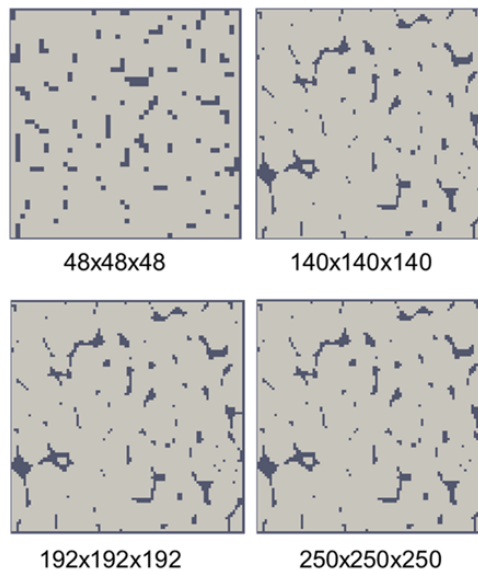


Figure 6.7. The change of the generated structure of aluminum foam with $PPI=20$ with number of grids for the surface with $y = 3L/2$ (black is solid region while gray represents void).

Furthermore, grid independency is analyzed in terms of interfacial convective heat transfer coefficient and thermal dispersion for $Re = 600$. The change of interfacial convective heat transfer coefficient with cell number for 20 PPI aluminum foam is given in Figure 6.8(a). As seen, after a point, there is no meaningful change in the value of interfacial convective heat transfer coefficient. Therefore, $192 \times 192 \times 192$ number of cells can be considered.

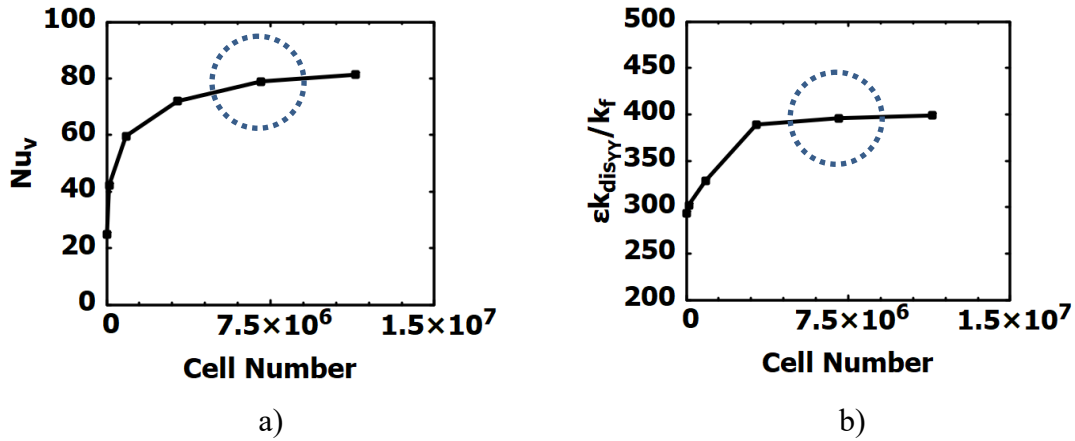


Figure 6.8. The change of volume-averaged transport parameters with cell number for 20 PPI aluminum foam, a) interfacial convective heat transfer coefficient, b) thermal conductivity

All computational methods explained here are repeated for all principal axes. Also, all foam samples considered in this study are checked and analyzed. By considering open-source CFD solver, OpenFOAM, governing equations are solved at computer clusters of Shizuoka University Nakayama-Kuwahara-Sano Lab., TUBITAK ULAKBIM TRUBA sources and Kyoto University Super Computer Facility.

CHAPTER 7

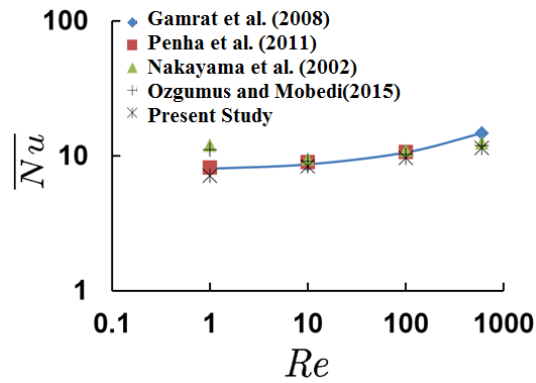
RESULTS AND DISCUSSION

After applying assumptions, obtaining the governing equations, volume – averaged transport parameters can be observed. In this chapter, the results will be reported. Discussions based on the governing parameters will be made. This chapter starts with the results of interfacial convective heat transfer coefficient and thermal dispersion of 2D periodic structures. Following that, the results for 3D foam structures are shown.

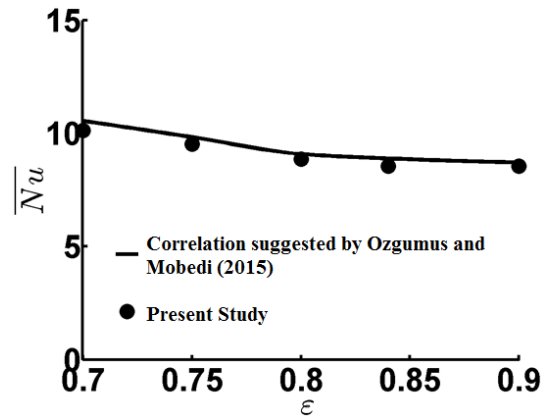
7.1. 2D Periodic Structure

7.1.1. Interfacial Convective Heat Transfer Coefficient

The code and method employed in this study validated by using the reported studies in the literature. As it was mentioned before, most of studies on interfacial convective heat transfer coefficient were performed for forced convection in porous media. Figure 7.1(a) shows the comparison of the present study with the reported results of the fully developed forced convection of porous media consisting of square rods and has porosity of 0.75. The comparison is accomplished for Ri number of 0.0001 presenting a forced convection heat transfer. The present results are compared with the results reported by Nakayama et al. (2002), Gamrat et al. (2008), Penha et al. (2011) and Ozgumus and Mobedi (2015). A reasonably good agreement between the present results and those reported studies can be observed. The results of the present study are also validated by comparing with the relationship suggested in the study of Ozgumus and Mobedi (2015) as shown in Figure 7.1(b). The correlation in their study was given for forced convection heat transfer when Re changes between 1 and 100. The correlation is valid for porosity values between 0.7 and 0.90. A good agreement between Ozgumus' suggested correlation and the present study for $Ri = 0.0001$ and $Re = 100$ can also be observed.



a)



b)

Figure 7.1. Validation of the obtained results, a) the comparison of present study with reported results for average interfacial Nusselt number of fully developed forced convection, b) comparison of average interfacial Nusselt number with correlation suggested by Ozgumus and Mobedi (2015) when $Ri = 0.0001$ and $Re = 100$

Figure 7.2 shows the velocity and the temperature fields for a mixed convection heat transfer in the porous media with $\epsilon = 0.96$, $Ri = 0.01$. Figure 7.2(a) shows the streamline and temperature distribution for heat and fluid flow with $Ri = 0.01$ and $Re = 100$. For better visualization of streamline and temperature contours, a close-up view is also given where the channel width is shown twice as big as the original size. Due to the low Ri number and buoyancy effect, the forced convection is dominant and no reverse flow occurs inside the porous media. The fluid flows upward in the center of the voids between the blocks while the air, close to the blocks, enters the gap between them. A secondary flow occurs on the top of each rod causing the reduction of heat transfer rate from the top surface of rod to the surroundings. The value and contribution of face local interfacial Nusselt number of each faces (i.e. A - B, B - C and C - D) of seventh rod onto \overline{Nu}_L can be seen in the table of Figure 7.2(a). As it can be seen from the table, heat

is mainly transferred from the surface B-C and the effect of the surface C-D to the local interfacial Nusselt number is small compared to the other surfaces due to the occurrence of secondary loop.

By increasing of Re number from 100 to 500, no notable change in the general behavior of the flow is observed due to low Ri number as can be seen from Figure 7.2(b). There is nearly no considerable change in the contribution of \bar{Nu}_{Lc} from surfaces, just the contribution from surface B-C a little bit increases while the contribution of surface C-D decreases compared to the case of Figure 7.2(a). For Re = 500, the flow between the blocks becomes straighter and vortices occurring in the vertical gaps between blocks become larger. The comparison between the temperature contours of porous media of Re = 100 and 500 (Figure 7.2(a) and 7.2(b)) shows that the cold fluid moves long distance in vertical direction. It should be mentioned that heat transfer coefficient is defined based on the surface and inlet temperature difference. That is why the interfacial convective heat transfer coefficient may be expected to be higher for a flow with Re = 500 compared to Re=100.

The structure of porous media in Figure 7.3(a) is the same with Figure 7.2(a); however, the Ri number is increased from 0.01 to 10. Figure 7.3(a) shows the flow and temperature distributions for Re = 100. As it can be seen, by increasing of Ri number from 0.01 to 10, reverse flows in the middle of the channel occur due to the strong buoyancy effect. A close – up picture of the flow reversal for the fourth rod of the channel is given in Figure 7.3(a). The shape of the secondary flows in the middle and top of the rods can be observed clearly. The contribution of each surfaces of seventh rod on heat transfer rate from rod to air when Ri = 10 and Re = 100 shown in Table of Figure 7.3(a). Again, the same contribution observed for previous figures can be seen also for Figure 7.3(a).

The flow and temperature fields for Re = 500 and Ri = 10 are shown in Figure 7.3(b). By increasing of Re from 100 to 500, the size of reverse flows become larger both in longitudinal and transverse directions but occurs at a little bit far from the inlet region. The comparison between Figures 7.3(a) and 7.3(b) indicates that the cold fluid moves longer distance in vertical direction and the interfacial convective heat transfer coefficient is expected to be increased when the Re value is increased from 100 to 500. The interesting point of Figure 7.3(b) is a secondary flow occurs on the vertical wall of

the rods (face BC). Hence, this secondary flow, heat transfer coefficient on the BC surface is reduced.

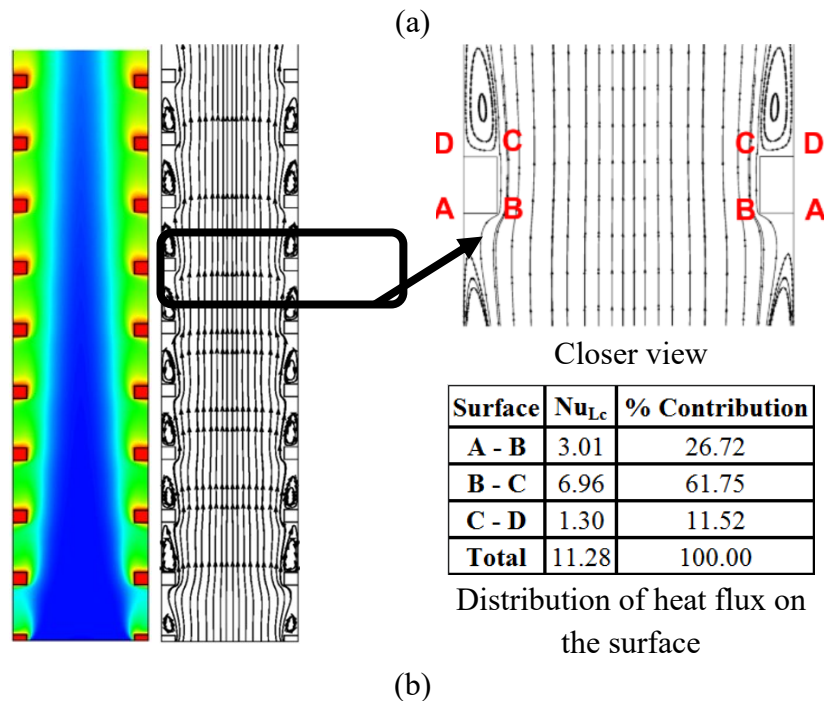
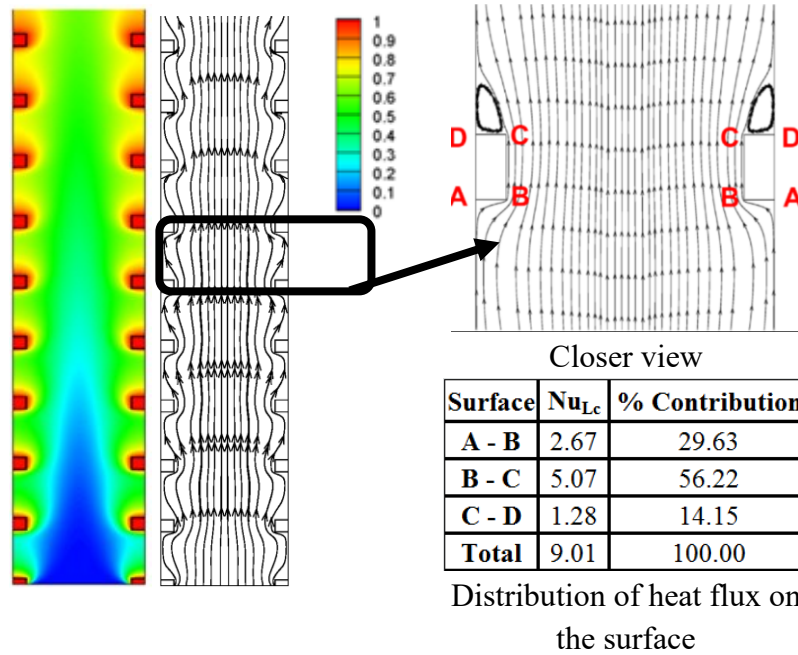
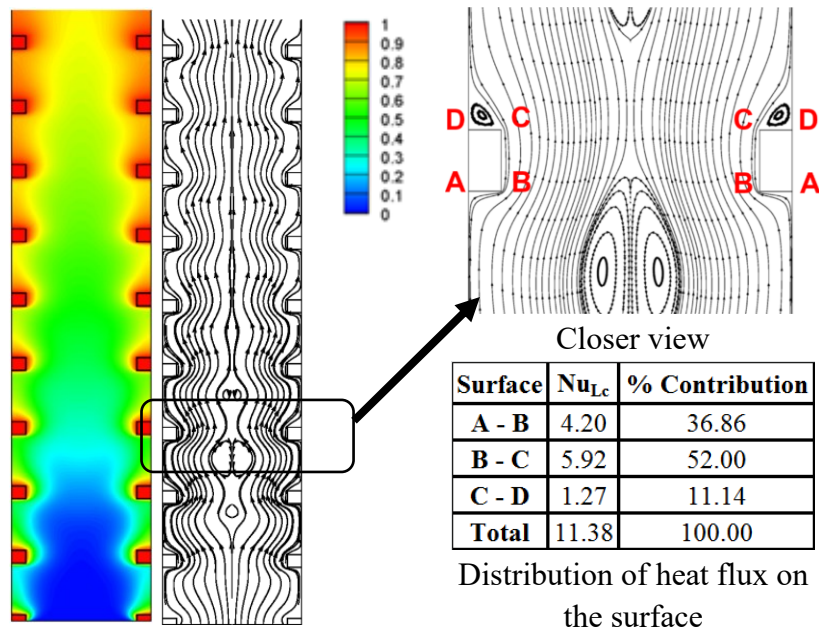
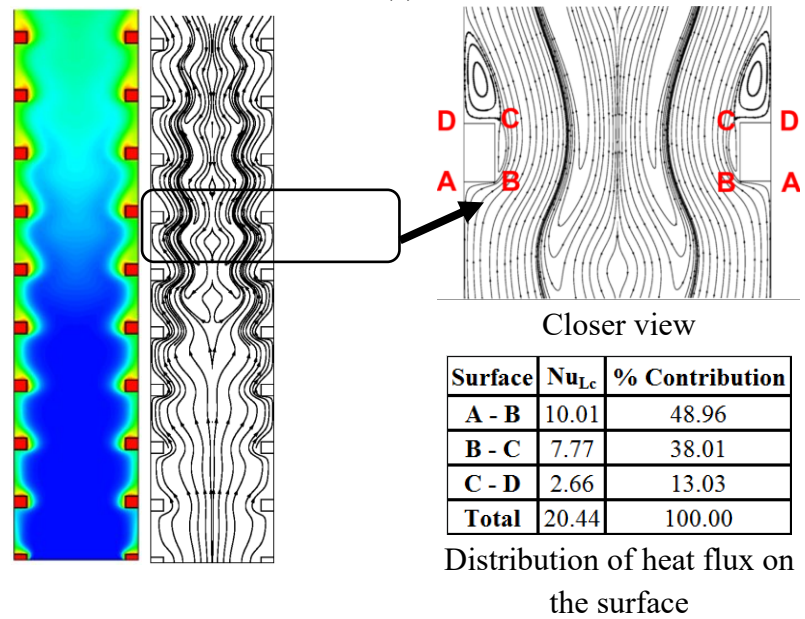


Figure 7.2. Streamlines and temperature distribution in porous media with $\varepsilon = 0.96$ and $Ri = 0.01$, a) $Re = 100$, b) $Re = 500$

Like the previous figures, the contribution of each surface on the interfacial heat transfer coefficient is shown in the same figure. It is seen that the heat transfer from surface B-C decreases compared to Figure 7.3(a), as expected. As secondary loop occurs near the surface B-C and heat is mainly transferred from surface A-B and surface C-D still has the lowest effect on the interfacial heat transfer coefficient.



(a)



(b)

Figure 7.3. Streamlines and temperature distribution in porous media with $\varepsilon = 0.96$ and $Ri = 10$, a) $Re = 100$, b) $Re = 500$

Figure 7.4 shows the streamline and temperature contours for the porous media with porosity of 0.51 when $Ri = 0.01$. Figure 7.2(a) shows the temperature field and streamline for $Re = 100$. Like the Figure 7.2(a), due to the low buoyancy effect, the streamlines are straight and no flow reversal occurs in the middle portion since forced convection is dominant heat transfer mechanism. Secondary flow occurs not only on the top but also on the bottom side with equal area. Due to high heat transfer area between

the solid and fluid phases, the temperature of fluid enters to the porous media attains to the solid temperature faster than Figures 7.2(a) in which $\varepsilon = 0.96$. Another interesting

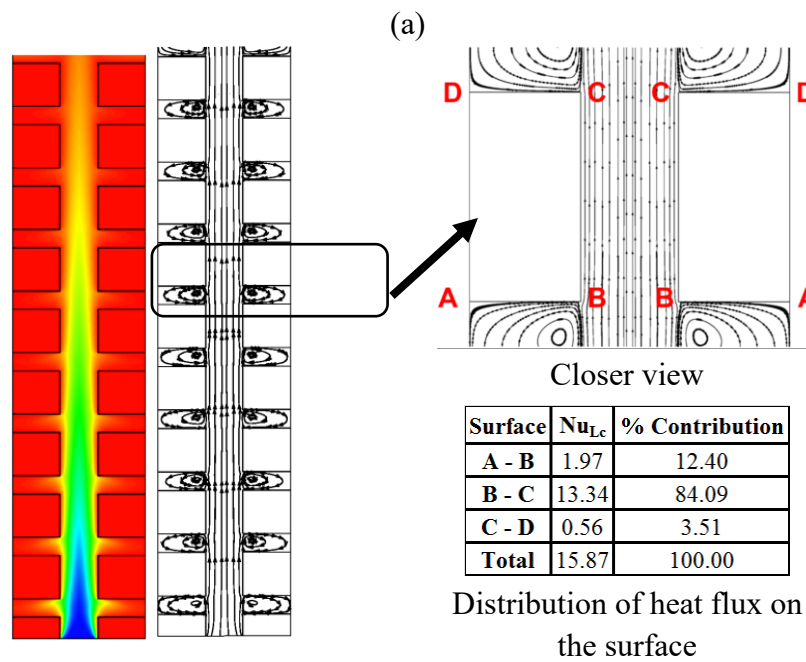
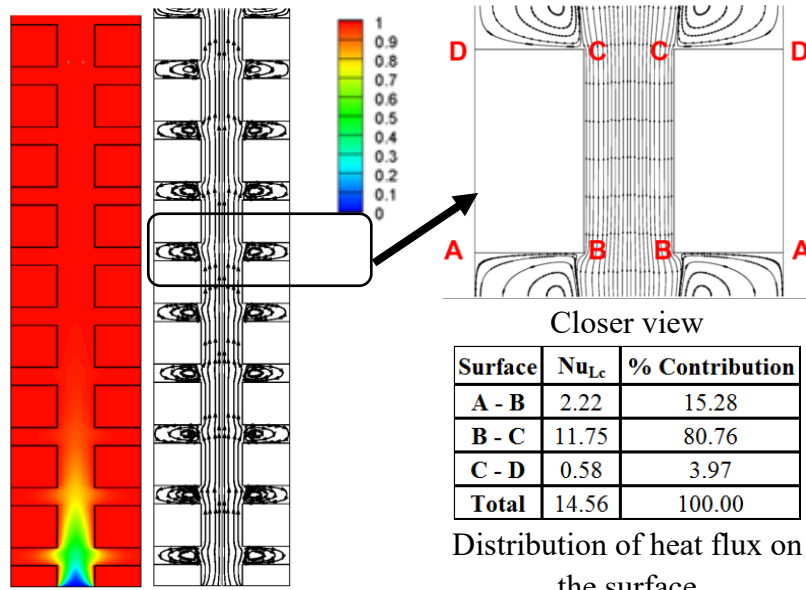


Figure 7.4. Streamlines and temperature distribution in porous media with $\varepsilon = 0.51$ and $Ri = 0.01$, a) $Re = 100$, b) $Re = 500$

point of Figure 7.4(a) is the contribution of heat transfer of each surface into the total heat transfer rate from rod. The surface B-C is the most important surface with 80.76% while the effect from surfaces A-B and C-D totally is 19.26%. By increasing of Re number from 100 to 500, there is no notable change in the velocity field inside the channel as seen from Figure 7.4(b). However, the cold fluid entering to the porous media moves longer distance in vertical direction due to high value of Re number (i.e.,

Re = 500) and then higher interfacial Nusselt value may be expected for Re = 500. There is no considerable change in contribution from each surface when it is compared with Figure 7.4(a), as it can be seen from the Table of Figure 7.4(b).

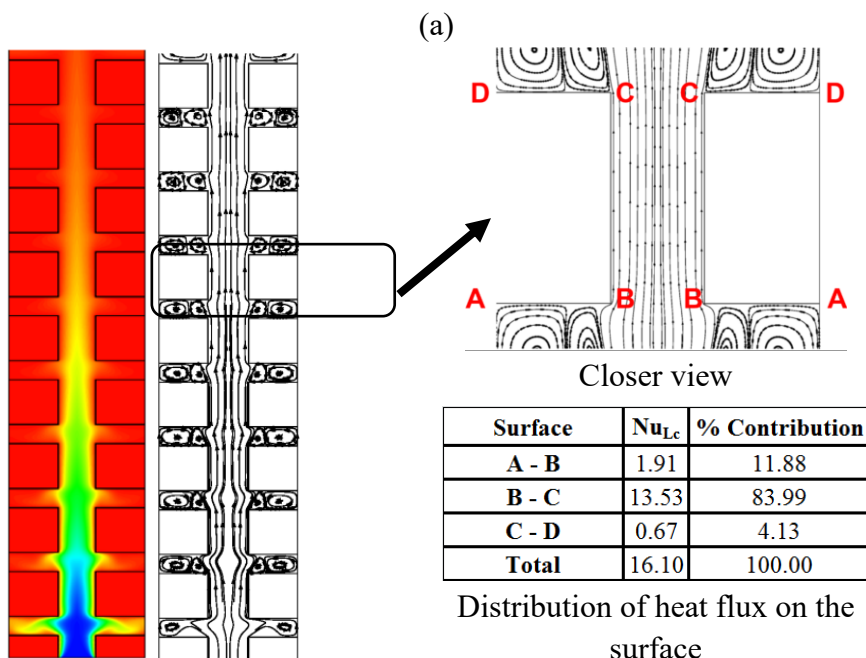
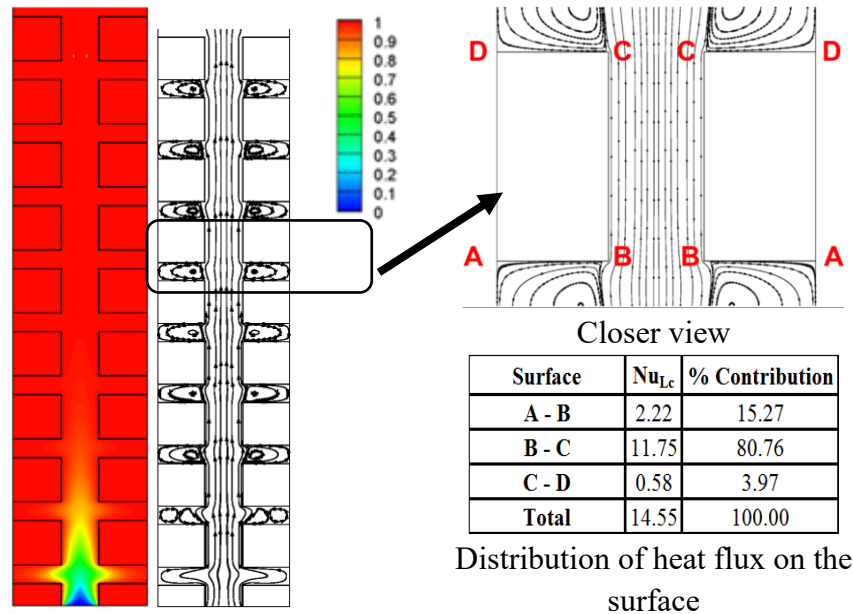
Figure 7.5(a) and 7.5(b) show the streamline and temperature field for the same porosity of Figure 7.4(a) and 7.4(b), when Ri = 10 and Re = 100 and 500, respectively. No significant changes observed in the flow and temperature field if Ri number is increased by 1000 times. The only change of flow configuration is the number of secondary flows for Re = 500 (Figure 7.5(b)) occurring in the space between the rods in vertical direction. However, the top and bottom surface does not have an important effect on the total heat transfer rate from the rod. Figures 7.4 and 7.5 show that for a porous medium with low porosity, the streamline and temperature contours in the most region of porous medium are not changed considerably by change of Re or Ri numbers.

7.1.1.1. Local Interfacial Convective Heat Transfer Coefficient

Figure 7.6 shows the change of local, rod number based interfacial Nusselt number with Reynolds number for different values of porosity and Ri. The change of local interfacial Nusselt number with Re number for Ri = 0.01 and $\varepsilon = 0.96$ shown in Figure 7.6(a). For low value of Ri number (i.e. Ri = 0.01) the buoyancy effect is negligible and forced convection heat transfer is dominant. As it can be seen from the Figure 7.6(a), the value of Nu_L is high for the first block and then it decreases steeply and takes almost a constant value for the rest of blocks showing fully developed condition. For Re = 100, the flow attains to the fully develop condition faster than Re = 500, as it is expected. In general, Figure 7.6(a) shows that when Ri number is small (e.g., Ri = 0.01), the interfacial convective heat transfer coefficient does not change considerably with Reynolds number, particularly for the blocks in fully developed regions.

A slight of increase of Nu_L with increase of Re is observed for fully developed condition. For instance, the rate of increase of Nu_L of tenth rod of porous media with Ri = 0.01 and $\varepsilon = 0.96$ when Re number increases from 100 to 500 is around 20%. By increasing Ri number from 0.01 to 10, the local interfacial Nusselt number increases with Re number as can be seen from Figure 7.6(b). The reverse flows occur in the middle of the channel and this causes the mixing of flow and increase of local

interfacial Nusselt number. By increasing of Re number, the size of the secondary flows at the middle of the channel increases (see Figures 7.3(a) and 7.3(b)) and that is why an obvious difference between the local Nusselt numbers of channels with different Reynolds number is seen which is completely different than Figure 7.6(a). The increase of size and mixing effect of the secondary flows also increase the interfacial heat transfer coefficient.



(b)

Figure 7.5. Streamlines and temperature distribution in porous media with $\varepsilon = 0.51$ and $Ri = 10$, a) $Re = 100$, b) $Re = 500$

By decreasing porosity from 0.96 to 0.51, as given in Figure 7.6(c), there is almost no change in general behavior of interfacial Nusselt number with Reynolds number. When $Ri = 0.01$, the interfacial convective heat transfer coefficient of the rods is very close to each other for different Reynolds number since the increase of Reynolds number in the porous media does not change the behavior of flow (see Figures 7.4-7.5). For the porous media with $\varepsilon = 0.51$ and $Ri = 10$, as it is shown in Figure 7.6(d), the local interfacial Nusselt number increases with Re number for the first two or three blocks, then again, the values of interfacial convective heat transfer coefficient become close to each other. Figure 7.6 clearly shows the effect of porosity on the heat and fluid flow in the mixed convection. The rate of increase of Nu_L for the tenth rod when Re number increases from 100 to 500 for a porous media with $Ri = 10$ and $\varepsilon = 0.96$ is 95% (Figure 7.6(b)), while for a porous media with $\varepsilon = 0.51$ under the same condition, the rate of increase is 11% (Figure (7.6(d))).

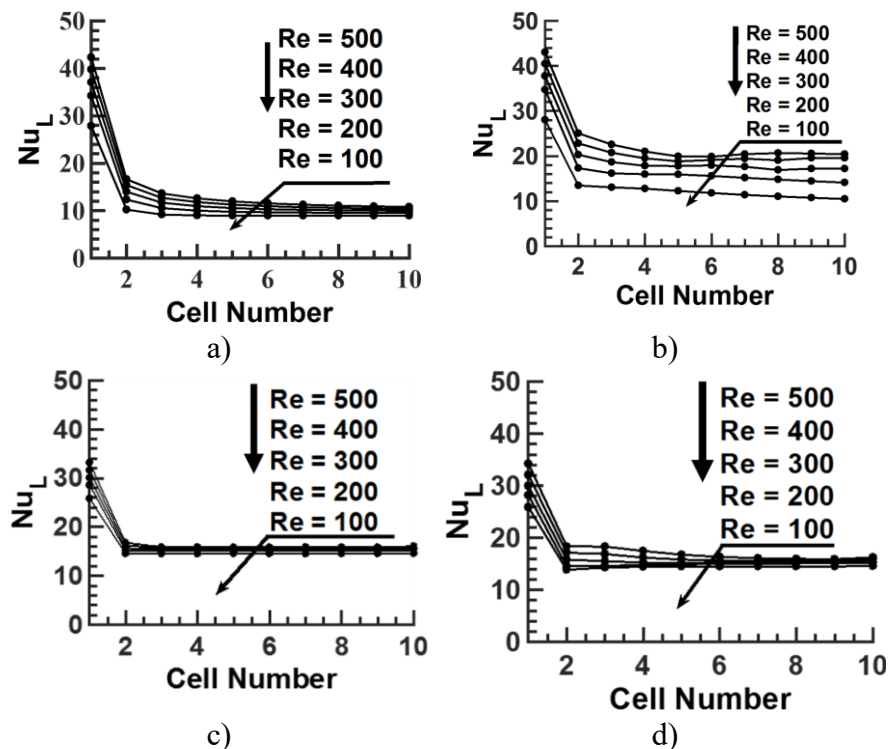


Figure 7.6. The change of local interfacial Nusselt number distribution with porosity, Re and Ri numbers a) $Ri = 0.01$, $\varepsilon = 0.96$, b) $Ri = 10$, $\varepsilon = 0.96$, c) $Ri = 0.01$, $\varepsilon = 0.51$, d) $Ri = 10$, $\varepsilon = 0.51$

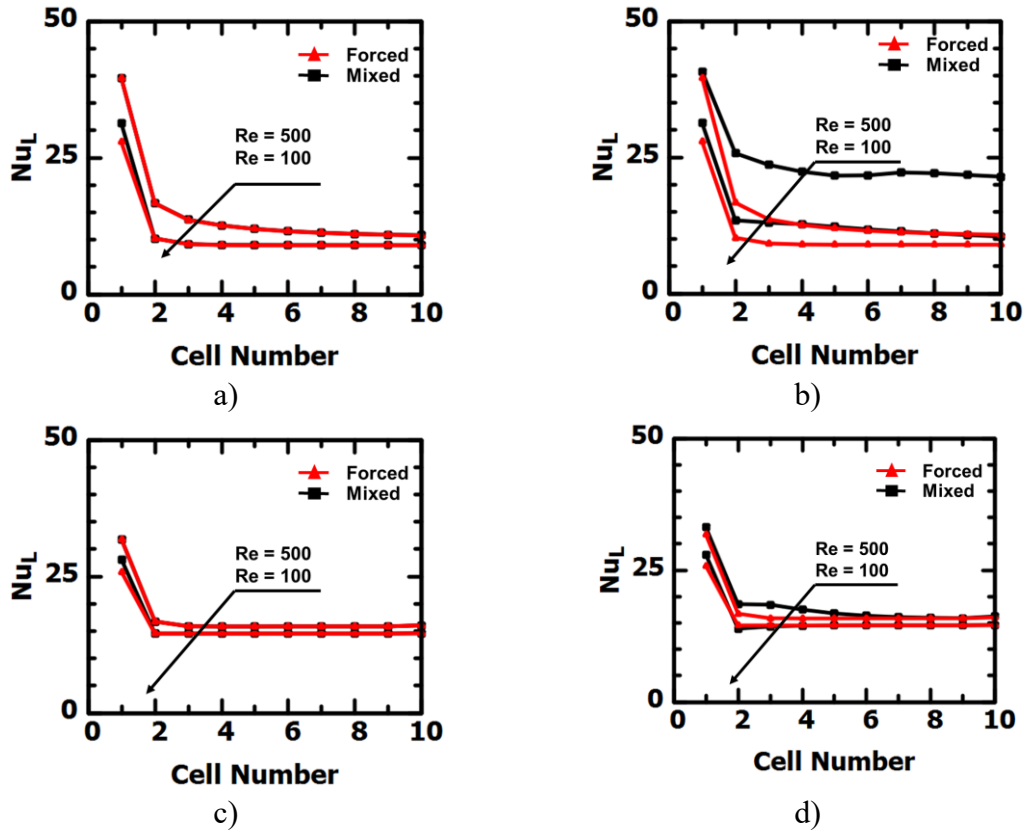


Figure 7.7. The local interfacial Nusselt number between forced and mixed convection for two values of ε , Re and Ri numbers a) Ri = 0.01, $\varepsilon = 0.96$, b) Ri = 10, $\varepsilon = 0.96$, c) Ri = 0.01, $\varepsilon = 0.51$, d) Ri = 10, $\varepsilon = 0.51$

Figure 7.6 compares the distribution of local Nusselt number of the mixed convection with forced convection for two Ri number of 0.01 and 10, two Re numbers of 100 and 500 and finally two porosities of 0.51 and 0.96. As can be seen from this figure, the forced convection interfacial heat transfer coefficient is very close to mixed convection except for the porous media with high porosity (i.e. $\varepsilon = 0.96$) and Ri number (i.e. Ri = 10). For high porosity values, the value of Nu_L deviates from forced convection and Nu_L increases with increase of Ri number. For instance, the values of Nu_L for the last rods of channels increase by 100% if the Ri number increases from 0 (forced convection) to 10.

7.1.1.2. Mean Interfacial Convective Heat Transfer Coefficient

Figure 7.8 shows the change of mean interfacial Nusselt number with Re and Ri numbers for different porosity values. The value of \bar{Nu}_L for forced convection is also

plotted on the same figure as a reference. The change of mean interfacial Nusselt number with porosity for different Ri numbers when $Re = 100$ is shown in Figure 7.8(a). As it can be seen, the interfacial Nusselt number has almost the same value for up to $\mathcal{E} = 0.8$ and it decreases by increase of porosity. Up to specific porosity, then it increases. The rate of increase depends on the Ri number. For small values of Ri number (e.g., $Ri = 0.01$) the rate of increase of interfacial convective heat transfer coefficient is small while for high values of Ri number (e.g. $Ri = 10$) the rate of increase becomes considerable due to the increase of buoyancy effect. For example, by increasing of Ri number from 0.01 to 10 for $Re = 100$, the change of \bar{Nu} for a porous medium with $\mathcal{E} = 0.51$ is 0.61%, while for a porous medium with $\mathcal{E} = 0.96$ under the same condition, the rate of increase become as 29%. Similar comments can be made for $Re = 500$ case as it is given in Figure 7.8(b). However, increase of interfacial convective heat transfer coefficient with Ri number becomes stronger. Particularly, for high porosity values (such as $\mathcal{E} = 0.96$) and high Ri numbers, the increase of size of secondary flows in the middle of channel due to the increase of buoyancy effect causes the considerable increase of heat transfer between solid and fluid. For instance, for a porous media with $\mathcal{E} = 0.96$, increase of \bar{Nu} for $Re = 500$ when Ri changes from 0.01 to 10 is 72%. The trend for enhancement of heat transfer by including buoyancy effect can also be observed from Figure 7.8. The value of Nusselt number of forced convection can considerably increase for porous media when porosity is high ($\mathcal{E} = 0.96$) and Ri increases from 0 to 10.

Figure 7.9 shows the change of \bar{Nu} with Ri and Re numbers for two values porosity as 0.51 and 0.96. The change of \bar{Nu} with Re numbers when $\mathcal{E} = 0.51$ is shown in Figure 7.9(a). As it can be seen in Figure 7.9(a), \bar{Nu} does not change significantly by increase of Ri number even for high values of Re number since there is not sufficient free space for reverse flow when porosity is low. For this reason, the change of Re or Ri number has nearly no effect on heat and fluid flow when porosity is low. By increasing porosity value from 0.51 to 0.96 as shown in Figure 7.9(b), \bar{Nu} increases not only with Ri number but also with Re number as well. For $Re = 100$, the rate of increase is gradual while it becomes steeper for $Re = 500$. As it was explained before, the effect of buoyancy on the interfacial heat transfer coefficient can be observed only for porous media with high values of porosity and Ri number.

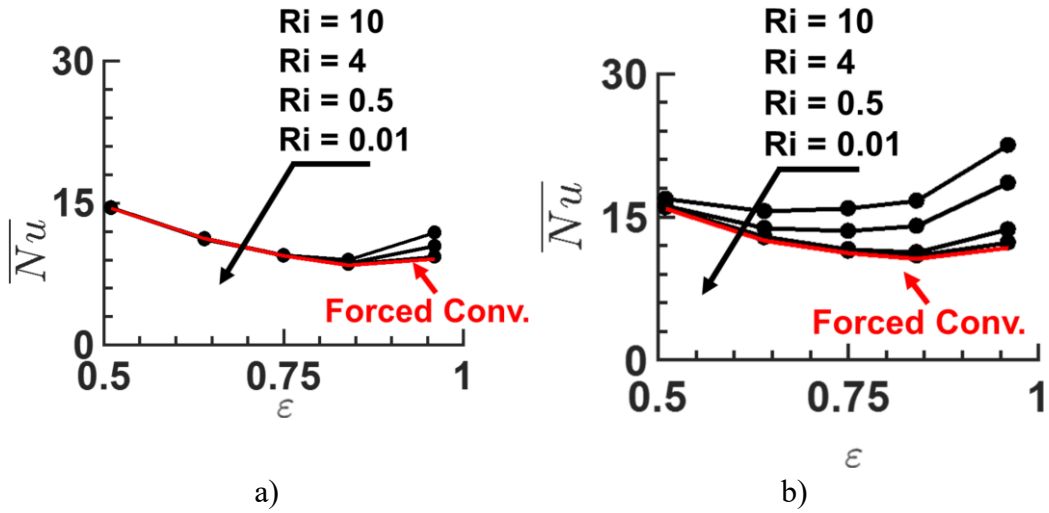


Figure 7.8. The change of mean interfacial Nusselt number distribution with porosity and Ri number a) $Re = 100$, b) $Re = 500$

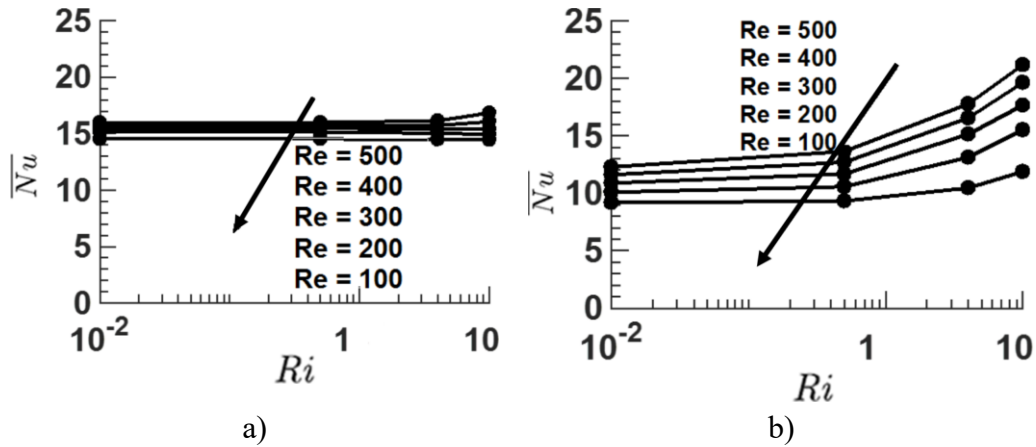


Figure 7.9. The change of mean interfacial Nusselt number distribution with Ri and Re numbers a) $\epsilon = 0.51$, b) $\epsilon = 0.96$

7.1.2. Thermal Dispersion

As it was mentioned before, the governing equations, which are used to obtain thermal dispersion for periodic 2D structure, are continuity, momentum and energy equations. Since the mixed convection is analyzed, the effect of gravity in momentum equation is considered. These equations and boundary conditions are given in Chapter 5.1. The computational domain is explained in Chapter 4. The computational method and the performed grid independency study are described in Chapter 6. The study is performed for Re from 100 to 500, porosity from 0.51 to 0.96 and the obtained results

are given below. The velocity and temperature distribution in the channel for different Ri, Re and porosity is very like what explained in previous chapter. Like previous chapter for low Ri number, forced convection exits and then by increasing Ri number mixed convection becomes dominant and reverse flows occurs. For this reason, in this chapter discussion on temperature and velocity field in the cells for different Re, Ri and porosity are not done.

Figure 7.10 shows the change of the ratio of effective thermal conductivity to thermal conductivity of the fluid with cell number for different Ri, Re and porosity values. Figure 7.10(a) shows the change of k_{eff}/k_f with cell number for different porosities. As shown on Figure 7.10(a) when Ri and Re number is low, (i.e. Ri = 0.1, Re = 100) there is no substantial change in k_{eff}/k_f with cell number for each porosity value. The main reason of this can be explained as highly effective conduction heat transfer compared to the convection. The flow reaches to fully developed condition fast. It is also possible to conclude that k_{eff}/k_f decreases with increase of porosity. Similar behavior can be observed when Ri is increased to 4 from 0.1 as shown in Figure 7.10(b). Even though buoyancy effect is high, Re is low so it is still conduction dominant heat transfer. By increasing Re number to 500 when Ri = 0.1, as shown in Figure 7.10(c), convective heat transfer effects can be seen to develop compared to Figure 7.10(a). It takes longer distance to obtain fully developed flow when Ri = 0.1, Re = 500 compared to Re = 100. By increasing Ri number to 4, buoyancy effects become more visible as k_{eff}/k_f decreases with porosity. And when $\varepsilon=0.96$, strange phenomena is observed where k_{eff}/k_f becomes negative.

As can be seen from Figure 7.11, the 3rd and 8th cells of porous media are considered and the dimensionless velocity, temperature, their deviations and its multiplication are plotted.

As it was mentioned above, one of the interesting points of this study is the negative value of the thermal dispersion for some cases. Many runs were performed to understand the reason of the negative thermal dispersion when the Ri number is high. A wide literature survey on this issue was done. However, this is the first-time negative thermal dispersion and negative effective thermal conductivity is reported in literature. It should be mentioned that all values of thermal dispersion and effective thermal conductivity are expected values but when the Ri number increases the behavior of the thermal dispersion and effective thermal conductivity become unexpected. The velocity

and temperature profile in the voids between the blocks for high values of Ri number ($Ri = 4$) is very different than the low values of Ri number ($Ri = 0.1$). For this reason, Figure 7.12 and 7.13 are provided to explain this unexpected behavior of thermal dispersion for $Ri = 4$.

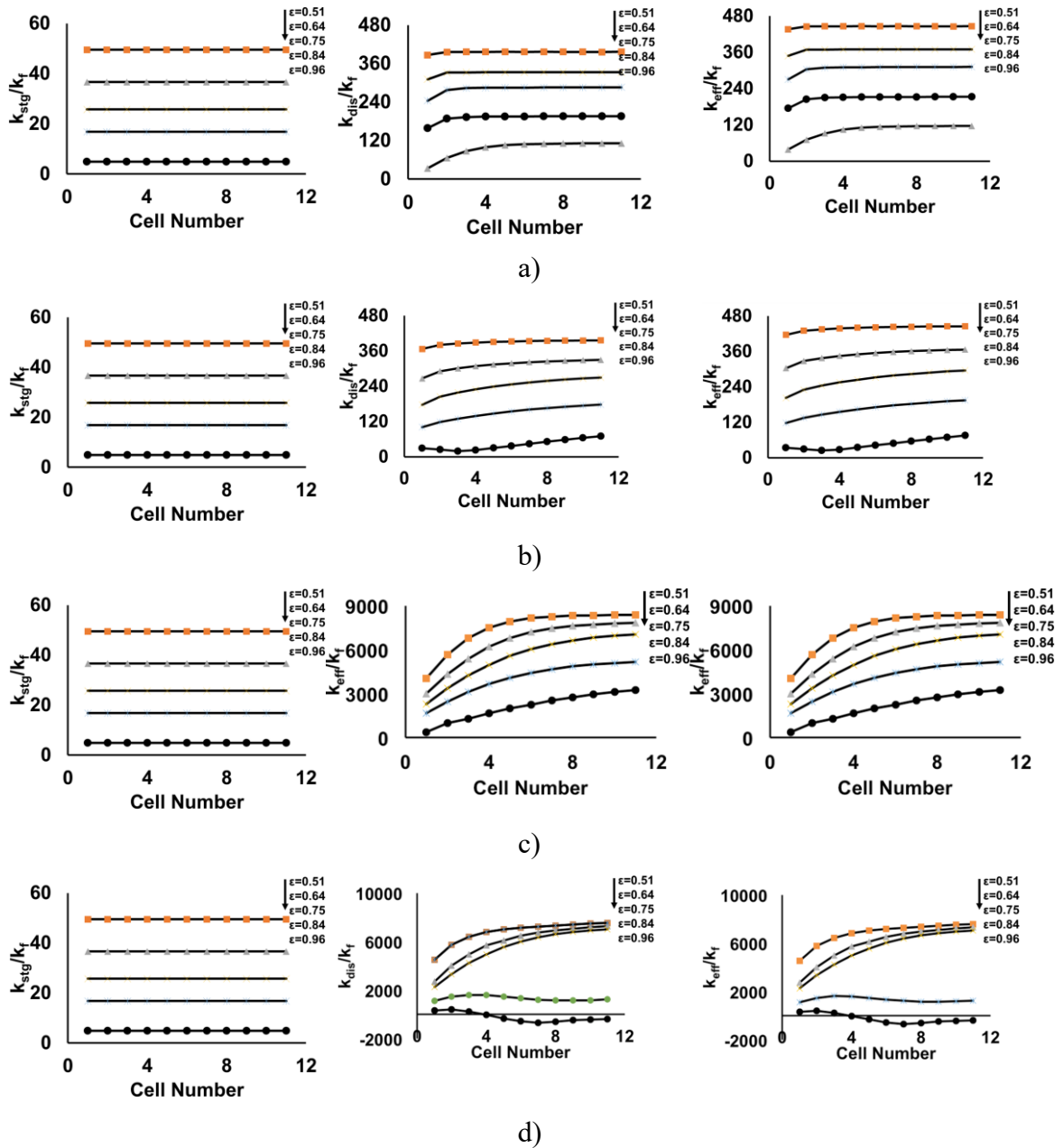


Figure 7.10. The change of the ratio of stagnant, dispersion and effective thermal conductivity to thermal conductivity of the fluid, respectively, with cell number when, a) $Ri = 0.1$, $Re = 100$, b) $Ri = 4$, $Re = 100$, c) $Ri = 0.1$, $Re = 500$, d) $Ri = 4$, $Re = 500$

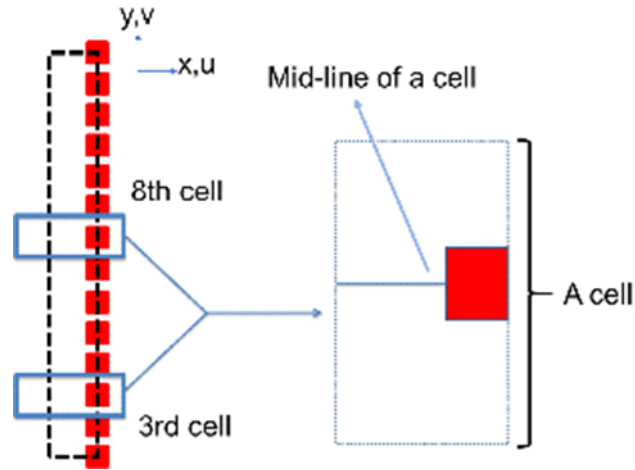


Figure 7.11. The third and 8th rods for the middle of their cells considered for explanation of unexpected behavior of thermal dispersion. Red squares indicate solid rods.

The change of dimensionless velocity, temperature, their deviations and its multiplication of these terms for 3th and 8th cells when $Ri = 0.1$ and $Re = 500$ can be seen in Figure 7.12. Briefly,

- The first column of Figure 7.12 shows the change of dimensionless velocity and fluid temperature in voids between the 3rd rods of block. These dimension values are obtained based on the following definition:

$$v^* = v / v_i, \quad \theta = \frac{T - T_i}{T_s - T_i}; \quad (7.1)$$

- The second column shows deviations of dimensionless temperature and velocity and it is calculated by the following relationship:

$$v' = v - \langle v \rangle; \quad \theta' = \theta - \langle \theta \rangle \quad (7.2)$$

- The third column shows the change of multiplication of the deviations which can be written as:

$$v' \theta' = (v - \langle v \rangle)(\theta - \langle \theta \rangle) \quad (7.3)$$

As can be seen from Figure 7.12, for small values of Ri ($Ri=0.1$) and high values of Re ($Re=500$) both in the third and 8th columns, the value of the velocity is zero at the solid surface and then it increases towards the center of the channel. Due to the symmetry boundary condition, the gradient of velocity is zero at the center of the channel. The dimensionless temperature decreases from the solid surface (which is hotter than fluid) toward the center of channel and then it stays constant in the center of channel due to the symmetry boundary condition. The deviation of the velocity and temperature from the mean value are shown in the second column. Since deviation is defined as difference

between mean value and local values, both negative and positive values must be in the chart. The behavior of the deviation of dimensionless velocity and temperature and their real change are similar to each other. The third column of Figure 7.12 shows the distribution of multiplication of the deviations. Since the behavior of the deviation of dimensionless velocity and temperatures are opposite to each other, their multiplication for entire region is negative. The thermal dispersion which is integral of this multiplication will be negative and based on Eq. (5.20).

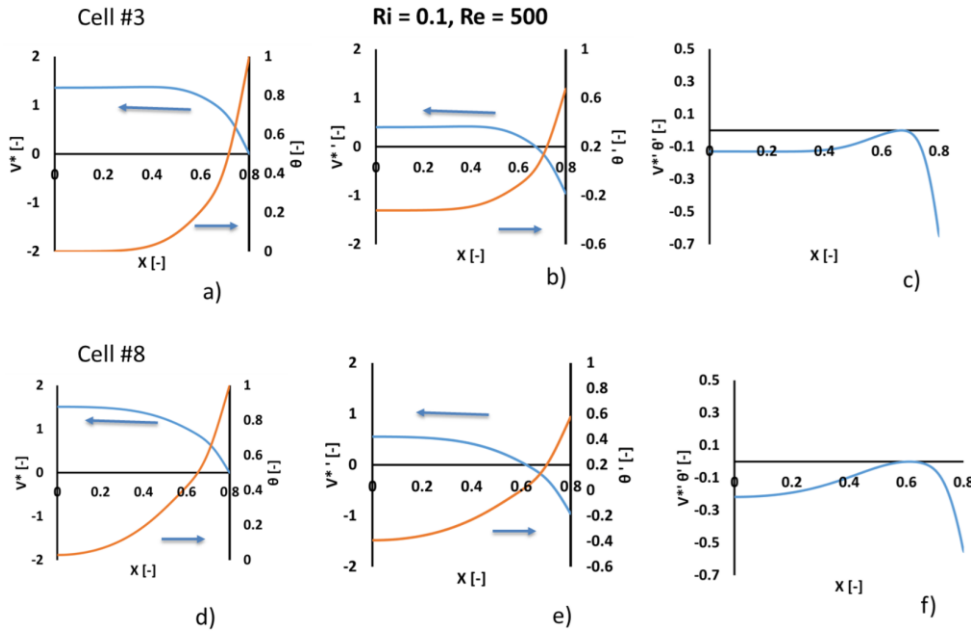


Figure 7.12. The change of dimensionless velocity and temperature, dimensionless deviation and the multiplication of the deviation when $Ri = 0.1$, $Re = 500$ for a, b, c) 3th rod, d, e, f) 8th rod

Similarly, Figure 7.13 shows similar graphs for $Ri = 4$, $Re = 100$. The distribution of velocity and temperature are considerably changed due to the increased buoyancy. The velocity shows an overshoot closer to the hot wall due to the buoyancy and it is an expected profile when the buoyancy forces play an important effect on the flow. The dimensionless velocity is not changed compared to the case with $Ri = 0.1$ and $Re = 100$. Dimensionless temperature decreases from the solid surface to the center of channel and the gradient of dimensionless temperature at the center of channel is zero. The deviation of dimensionless temperature and velocity are plotted in the charts on the second column. The signs (negative or positive), the dimensionless velocity and temperature have opposite behaviors. When the deviation of velocity is positive, the deviation of temperature is negative or vice versa. However, due to strong buoyancy force, the deviations of temperature and velocity are different. The deviation of dimensionless

velocity is negative at the wall and then it increases and becomes positive and finally it decreases toward the center of the channel. Hence, the signs are not symmetrical. For the third cell, almost all values are negative and then their integration becomes negative. Hence the value of thermal dispersion becomes positive base on Eq. (5.20). But for the 8th cell the multiplication of deviation of velocity and temperature is strange. According to the distribution of dimensionless velocity (second column), the multiplication of deviation of the velocity and temperature is negative at the surface and becomes positive and it drops to a negative value and finally its value increases and takes positive values towards the center of the channel. The interesting point is the integration of multiplication of deviations is positive causes that thermal dispersion value becomes negative.

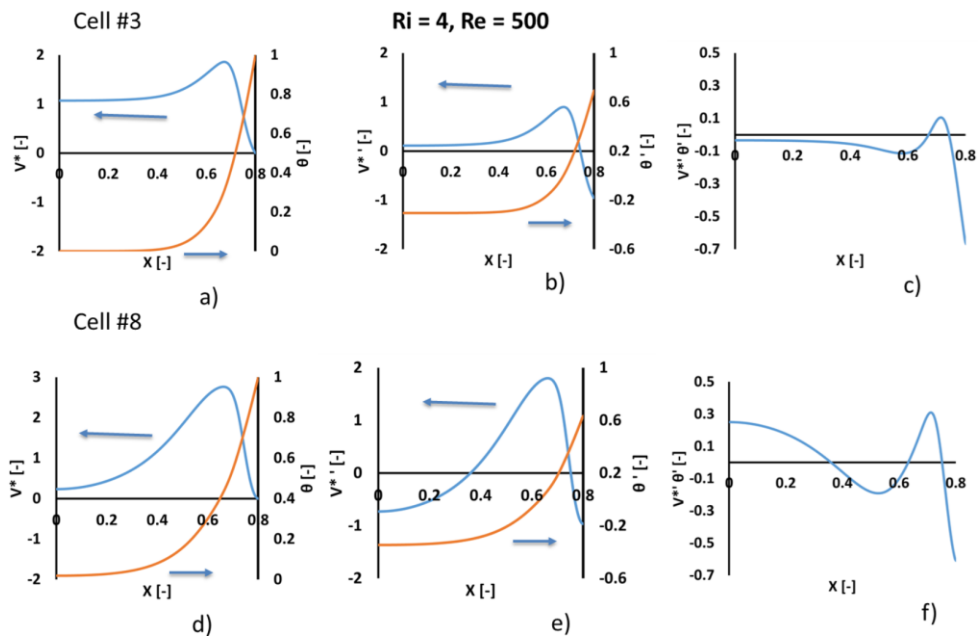


Figure 7.13. The change of dimensionless velocity and temperature, dimensionless deviation and the multiplication of the deviation when $Ri = 4$, $Re = 500$ for a, b, c) 3th rod, d, e, f) 8th rod

During this thesis, many runs were performed to be sure from this negative thermal conductivity. Our observation showed that the above-presented value is correct. However, obtaining negative value for effective thermal conductivity sounds unphysical. Below, our comments relating to this issue are given:

- For low Ri number ($Ri = 0.1$), velocity and temperature profiles are negatively correlated, therefore; the obtained values are positive which are expected value.

- For high values of Ri number ($Ri=4$), the velocity profile completely changes due to strong buoyancy and this causes a positive correlation, which results at the end negative thermal dispersion and consequently effective thermal conductivity. Based on the second law of thermodynamic the value of effective thermal conductivity should be positive and negative thermal conductivity concept is against of the second law of thermodynamics.
- As it is well known, the transport of heat in the fluid phase of the considered porous media is done by two mechanisms as convection and conduction. Most probably, the propagation of heat based on the volume average method in the channel becomes faster than reality and that's why automatically the values of effective thermal dispersion become negative to reduce diffusion propagation.
- One of other reason for negative thermal dispersion is the reverse flows in the channel. Figure 7.14 shows the schematic of flow for two cases of low and high values of Ri number. As can be seen, flow at the low values of Ri number, the direction of the macroscopic (volume averaged) flow and real flow are same. Fluid flows from the bottom of the channel and goes up. However, for high values of Ri number ($Ri = 4$), the inlet of flow from the top of the channel exits however this reverse flow cannot resemble by the column average method. The flowing of reverse flow at lower temperature causes the effective thermal conductivity to become negative since it reduces the propagation of heat in flow direction.
- Our observation shows that there is no problem with volume average technique and it can be applied to porous media under mixed convection, if Ri is small; the results will be acceptable. But the difficulty comes for porous media with high Ri number. The volume average fail for the cases with high Ri number and it may not be used. Unfortunately, many studies macroscopic (volume averaged) on heat transfer in porous media have been published even for high values of Ri number. A range for the effective thermal conductivity ratio is defined and results are presented according the given range. Based on the present study, the results of all performed studies with micro reverse flow might be questionable.

- It should be mentioned that the shortcomings of the problem of mixed convection with high Ri number does not rise from the volume average method. The definition of thermal dispersion based on the temperature gradient causes difficulties. If the equation of 2.26 is rewritten here, it is seen that thermal dispersion based on the gradient temperature and thermal dispersion provides wrong results since a negative flux is obtained.
- Hence, as a result it can be said that volume average can be applied onto heat transfer with mixed convection however for the cases with high Ri number the use of temperature gradient for the effect of thermal dispersion does not work and new innovative methods are required.

7.2. 3D Foam Structure: Forced Convection

7.2.1. Permeability and Inertia Coefficient

Figure 7.15 shows the change of velocity contour at the mid-section slice through the flow direction of the metal foam with 20 PPI. It is plotted for four Re number as 0.001, 12, 26 and 600. The white regions show the solid parts in porous medium. The contour range (i.e., legend) is identical for four Re numbers. The Darcy velocity is 1 mm/s for Re =0.001 which very low. Velocity distribution seems to be very uniform from this figure. By increasing Re number, the velocity in the voids increases and distributions becomes more inhomogeneous especially for Re = 600. The effect of tortuosity (complexity of the fluid path) can be seen clearly since in some pores the highest velocity is deviated very much from the middle of voids. The same situation was observed also for aluminum foam with 10 PPI.

Figure 7.16 shows the change of velocity component in flow direction though the channel of metal foam with 10 and 20 PPI and for Re = 600. As can be seen, a uniform velocity distribution exists in inlet region since the cross-section area does not change. The velocity value increases in the voids of the metal foam due to reducing of flow cross section areas. Finally, the velocity is reduced at the outlet again and begins to become uniform again. Due to slip boundary condition applied to circumference of channel, non-uniformity near the boundaries is always the case.

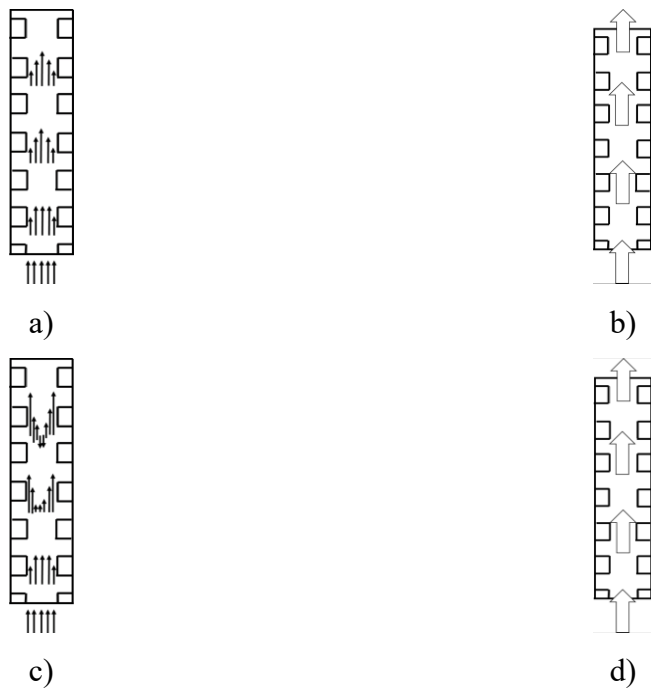


Figure 7.14. The schematic velocity profiles inside a channel when a) $Ri = 0.1$ and pore scale analysis, b) $Ri = 0.1$ and volume-averaged analysis, c) $Ri = 4$ and pore scale analysis, d) $Ri = 4$ and volume-averaged analysis

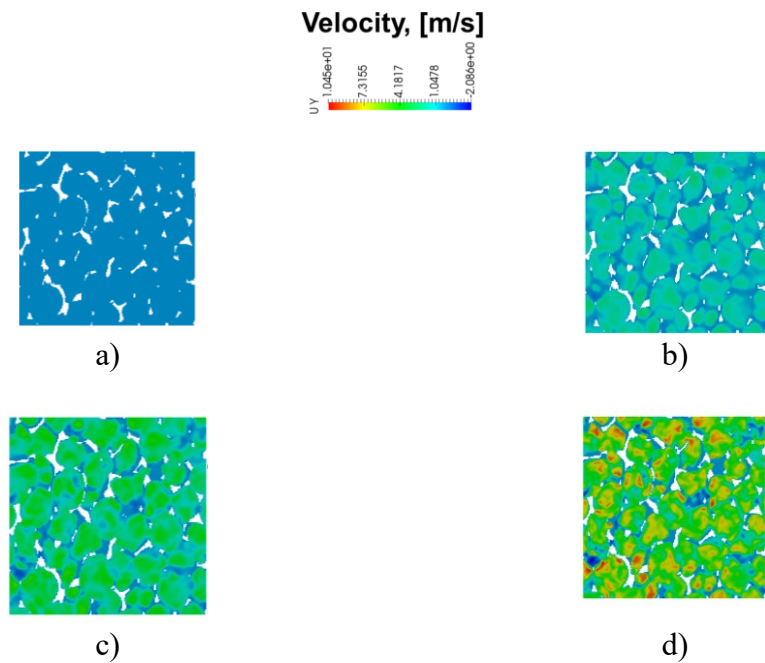
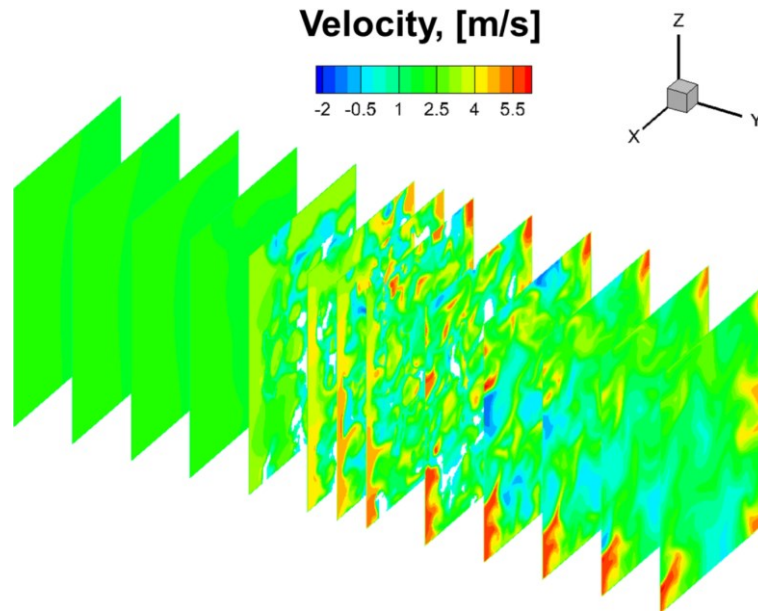
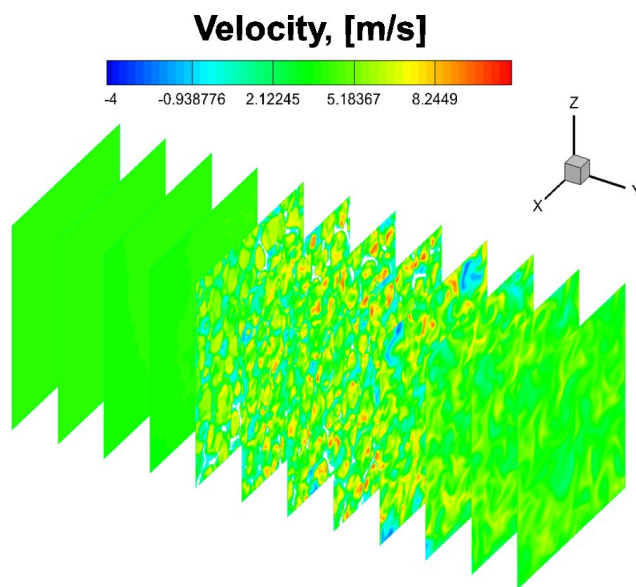


Figure 7.15. The change of velocity contour when the flow is in the perpendicular direction to the page, the mid-section slice of the metal foam with 20 PPI, a) $Re = 0.01$, b) $Re = 12$, c) $Re = 26$, d) $Re = 600$



a)

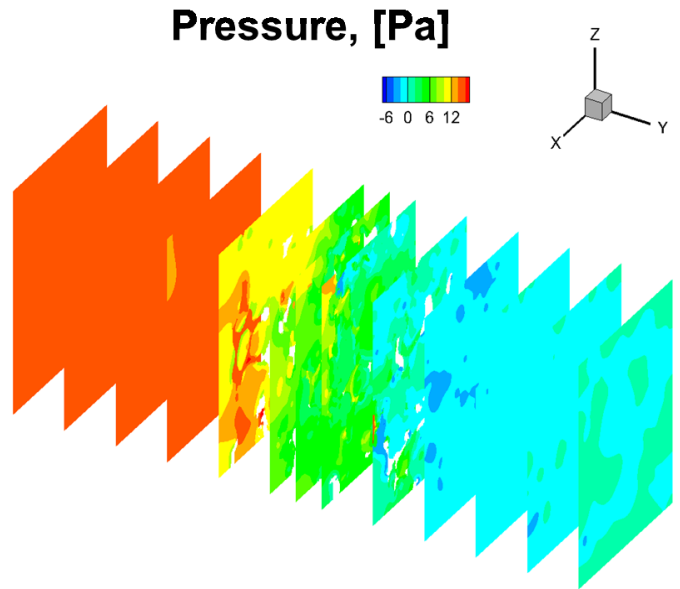


b)

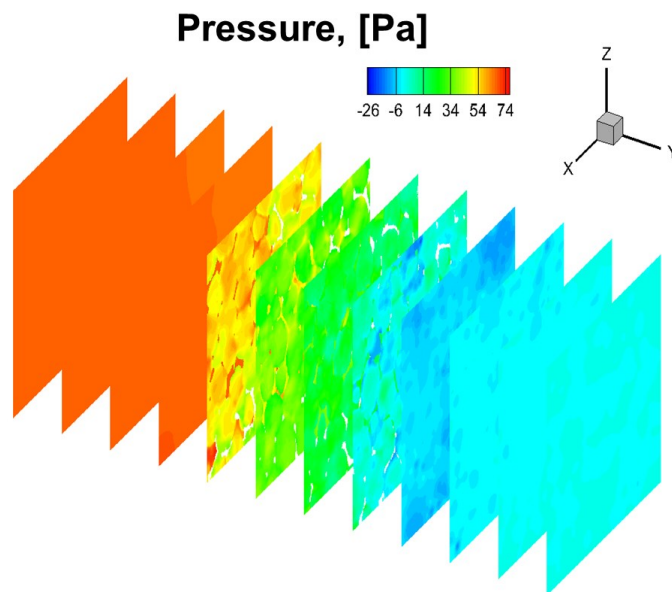
Figure 7.16. The change of v velocity component in flow direction through the channel of metal foam with $Re = 600$ for a) 10 PPI, b) 20 PPI

Figure 7.17 shows the distribution of pressure for the same case. As expected at the inlet of the channel, the pressure is high. Through the domain, it decreases. By changing of the flow cross-section area in the porous media, the pressure gradient in the voids can be seen. Finally, at the outlet of the channel, almost a uniform lowest pressure gradient can be observed.

The distribution of path lines can be seen in Figure 7.18 when $Re = 600$. As it is seen in Figure 7.18, the fluid flows uniformly in the inlet region, as there is no obstacle to disturb flow pattern. As flow reaches to the foam region, the fluid starts to flow through the randomly distributed pores, which brings the irregular nature to distribution.



a)



b)

Figure 7.17. The change of pressure through the channel of metal foam with $Re = 600$ for a) 10 PPI, b) 20 PPI

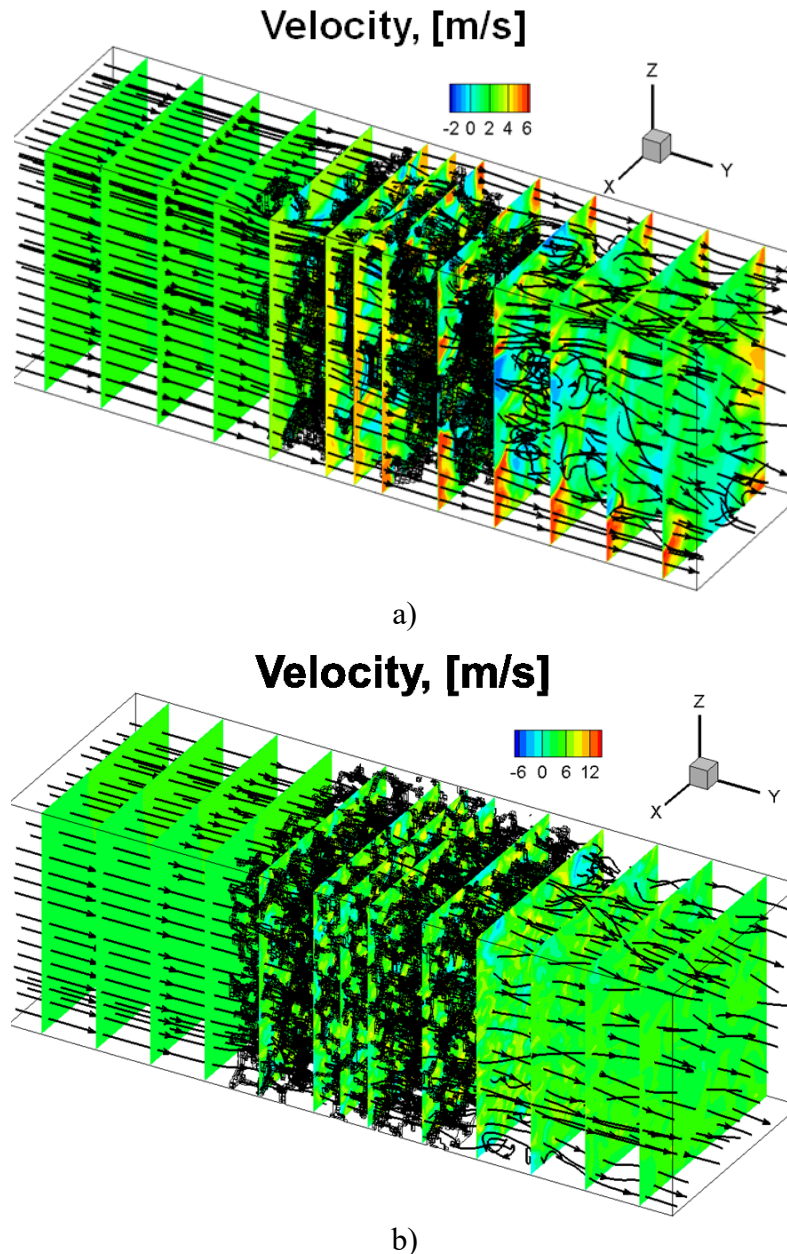


Figure 7.18. Pathlines inside the computational domain when $Re = 600$; a) 10 PPI, b) 20 PPI

The changes of dimensionless pressure drop with Re numbers for aluminum foams with pore density of 10 and 20 PPI and for x , y and z principal axes are presented in Figure 7.19. As it is seen here, the inertia effect is not significant for low Re numbers. As Re number is increased, the effect of inertia appears and Π changes linearly with Re , consequently the inertia effect should be considered. It should also be mentioned that the values of Π for x , y and z directions are not the same and minor changes between them exist. There might be two reasons for this small difference of permeability and inertia coefficient in the principle axes. There might be small anisotropy in the sample,

since its size is small. The second reason might be the elimination of images in x direction slightly causes a difference between the structure of y direction from x and z directions. The elimination of images in y direction is done since the available computer resources in our laboratory cannot process all images.

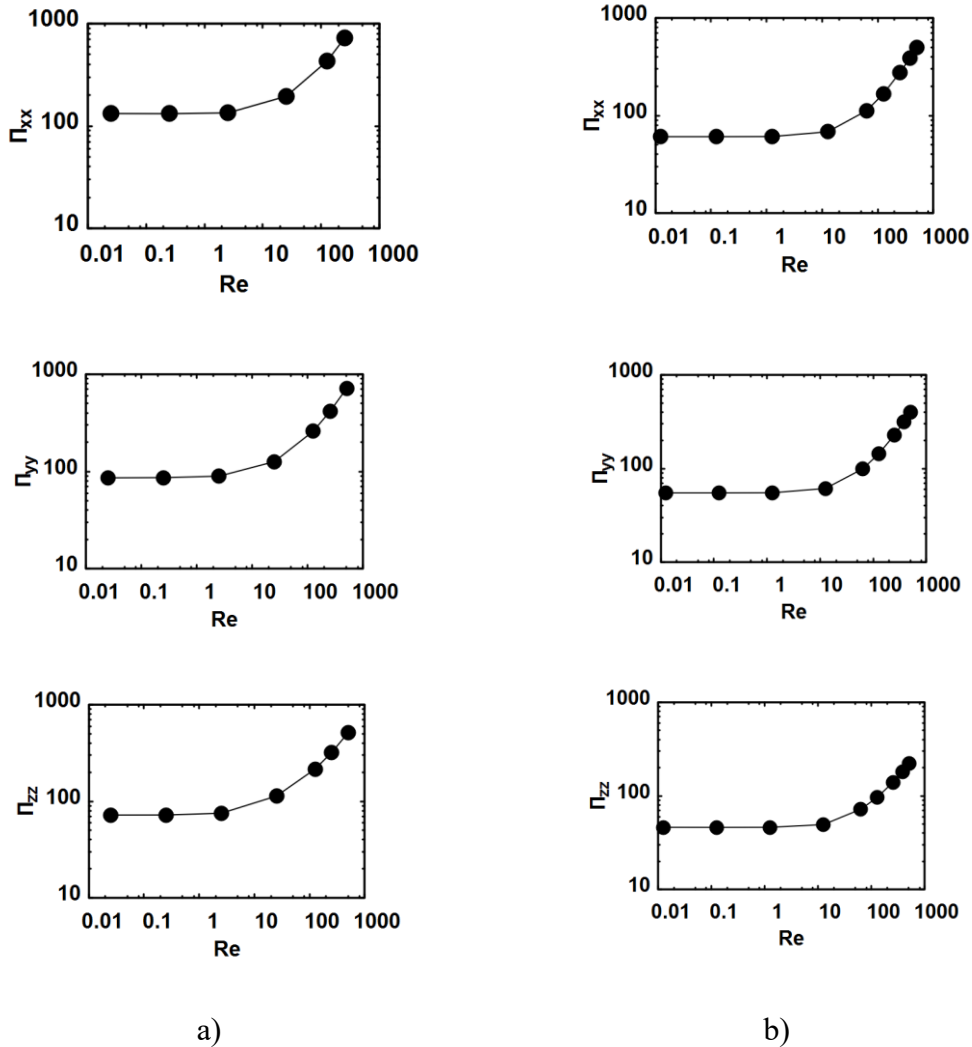


Figure 7.19. The change of dimensionless pressure gradient in x, y and z directions with respect to Re number for a) 10 PPI, b) 20 PPI

The obtained permeability and inertia coefficient for principal axes of all sample foams shown in Table 7.1. The change between the values of these transport properties is not too much and then the average of them can be accepted as unique permeability and inertia coefficient. Figure 7.20 compares the obtained value with some of the reported results. As can be seen for the many aluminum foams with different porosity and inertia coefficient, but with the same PPI may exist. The obtained values for both for permeability and inertia coefficient are in the range of the reported values by the other researchers.

Table 7.1. The properties obtained from 3D model generated in computer environment and the obtained results

Sample No #	1	2	3	4
Pore Density	10	20	20	40
Material	Aluminum	Aluminum	Alumina	Alumina
Porosity	0.90	0.95	0.84	0.84
Cell Diameter [m]	0.0044	0.0023	0.0021	0.0011
Strut Diameter [m]	0.00028	0.00019	0.00027	0.00027
Surface Area [m ²]	0.001500	0.002770	0.003764	0.006731
K _{xx} [m ²]	1.60E-07	8.97E-08	1.19E-07	4.55E-09
K _{yy} [m ²]	2.33E-07	9.66E-08	1.06E-07	4.21E-09
K _{zz} [m ²]	2.56E-07	1.11E-07	1.16E-07	4.34E-09
C _{xx} [-]	0.2054	0.1125	0.234	0.7123
C _{yy} [-]	0.1303	0.0925	0.2302	0.6909
C _{zz} [-]	0.0975	0.1253	0.241	0.762

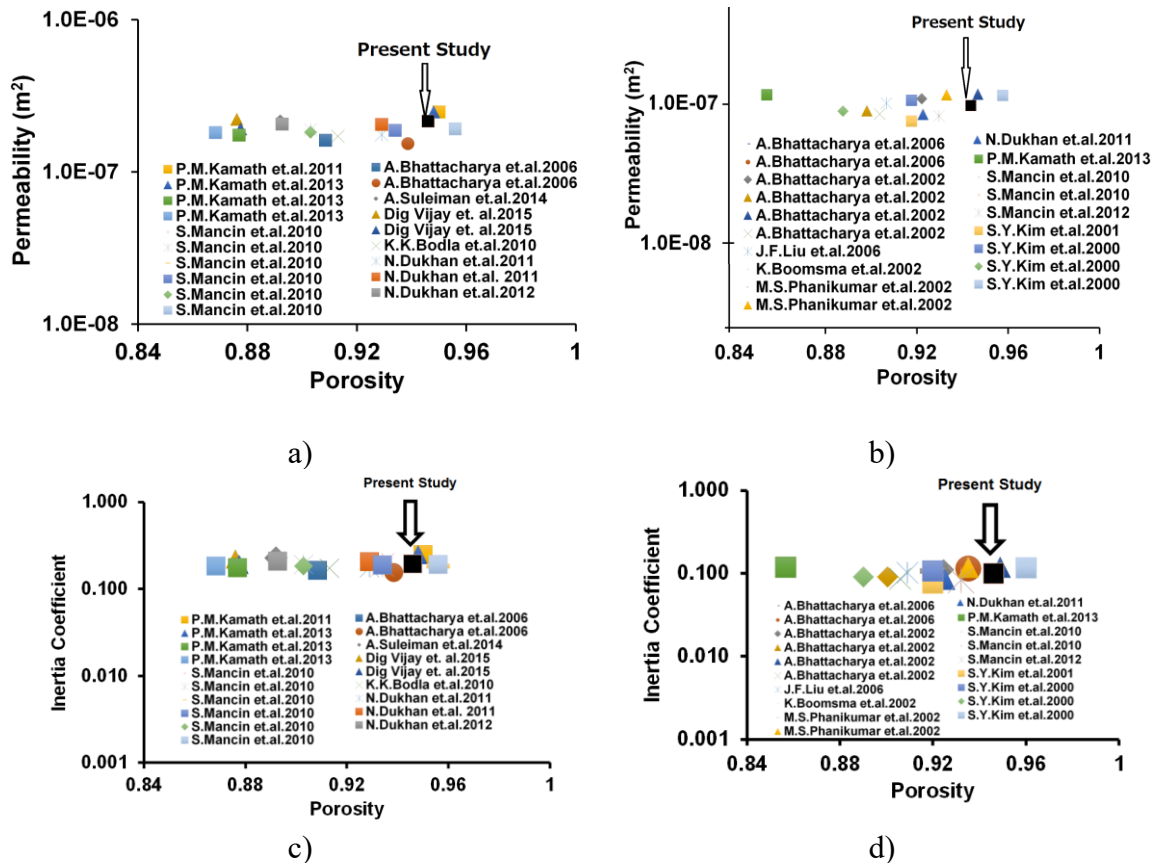


Figure 7.20. Comparison of the present study with the reported studies in literature, a) permeability 10 PPI, b) permeability 20 PPI, c) inertia coefficient 10 PPI, d) inertia coefficient 20 PPI

7.2.2. Interfacial Convective Heat Transfer Coefficient

As it was mentioned before, to determine interfacial heat transfer coefficient, sub-volumes are generated in the flow direction and after solving pore scale governing equations and obtaining the temperature field, Eq. (2.48) is applied to the temperature field of sub-volumes and interfacial heat transfer coefficient and consequently interfacial Nusselt number for each sub-volume is calculated. As it was mentioned before, since the thermal conductivity ratio between solid and fluid (k_s / k_f) is very high, a uniform temperature inside the solid is assumed.

Figure 7.21 shows the temperature distribution of aluminum metal foams with 10 and 20 PPI pore density when $Re = 600$. The general behavior of the heat flow from inlet to outlet is similar for all samples. As seen on Figure 7.21(a), for 10 PPI aluminum foam, the temperature at the inlet region is cold and remains at inlet temperature till the porous media region. The fluid enters to the foam region and due to hot metal foam in this region, fluid temperature starts to increase. After foam region, fluid flows through the end of the channel and temperature in this region is almost constant as there is no solid structure at the outlet region. Figure 7.21(b) shows the similar temperature distribution for 20 PPI foam. Temperature of the fluid increases more for 20 PPI foam compared to 10 PPI foam, as tortuous path of the metal foam increases by increase of PPI and the heat transfer coefficient increase and this also increases heat transfer.

Figure 7.22 shows the temperature profile in the middle line of a cross section for two Re numbers as 120 and 600. Figure 7.22(a) shows temperature profiles for $Re = 120$. As can be seen, the temperature of the fluid in the pores is close to the temperature of the solid as the convective effect is low. By increasing of Re number from 120 to 600, the temperature of the fluid in the pores decreases due to increase of convection. This figure also shows the employed number of mesh is adequate to catch the temperature profile in the pores. The gradient of temperature profiles particularly near the solid surface is important since the total heat transfer from solid to fluid is calculated by using this temperature gradient in entire solid surface.

Figure 7.23 shows two view of temperature distributions of obtained results for the calculation of Nu_v . Figure 7.23(a) shows the cross-section considered for Figures 7.23(b) and 7.23(c). A cross-section along the flow at the middle of aluminum foam where a temperature gradient exists is considered. The fluid temperature gradient for

two cases when $Re = 120$ and 600 are shown in Figures 7.23(b) and (c). The white spaces show solid which is hot. The temperature around the white spaces (hot solid) is greater than its surrounding. The effect of convection can also be clearly observed from the shape of isotherms. It should be noted that there should be sufficient fluid temperature gradient for calculation of Nu_v , otherwise numerical errors might be involved. The gradient of temperature in flow direction can be observed clearly.

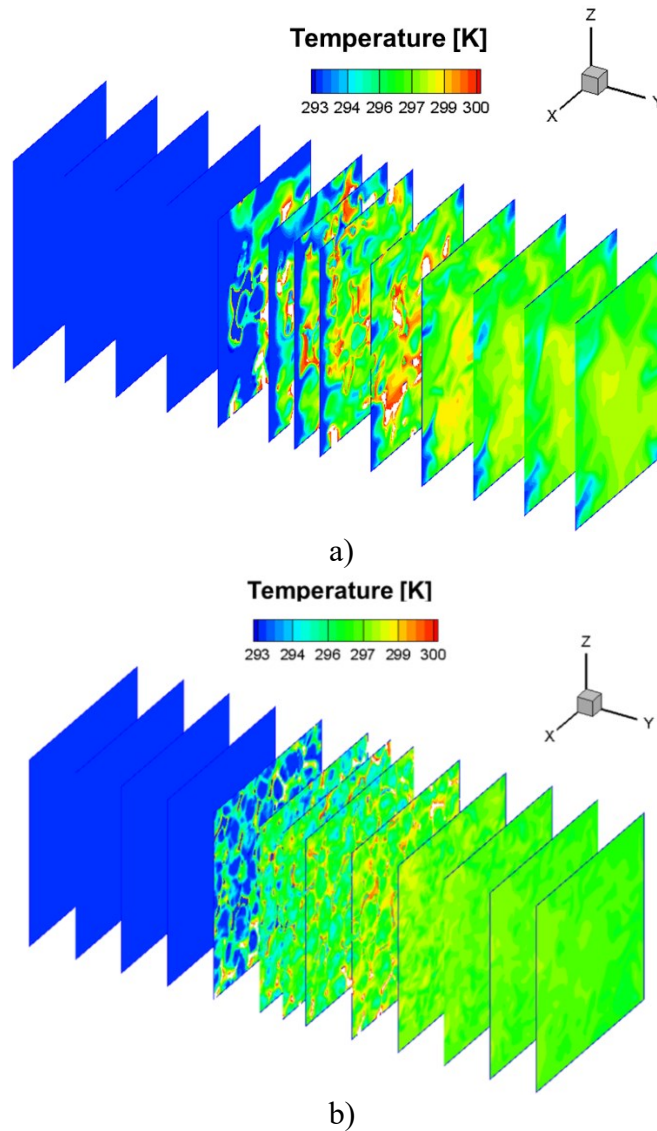


Figure 7.21. The change of temperature in flow direction through the channel of metal foam when $Re = 600$ for a) 10 PPI, b) 20 PPI

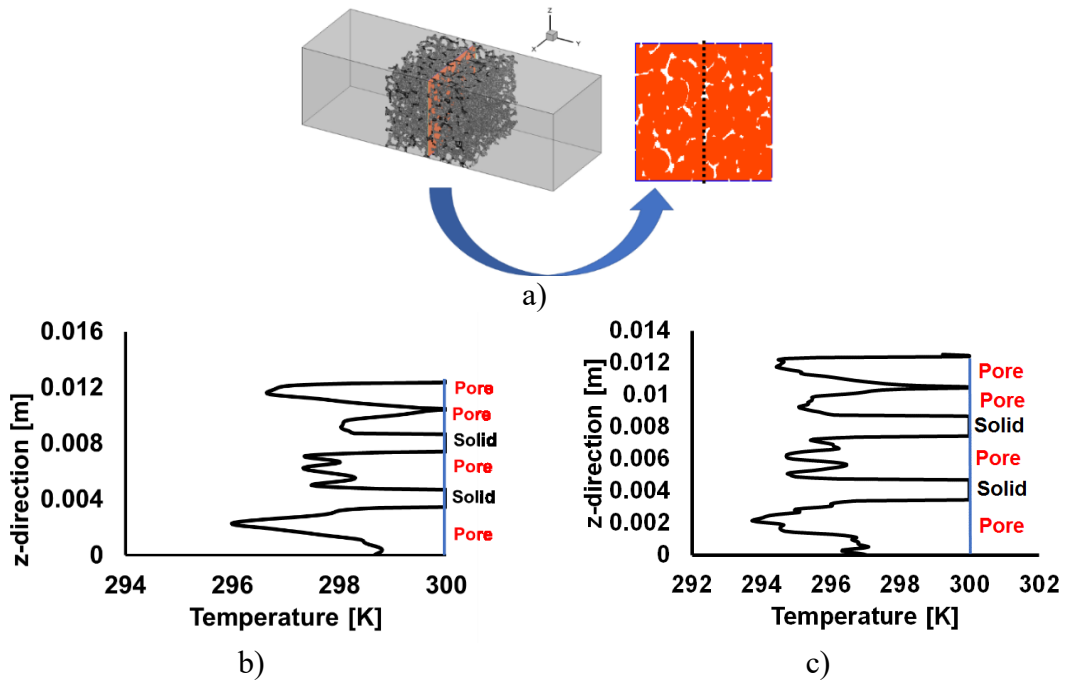


Figure 7.22. The temperature profiles on the line at the mid-point for 20 PPI metal foam; a) the considered line to plot the velocity profile, b) the temperature profile at the mid-plane for $Re = 120$, c) the temperature profile at the mid-plane for $Re = 600$

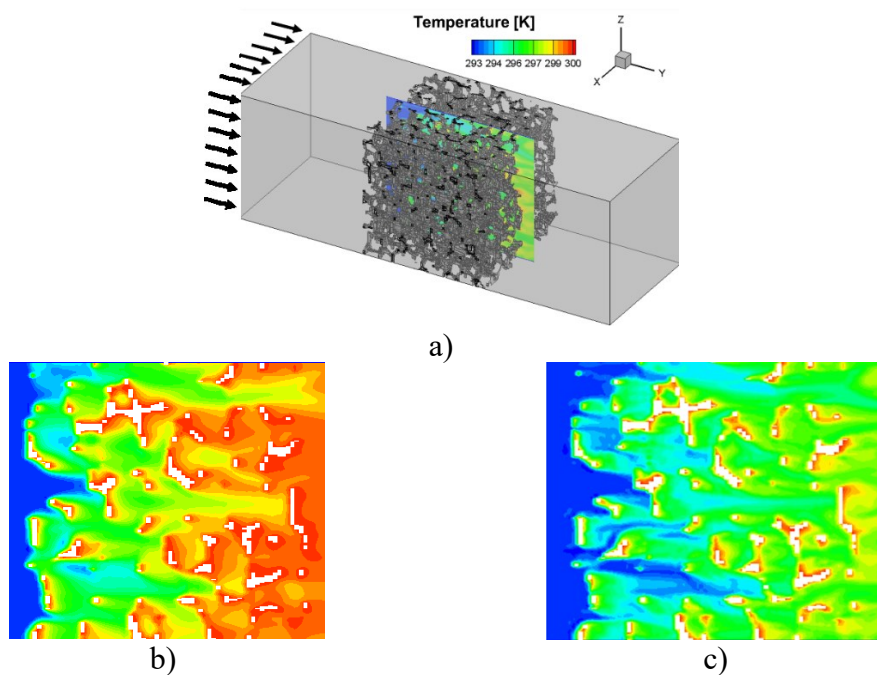


Figure 7.23. A sample of temperature distribution along the flow a) the position of the through the flow direction, b) $Re = 120$ c) $Re = 600$

As it was mentioned before the porous media is divided to the sub-volumes in flow direction (See Figure 5.4(a)) and the interfacial heat transfer coefficient and consequently interfacial Nusselt number for each sub-volume is obtained. But an

important question might be number of the sub-volumes. The porous media should be divided to adequate sub-volumes in the flow direction to calculate correct results. In this study, the porous media is divided to 5 and 20 sub-volumes and the interfacial Nusselt number are obtained for each sub-volumes and presented in Figure 7.24, as a sample for the aluminum foam with 20 PPI metal foam. As it is seen on Figure 7.24, for 20 sub-volumes the local interfacial Nusselt number are fluctuating while the results are nearly constant for 5 sub-volumes. The high fluctuation of results for 20 sub-volumes might be due to rapid change in the structure of the foam from solid to fluid or vice versa. However, the averages of two sub-volumes are the same. By following volume-average concept, taking one cell as a control volume is more realistic and logical. For this reason, in this study results are obtained based on the cell size.

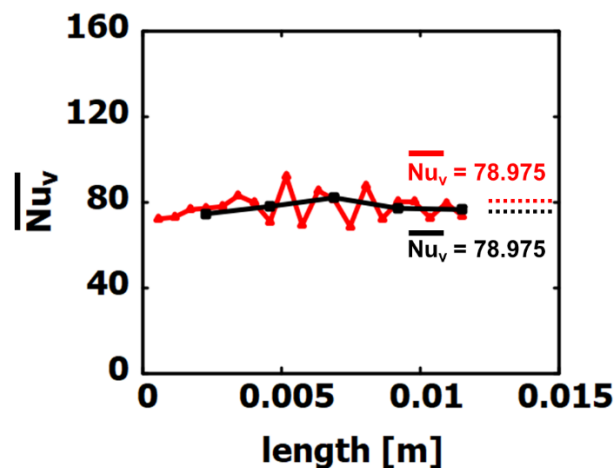


Figure 7.24. The change of interfacial Nu number with number of volume in flow direction (The dotted lines shows average values)

The obtained results for the interfacial Nusselt number are validated with the study of Calmidi and Mahajan (2000). They studied aluminum metal foam and obtained the interfacial convective heat transfer coefficient and Nusselt number experimentally. They considered wide range of different aluminum foams in their study. The results of their experimental studies were evaluated by Zhang et al. (2015) and a correlation is suggested (see Eq. (3.19)). In Figure 7.25, the change of Nu number with pore scale Re number is plotted. The red line shows the values obtained from the correlation of Calmidi and Mahajan (2000), while blue lines indicate 50% upper and lower values of their correlation. Black squares show the values of the present study. The validation is done for 20 PPI aluminum foams. Their results and the present study are in acceptable

agreement. The maximum difference between two results of Nu_v for 10 PPI is 39% while this value for 20 PPI is 24%. The difference between the results of two studies may occur due to some reasons:

- the structure of the studied aluminum foam in this study might be different than the aluminum foams studied by Calmidi and Mahajan (2000). Nowadays many manufactures produce aluminum foam with different geometry of cells and struts. The differences in strut diameter, surface area and pore to throat may cause the deviation of the computational results from the correlation. For instance, one difference between the structure of aluminum foam studied by Calmidi and Mahajan (2000) with the aluminum foam in the present work is strut diameter. The strut diameter of aluminum foam of Calmidi and Mahajan (2000) are 0.40 and 0.30 mm (the second sample is 0.35 mm) for 10 and 20 PPI while the strut diameters of the presents samples are 0.28 mm and 0.19 mm.

- The truncation errors during computation of the interfacial heat transfer coefficient may cause the difference between computational and experimental results. Due to high tortuous path of the structure, the volume averaged fluid temperature considerably increases and becomes nearly the same with volume-averaged solid temperature, particularly at the low Re numbers (such as $Re = 100$). This results in very small temperature difference between fluid and solid phases that triggers the truncation error during calculation of interfacial heat transfer equation. For instance, the values of $\langle T \rangle^f$ and $\langle T \rangle^s$ when $Re = 120$ are 300.000 and 299.053 K whose difference is small. Most probably, the same errors occurred in the experimental studies of the Calmidi and Mahajan (2000) due to low Re number.

- As mentioned previously, the study of Calmidi and Mahajan (2000) is experimental study and it also may contain experimental errors due to the accuracies of the equipment used in their study. The estimation of the experimental error of their study was reported by Calmidi and Mahajan (2000) as $\pm 4.3\%$ in their study.

The comparison between the variation of Nu_v with pore scale Re number for 10 and 20 PPI aluminum foam shows that Nu_v value for 10 PPI aluminum foam is greater than 20 PPI (see Figure 7.25). However, this does not mean that heat transfer coefficient of the aluminum metal foam with 10 PPI is greater than 20 PPI due to definition of Nu_v number. The interfacial Nusselt number is defined based on square of cell diameter.

Since the cell diameters of the 20 PPI is smaller than 10 PPI, h_v of the 20 PPI may be greater than 10 PPI. Figure 7.26 shows the variation of h_v with Reynolds number for 10 and 20PPI aluminum foams. As can be seen, the value of h_v of 20 PPI is higher than 10 PPI.

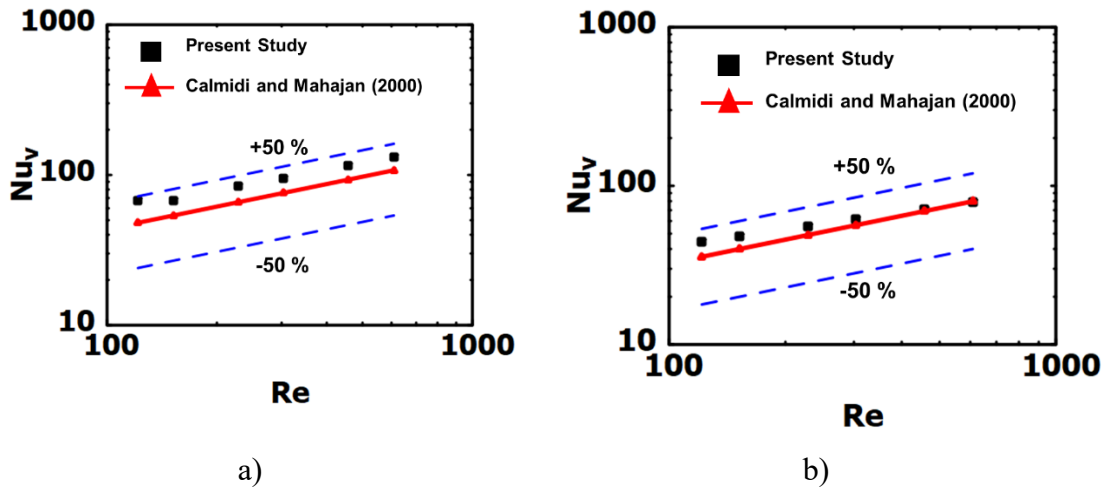


Figure 7.25. The comparison of interfacial Nu number for the present study with the study of Calmidi and Mahajan (2000) for different Re numbers for a) 10 PPI aluminum metal foam, b) 20 PPI aluminum metal foam

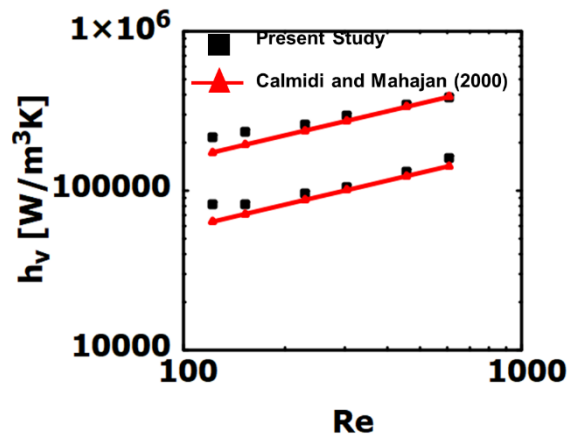


Figure 7.26. The change of the interfacial heat transfer coefficient of 10 and 20 PPI aluminum foams with pore scale Re number

The change of interfacial Nusselt number and convective heat transfer coefficient with Re number for all samples considered in this study is shown in Figure 7.27. As seen, due to high value of k_s/k_f ratio of both ceramic and aluminum foams (700 and 6498, respectively), the change of material with the same PPI does not change interfacial convective heat transfer coefficient and interfacial Nu number significantly, from the comparison of 20 PPI aluminum and ceramic foams. As seen in Figure 7.27(b),

by the trend of changing of h_v with PPI becomes the same for both aluminum and ceramic foams. By reducing the value of PPI, the value of h_v decreases for both aluminum and ceramic foams. As it was mentioned before Nu_v strongly depends on the cell size (selected as characteristic length). Hence, in order to analyze the change of interfacial Nusselt number of different foams with any parameter, in addition to the change of Nu_v , the variation of h_v should also be plotted. Three important results can be concluded from Figure 7. 28(b):

- the highest value of h_v belongs to ceramic foam with 40 PPI.
- the value of h_v increases with decrease of cell size since number of cells in the foams increases. The high number of cells increases mixing effect.
- The value of h_v is identical for both ceramic and aluminum forma of 20 PPI since the cell size are almost equal.

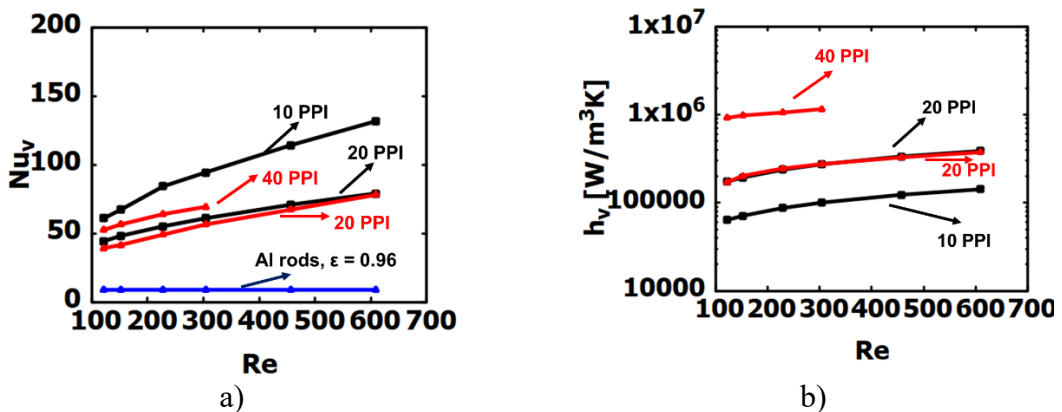


Figure 7.27. For all the samples considered in this study for different Re numbers a) the change of interfacial convective heat transfer coefficient, b) the change of interfacial Nusselt number

7.2.3. Thermal Dispersion

Similar with interfacial convective heat transfer calculations, the foam region is divided into sub-volumes and calculation was performed for sub-volumes. After obtaining the velocity and temperature fields, Eq. (5.27) and (5.29) are used to obtain longitudinal and transverse thermal dispersion of each sub-volume, respectively. The average of thermal dispersion for the sub-volumes yields the thermal dispersion values for the studied foam.

Thermal dispersion both in longitudinal and transverse directions is evaluated in this study. If the heat and fluid flow through the same direction, longitudinal thermal dispersion occurs (see Figure 7.28(a)). However, if fluid and heat flow perpendicular to each other, transverse thermal dispersion can be observed, as shown in Figure 7.28(b). The results for both longitudinal and transverse directions are reported below.

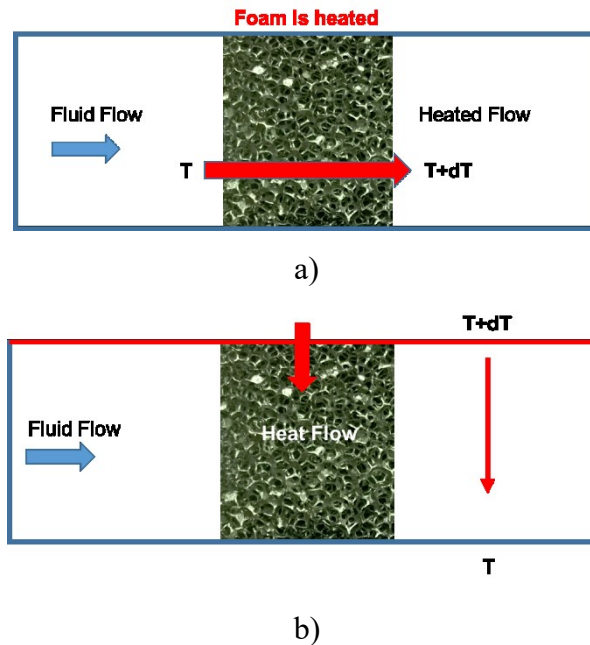


Figure 7.28. Directions of heat and fluid flow in a porous media a) longitudinal direction , b) transverse direction

7.2.3.1. Longitudinal Thermal Dispersion

The results of present study are compared with the reported studies in the literature for longitudinal thermal dispersion of aluminum foams. The comparison of longitudinal thermal dispersion of aluminum metal foam with the change of Re number for pore density 10 and 20 PPI is presented in Figure 7.29. Unfortunately, no experimental or even numerical results relating to thermal dispersion of metal foam could be found in literature. To the best of our knowledge, the only reported study relating to thermal dispersion of metal foam is the theoretical study performed by Zhang and Nakayama et al. (2015). This correlation is given by Eq. (3.20) in Chapter 3. Figure 7.29 shows the comparison and as can be seen, an acceptable agreement between the results of present study and the suggested correlation for both 10 and 20 PPI exists. The agreement of the present study with the study of Calmidi and Mahajan (2000) in terms of interfacial Nusselt number are better than longitudinal thermal dispersion compared with the correlation of Zhang and Nakayama (2015).

The main reason of larger difference between the result of present study and the suggested correlation might be the assumptions employed for derivation of the correlation. Although their correlation is based on the interfacial heat transfer correlation suggested by Calmidi and Mahajan (2000), the employed approach is conduit model. In this model, mechanical mixing of fluid due to collision of fluid particles with strut and changing of flow path from one cell to another cell are not taken into account. The aluminum foam is accepted as consisting of large number of straight conduits in which a fully developed flow without changes in flow direction exists. Based on this assumption, heat diffusion from wall to the center is the main reason of mixing heat. Unfortunately, the results of the suggested correlation for metal foam was not validated with experimental studies since no experimental study exists. Based on the above explanations about the employed assumption, 50% difference for thermal dispersion can be tolerated.

By adding stagnant thermal conductivity to thermal dispersion value, the effective thermal conductivity can be found. As can be seen both in Figure 7.29(c) and (d), the material and tortuosity of metal foams can increase the effective thermal conductivity significantly. The values of $k_{eff,xx} / k_f$ for 10 and 20 PPI when $Re = 600$ are 635 and 338 which means 635 % and 338% percent of increment compared to the clear fluid.

After completing comparison discussion on longitudinal thermal dispersion on metal foam, the discussion on the longitudinal thermal dispersion is started. The results for longitudinal thermal dispersion and effective thermal conductivity for 20 and 40 PPI are shown in Figure 7.30. It is seen that the studied ceramic metal foams are not very good at increasing thermal conductivity compared to aluminum foam samples. For 20 PPI aluminum foam when the $Re = 600$, the value of $k_{eff,yy} / k_f$ is 732 while for the same PPI number of ceramic foam and the same Re number, this value is 531. The main reason of this difference is the value of stagnant conductivity of aluminum foam. What is more, for 40 PPI ceramic foam sample, highest Re number results cannot be obtained due to failure of CFD solver for those cases. The reason behind that is related with the number of grid. In this study, the highest number of the grid, which the current computing sources available for this study allow, are used. However, when Re number is high, current mesh are not capable of determining flow and temperature field inside

the pores, especially in the boundary layer near the solid structure and the solver diverges.

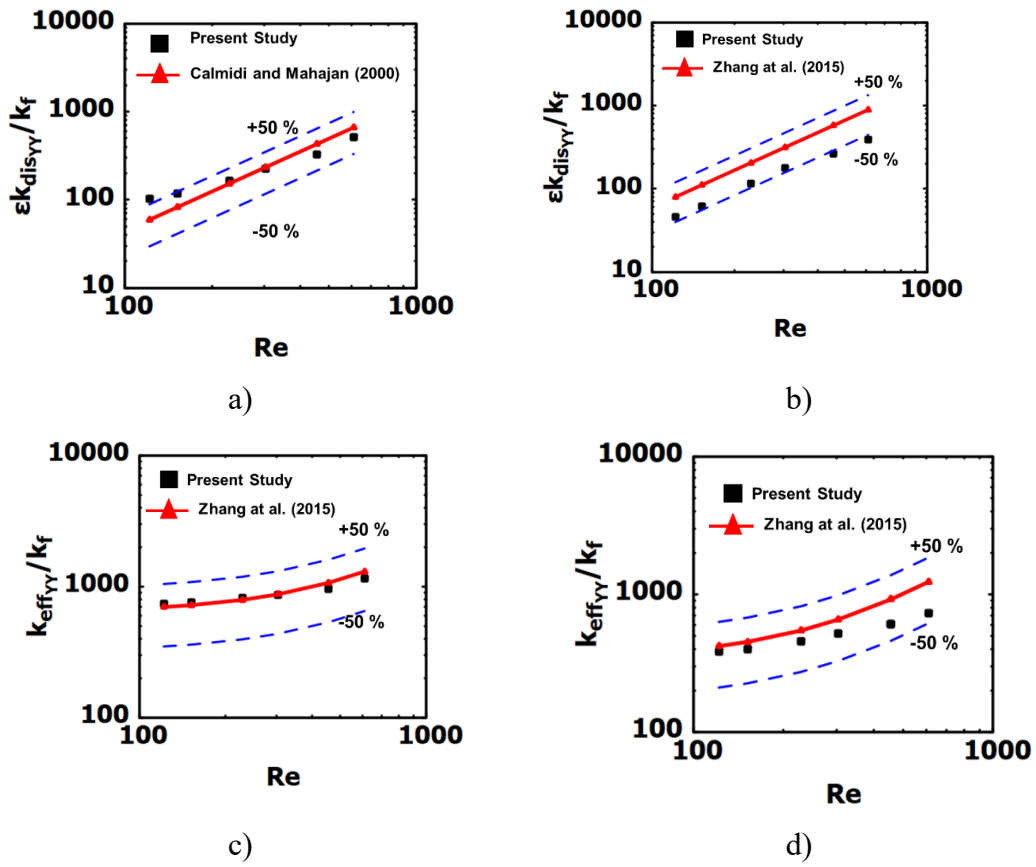


Figure 7.29. The comparison of present study with the study of Zhang et al. (2015) for different Re numbers for a) k_{dis}/k_f of 10 PPI aluminum metal, b) k_{dis}/k_f of 20 PPI aluminum metal, c) k_{eff}/k_f of 10 PPI aluminum metal foam, d) k_{eff}/k_f of 20 PPI aluminum metal foam

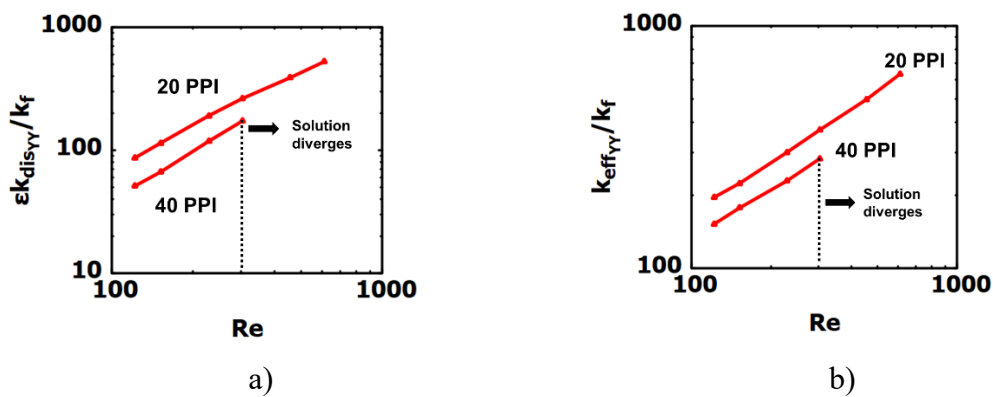


Figure 7.30. The change of a) k_{dis}/k_f , b) k_{eff}/k_f , with Re number for ceramic foam samples

7.2.3.2. Transverse Thermal Dispersion

Similar to the calculation of longitudinal thermal dispersion, the porous media divided into sub-volumes but in transverse to the flow direction. A temperature gradient in transverse direction is generated and the pore scale governing equations are solved for the generated domain. Then the transverse thermal dispersion is obtained by using the obtained velocity and temperature fields and Eq. (5.29). The sub-volumes and temperature gradient in transverse direction are shown in Figures 5.4(b-d) and 5.4(f) of previous chapters. In general, determination of transverse thermal dispersion is a very challenging process. Many numerical runs are completed to build the numerical model and generate a linear temperature gradient in transverse direction.

To the best of our knowledge, unfortunately no correlation or experimental or numerical works for determination of transverse thermal dispersion of aluminum foam and ceramics. The only available correlation is the expression suggested by Zhang and Nakayama (2015) (see Eq. 3.21 in Chapter 3). As it was mentioned before, conduit model has been used to derive the suggested expression. The comparison between the correlation of Zhang and Nakayama and the results of present study is given in Figure 7.31. As expected transverse thermal dispersion is smaller than longitudinal one. A good agreement between the results of two studies can be observed. Maximum difference between two results is 42% for 10 PPI and 22% for 20 PPI aluminum foams. Considering assumption of conduit model, these differences between the results of two studies for transverse thermal dispersion are acceptable. Figures 7.31(c) and (d) show the change of effective thermal conductivity with pore scale Re number. Based on definition of Eq. (2.2) in Chapter 2, the value of k_{stag}/k_f for 10 and 20 PPI aluminum foam is 635.80 and 338.91. If this value compared with the values of $k_{dis,xx}/k_f$ for the studied aluminum foams, in the range of studied Re number, transverse thermal dispersion does not have significant effect on the effective thermal conductivity. That is why $k_{eff,xx}/k_f$ almost does not change with Re number for both 10 and 20 PPI aluminum foams.

The change of transverse thermal dispersion in terms of effective thermal conductivity for alumina ceramic foam with 20 and 40 PPI pore density is shown in Figure 7.32. It is seen that transverse thermal dispersion is low compared to longitudinal thermal dispersion which is given in Figure 7.29. Moreover, transverse thermal

dispersion for alumina foam with 40 PPI pore density is also reported on Figure 7.33, as well. The results are shown up to $Re = 300$ for 40 PPI foam structure due to similar convergence problem explained in the longitudinal thermal dispersion sub-heading. Effective thermal conductivity decreases of ceramic 20 and 40 PPI structures are compared in Figure 7.32 and as seen, increase of pore density from 20 to 40 PPI, transverse thermal dispersion decreases for the samples considered in this study. However, change in Re number does not affect transverse thermal dispersion alike aluminum foam samples.

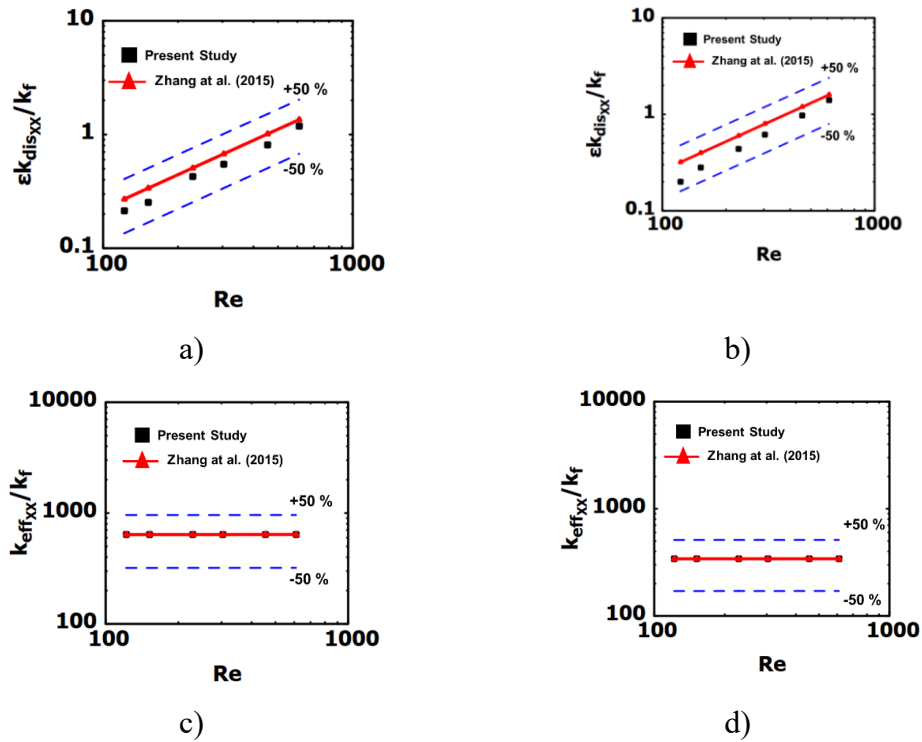


Figure 7.31. Transverse thermal dispersion compared with reported study of Zhang et al. (2015) for 20 PPI aluminum foam, a) k_{dis} / k_f , b) k_{eff} / k_f

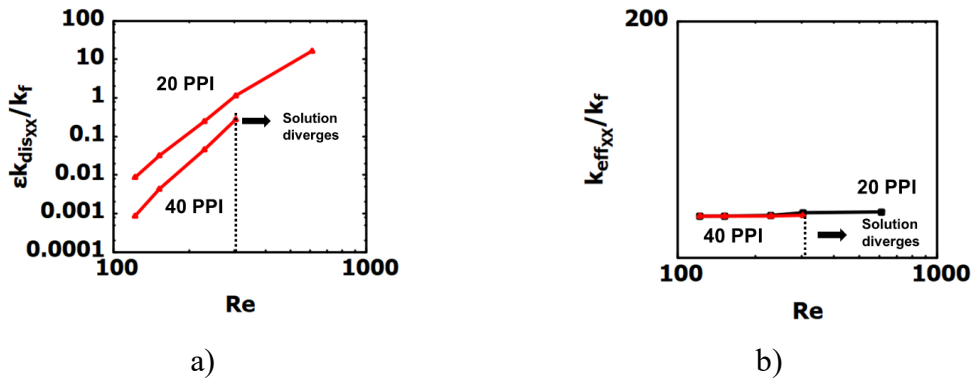


Figure 7.32. Transverse thermal dispersion with Re number for 20 and 40 ceramic foam samples, a) k_{dis} / k_f , b) k_{eff} / k_f

7.3. 3D Foam Structure: Mixed Convection

Mixed convection heat transfer is important heat transfer mechanism as mixed convection may appear in many applications due to decrease of applications, low velocity and high temperature difference may appear. For this reason, analyzing mixed convection requires separate attention. Similar with the forced convection studies, interfacial convective heat transfer coefficient and thermal dispersion are evaluated and reported in this sub-heading. The same domain with forced convection is considered except gravity acts in $-y$ direction as shown in Figure 7.33. Two aluminum metal foam samples with 10 and 20 PPI are investigated for a comparison with forced convection regime. The melting point of the foam material is the only limit for this investigation where temperature difference cannot be increased too much. Also, due to the small characteristic length and low velocity requirement of mixed convection, Re number cannot be increased significantly. For this reason, no big chance can be observed with mixed convection heat transfer parameters using stochastic porous media (i.e. foam structures).

Figure 7.34 shows the change of Nu number when $Re = 30$ is shown for 10 and 20 PPI metal foam samples. As it is, there is no notable change in Nu number with Ri number when $Re = 30$, $Ri = 8.3$. As Re number is low, the effect of convection is not high and conduction is dominant in the domain. Compared to the forced convection case when $Re = 30$, such as $Ri = 0.0001$, an increase in Nu number can be expected by increasing Ri number. However, under mixed convection regime, comparable results with forced convection studies are observed. Figure 7.34 shows that, Re is a key parameter for heat transfer enhancement in mixed convection studies. Even though Gr number is an important parameter for mixed convection, a significant increase like 2D cases are not possible with foam structures when Re is low. Due to low characteristic length of foam structures, increasing Re number to the highest value in this study (i.e. $Re = 600$) even when $Ri = 1.4$ is not possible as solid temperature is required to be higher than the melting point of aluminum; as melting temperature of aluminum is around 900 K.

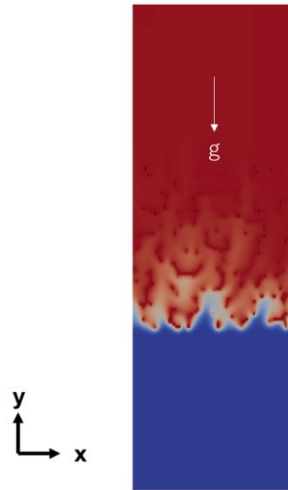


Figure 7.33. The domain considered in mixed convection case

The change of effective thermal conductivity seen in Figure 7.35 shows a similar behavior with interfacial convective heat transfer coefficient where forced and mixed convection results are very close. This might be due to the fact that it is not possible to increase solid temperature too high values when Re is high.

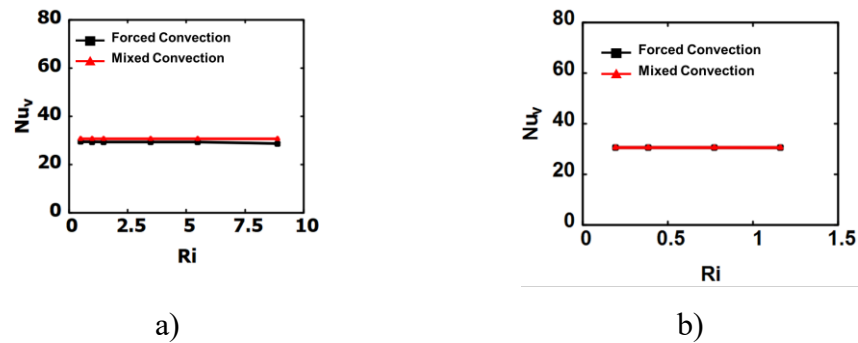


Figure 7.34. The change of Nu number with Ri number when Re = 30; a) 10 PPI aluminum foam, b) 20 PPI aluminum foam

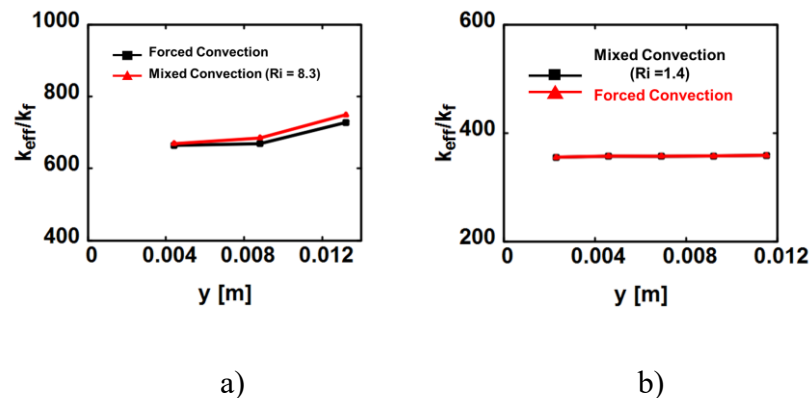


Figure 7.35. The change of effective thermal conductivity when Re = 30; a) 10 PPI aluminum foam, Ri = 8.3, b) 20 PPI aluminum foam, Ri = 1.4

The velocity and temperature profiles at the mid of foam samples can be seen in Figure 7.36. As it is seen that, temperature and velocity slightly increases under mixed convection, as expected. However, the behavior of the profiles is same with forced convection case as the dimension of the pores are small and there is not enough space for the occurrence of flow reversals. That is why; there is no meaningful change in Nusselt number and thermal dispersion value.

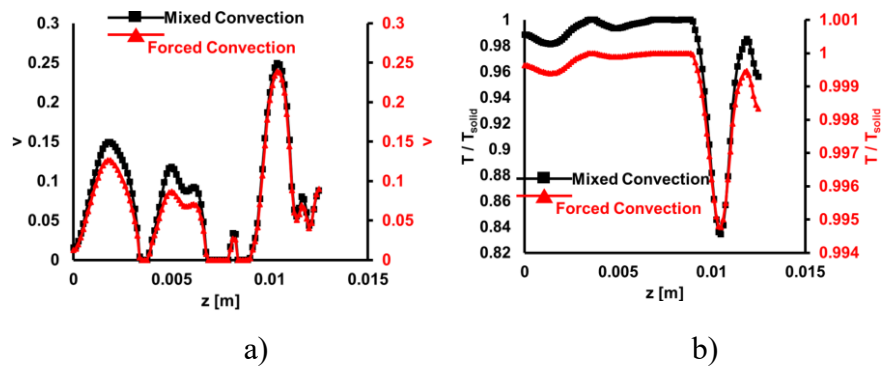


Figure 7.36. The change velocity and temperature at the mid of the foam when $Re = 30$, 10 PPI aluminum foam and $Ri = 8.3$, a) velocity profiles, b) temperature profiles

Similar behavior shown in above figures with aluminum samples is also observed with ceramic samples. For this reason, current structures of foams may not be a suitable candidate for mixed convection heat transfer enhancement due to their small characteristic length, viscous forces dominate very quickly (low Re) which does not allow increasing temperature difference term in Grashof number. Decreasing Re number might increase Ri number, when Gr is constant. However, when the velocity is too low, the temperature at every point inside pores are getting very close to each other due to high thermal conductivity of solid phase.

CHAPTER 8

CONCLUSION

In this thesis, volume-averaged transport parameters of a periodic 2D and stochastic 3D foam structures for both forced and mixed convection heat transfer are determined computationally by using volume-averaging method. The pore scale governing equations are presented and theory of volume average is explained in detail. For each domain, the governing equations are solved and based on the obtained velocity, pressure and temperature distributions, the volume-averaged transport parameters which are interfacial heat transfer and thermal dispersion coefficients for period structure and permeability, inertia, interfacial and thermal dispersion coefficients for aluminum and ceramic foams are calculated. Based on the obtained results, following remarks can be concluded:

For interfacial convective heat transfer coefficient of 2D periodic structure under mixed convection:

The effects of Ri , Re and ε on the interfacial heat transfer coefficient are analyzed. The study is performed for $100 < Re < 500$, $0.1 < Ri < 10$, $0.51 < \varepsilon < 0.96$ and based on the obtained results following conclusion can be presented:

- a) The influence of the surface parallel to flow is higher for the porous media with low values of porosity (i.e. $\varepsilon = 0.51$). For porous media with high porosity, Re and Ri numbers ($\varepsilon = 0.96$, $Re=500$, $Ri = 10$) a secondary flow occurs on the surface parallel to flow and bottom surface of the rod plays vital role on the interfacial heat transfer coefficient.
- b) For low porosity values (i.e. $\varepsilon = 0.51$), the mean interfacial Nusselt number does not change significantly with Ri or Re numbers. The rate of increase of mean interfacial convective heat transfer coefficient for a

porous medium with $\varepsilon = 0.51$ and $Re = 100$, when Ri increases from 0.01 to 10 is only 0.64%.

- c) For the porous media with high values of porosity (i.e., $\varepsilon = 0.96$), the interfacial convective heat transfer coefficient considerably improves with increase of Ri number. However, the rate of increase depends on Re number. For a porous medium with high porosity values, secondary flows occur in the main channel between rods when Ri value is high (i.e. $Ri = 10$) and this enhances heat transfer rate. For a porous medium with $\varepsilon = 0.96$ and $Re = 500$, the value of mean interfacial convective heat transfer coefficient improves by 72% when Ri changes from 0.01 to 10.
- d) The available correlations employed for determination of interfacial heat transfer coefficient for forced convection can be used for mixed convection for low porosity (such as $\varepsilon = 0.51$) even for high Re and Ri numbers. However, those correlations are not valid for porous media with high porosity values (such as $\varepsilon = 0.96$) and Ri numbers ($Ri = 10$).

For thermal dispersion conductivity of 2D periodic structure under mixed convection:

Like the interfacial heat transfer coefficient, the longitudinal thermal dispersion is attempted to be calculated for $100 < Re < 500$, $0.1 < Ri < 4$, $0.51 < \varepsilon < 0.96$. Unfortunately, the obtained results were very surprising. To ensure of the results many runs were performed, however the same results were obtained. The conclusion of this part of study can be written as follow:

- a) The volume averaging technique fails for the cases with high Ri number and it may not be applied for those kinds of problems. There are many reported studies consider volume-averaged governing equations for mixed convection problems even with high Ri number, in the literature. However, the present thesis shows that those results might be questionable.
- b) For low Ri number ($Ri = 0.1$) there is no problem with the velocity and temperature profiles are very like the forced convection and consequently the obtained values are positive which are expected values. For high values

of Ri number ($Ri=4$), the velocity profile completely changes and this causes appearing of negative thermal dispersion and consequently effective thermal conductivity. Based on the second law of thermodynamic the value of effective thermal conductivity should be positive and negative thermal conductivity concept is against of the second law of thermodynamics.

c) Longitudinal thermal dispersion increases by Re number when $Ri = 0.1$. However, by increasing Ri number to high values (i.e. $Ri = 4$), longitudinal thermal dispersion may decrease to lower values than the values when $Re = 100$.

d) For low values of Ri (e.g. $Ri= 0.1$) number the direction of the macroscopic (volume averaged) flow and real flow are same. Fluid flows from the bottom of the channel and goes up. However, for high values of Ri number ($Ri = 4$), the inlet of flow from the top of the channel exits however this reverse flow cannot resemble by the volume average method. The flowing of reverse flow at lower temperature causes the effective thermal conductivity to become negative since it reduces the propagation of heat in flow direction.

For permeability and inertia coefficient of stochastic porous media:

In this study, the tomography technique is used to calculate permeability and inertia coefficient of two kinds of foams, which are ceramic and metal foam structures with 10 and 20 PPI. The values of permeability and inertia coefficient for foam structures were found computationally by using micro-tomography images. After solving the continuity and momentum equations for the voids inside the metal foam, the volume average technique is applied and the values of those transport parameters are found according to Darcy extended Forchheimer equation. The calculation method of these parameters is explained in detail. The study is performed for air and Re number from 0.01 to 600. Based on the obtained results following conclusion can be written:

- a) One of the aims of this section is to focus on the techniques can be employed to check the accuracy of the obtained results and to inspect the

long computational process. In addition to the traditional checks such as grid independency, comparison of results with available results in literature and image reduction check, significant inspections for the accuracy of the computational process are suggested and discussed. The suggested computational process inspection can be listed as:

- The numbers of voxels (or mesh) in the narrowest throat must be sufficiently high to simulate the flow well enough.
- Fully developed flow condition must be checked to ensure that the application of Darcy or Darcy-Forchheimer equation is valid.
- Calculations for both Darcy and non-Darcy regions should be done to catch any computational mistake and find accurate coefficients from dimensionless Darcy – Forchheimer line.
- Mesh scale must be fine enough near the walls so that the transverse velocity gradient is resolved well in the pores.
- Conservation of mass must be checked one-way or other. The simplest way to do this is to look at if the flow rate stays the same though the flow direction.

- b) There is no doubt that by improving computer and software technology, smaller voxels can be used and no need for elimination of images and more accurate results can be achieved. Furthermore, computation can be done for larger samples to reduce the possible directional errors.
- c) The obtained values for permeability and inertia coefficient are compared with available experimental results in literature and a good agreement between the obtained values and reported experimental values were observed.

For interfacial convective heat transfer coefficient and thermal dispersion coefficient of stochastic porous media:

The generated 3D digital structure of metal foam and ceramic foams are used to calculate interfacial heat transfer coefficient and longitudinal and transverse thermal conductivity. Following remarks can be concluded:

- a) The obtained results for interfacial heat transfer coefficient are compared with the equation of Calmidi and Mahajan (2000). An acceptable agreement between the obtained results and their suggested correlation has been observed. This result shows that micro-tomography method can be a suitable alternative of experimental studies to obtain volume-averaged transport parameters.
- b) By increasing Re number, convective heat transfer effect starts to increase and consequently, interfacial convective heat transfer coefficient increases with Re number. Furthermore, by increasing pore density from 10 to 20 PPI, surface area increases and surface area increases. This causes increase in interfacial convective heat transfer coefficient. Highest interfacial convective heat transfer coefficient is observed with 40 PPI pore density.
- c) To obtain high Ri numbers for 3D foam structures under mixed convection heat transfer is not practical as when $Re = 100$ or higher, temperature difference in Gr number may increase more than the melting point of foam structure. For this reason, it is not possible to have big temperature difference between solid and fluid phases. What is more, as the characteristic length of foam structures are low, there is not enough space for flow reversals to appear. Therefore, almost same results with forced convection cases are obtained under mixed convection for 3D foam structures.
- d) Transverse thermal dispersion is very low compared to longitudinal thermal dispersion.
- e) Similar with interfacial convective heat transfer coefficient, for both longitudinal and transverse thermal dispersion values are validated with the studies of Zhang et al. (2015). Therefore, it is shown that to obtain interfacial convective heat transfer coefficient and thermal dispersion using micro-tomography method is easier and cheaper compared to experimental studies.

Difficulties in the present study:

For 3D foam structures, processing high number of images is very challenging process due to need of high amount of random access memory (RAM). Even though rapid increase of imaging techniques, scanning big samples is not easy process. Considering more number of images in flow direction increases the required RAM gradually. For this reason, REV selection should be considered. Nearly three months were spent on deciding computational fluid dynamics (CFD) solver. Much commercial software is tried and mostly had difficulties in importing the domain into CFD solver. OpenFOAM has tools to import generated 3D foam domain. As shown in Chapter 7, number of sub-volumes may change the results. It should also be noted that CFD analysis of 3D structures requires high amount of central processing unit (CPU) and RAM. Melting point of foam samples is another limit for foam samples to include buoyancy effects under mixed convection.

Suggestions for future study:

As a future study, even though the present study is validated with forced convection reported studies, experimental analysis is required to validate present numerical results. Secondly, determination of thermal dispersion under mixed convection for 2D porous structures is very challenging as flow entrance to the domain from the exit of the channel may not be represented correctly mathematically as thermal dispersion becomes negative when $Ri = 4$, $Re = 500$ and $\varepsilon = 0.96$. Also, mixed convection flow under mixed convection for 3D foam structures can be analyzed further to include buoyancy effects.

There is no doubt that the height of the porous medium has an important effect on the interfacial heat transfer coefficient when the buoyancy effect is considerable. For further study, the effect of height of channel and Pr number on the trend of change of interfacial heat transfer coefficient should be investigated.

REFERENCES

- AKOLKAR, A. & PETRASCH, J. 2012. Tomography-based characterization and optimization of fluid flow through porous media. *Transport in porous media*, 1-16.
- ALSHARE, A., STRYKOWSKI, P. & SIMON, T. 2010. Modeling of unsteady and steady fluid flow, heat transfer and dispersion in porous media using unit cell scale. *International Journal of Heat and Mass Transfer*, 53, 2294-2310.
- AMBROSIO, G., BIANCO, N., CHIU, W. K., IASIELLO, M., NASO, V. & OLIVIERO, M. 2016. The effect of open-cell metal foams strut shape on convection heat transfer and pressure drop. *Applied Thermal Engineering*, 103, 333-343.
- CALMIDI, V. & MAHAJAN, R. 1999. The effective thermal conductivity of high porosity fibrous metal foams. *Journal of Heat Transfer*, 121, 466-471.
- CALMIDI, V. & MAHAJAN, R. 2000. Forced convection in high porosity metal foams. *Transactions-American Society Of Mechanical Engineers Journal Of Heat Transfer*, 122, 557-565.
- DARCY, H. P. G. 1856. *Dètermination des lois d'ècoulement de l'eau à travers le sable*.
- DELLA TORRE, A., MONTENEGRO, G., TABOR, G. & WEARS, M. 2014. CFD characterization of flow regimes inside open cell foam substrates. *International Journal of Heat and Fluid Flow*, 50, 72-82.
- DIANI, A., BODLA, K. K., ROSSETTO, L. & GARIMELLA, S. V. 2015. Numerical investigation of pressure drop and heat transfer through reconstructed metal foams and comparison against experiments. *International Journal of Heat and Mass Transfer*, 88, 508-515.
- FORCHHEIMER, P. 1901. Wasserbewegung durch boden. *Z. Ver. Deutsch. Ing.*, 45, 1788.
- GAMRAT, G., FAVRE-MARINET, M. & LE PERSON, S. 2008. Numerical study of heat transfer over banks of rods in small Reynolds number cross-flow. *International Journal of Heat and Mass Transfer*, 51, 853-864.
- JEONG, N., CHOI, D. H. & LIN, C.-L. 2006. Prediction of Darcy–Forchheimer drag for micro-porous structures of complex geometry using the lattice Boltzmann method. *Journal of Micromechanics and Microengineering*, 16, 2240.
- KUWAHARA, F. & NAKAYAMA, A. 1999. Numerical determination of thermal dispersion coefficients using a periodic porous structure. *Journal of Heat Transfer*, 121, 160-163.

- KUWAHARA, F., NAKAYAMA, A. & KOYAMA, H. 1996. A numerical study of thermal dispersion in porous media. *Transactions-American Society of Mechanical Engineers Journal of Heat Transfer*, 118, 756-761.
- KUWAHARA, F., SHIROTA, M. & NAKAYAMA, A. 2001. A numerical study of interfacial convective heat transfer coefficient in two-energy equation model for convection in porous media. *International journal of heat and mass transfer*, 44, 1153-1159.
- LU, T. J., XU, F. & WEN, T. 2015. *Thermo-Fluid Behaviour of Periodic Cellular Metals*, Springer Berlin Heidelberg.
- MAGNICO, P. 2009. Analysis of permeability and effective viscosity by CFD on isotropic and anisotropic metallic foams. *Chemical Engineering Science*, 64, 3564-3575.
- MOYNE, C., DIDIERJEAN, S., SOUTO, H. A. & DA SILVEIRA, O. 2000. Thermal dispersion in porous media: one-equation model. *International journal of heat and mass transfer*, 43, 3853-3867.
- NAKAYAMA, A. 1995. *PC-Aided Numerical Heat Transfer and Convective Flow*, Taylor & Francis.
- NAKAYAMA, A. & KUWAHARA, F. 1999. A macroscopic turbulence model for flow in a porous medium. *Transactions-American Society Of Mechanical Engineers Journal Of Fluids Engineering*, 121, 427-433.
- NAKAYAMA, A. & KUWAHARA, F. 2005. Algebraic model for thermal dispersion heat flux within porous media. *AIChE journal*, 51, 2859-2864.
- NAKAYAMA, A., KUWAHARA, F., UMEMOTO, T. & HAYASHI, T. 2002. Heat and fluid flow within an anisotropic porous medium. *Transactions-American Society Of Mechanical Engineers Journal Of Heat Transfer*, 124, 746-753.
- NIELD, D. A. & BEJAN, A. 2012. *Convection in Porous Media*, Springer New York.
- OZGUMUS, T. & MOBEDI, M. 2015. Effect of Pore to Throat Size Ratio on Interfacial Heat Transfer Coefficient of Porous Media. *Journal of Heat Transfer*, 137, 012602.
- OZGUMUS, T. & MOBEDI, M. 2016. Effect of pore to throat size ratio on thermal dispersion in porous media. *International Journal of Thermal Sciences*, 104, 135-145.
- OZGUMUS, T., MOBEDI, M., OZKOL, U. & NAKAYAMA, A. Thermal dispersion in porous media—a review on approaches in experimental studies. 6th International Advanced Technologies Symposium (IATS'11), 2011. 16-18.
- PATHAK, M. & GHIAASIAAN, S. 2011. Convective heat transfer and thermal

- dispersion during laminar pulsating flow in porous media. *International Journal of Thermal Sciences*, 50, 440-448.
- PEDRAS, M. H. & DE LEMOS, M. J. 2008. Thermal dispersion in porous media as a function of the solid–fluid conductivity ratio. *International Journal of Heat and Mass Transfer*, 51, 5359-5367.
- PETRASCH, J., MEIER, F., FRIESS, H. & STEINFELD, A. 2008. Tomography based determination of permeability, Dupuit–Forchheimer coefficient, and interfacial heat transfer coefficient in reticulate porous ceramics. *International Journal of Heat and Fluid Flow*, 29, 315-326.
- RANUT, P., NOBILE, E. & MANCINI, L. 2014. High resolution microtomography-based CFD simulation of flow and heat transfer in aluminum metal foams. *Applied thermal engineering*, 69, 230-240.
- SAADA, M. A., CHIKH, S. & CAMPO, A. 2006. Analysis of hydrodynamic and thermal dispersion in porous media by means of a local approach. *Heat and mass transfer*, 42, 995-1006.
- TERUEL, F. E. & DÍAZ, L. 2013. Calculation of the interfacial heat transfer coefficient in porous media employing numerical simulations. *International Journal of Heat and Mass Transfer*, 60, 406-412.
- VAFAI, K. & TIEN C. L., 1981. Boundary and inertia effects on flow and heat transfer in porous media. *International Journal of Heat and Mass Transfer*, 24, 195 – 203.
- VIJAY, D., GOETZE, P., WULF, R. & GROSS, U. 2015. Forced convection through open cell foams based on homogenization approach: Steady state analysis. *International Journal of Thermal Sciences*, 98, 381-394.
- VU, T., LAURIAT, G. & MANCA, O. 2014. Forced convection of air through networks of square rods or cylinders embedded in microchannels. *Microfluidics and nanofluidics*, 16, 287-304.
- WARD, J. 1964. Turbulent flow in porous media. *Journal of the Hydraulics Division*, 90, 1-12.
- XU, J., LU, T.-J., HODSON, H. P. & FLECK, N. A. 2010. Analysis of thermal dispersion in an array of parallel plates with fully-developed laminar flow. *International Journal of Heat and Fluid Flow*, 31, 57-69.
- YANG, C. & NAKAYAMA, A. 2010. A synthesis of tortuosity and dispersion in effective thermal conductivity of porous media. *International Journal of Heat and Mass Transfer*, 53, 3222-3230.
- YANG, J., WANG, Q., ZENG, M. & NAKAYAMA, A. 2010. Computational study of forced convective heat transfer in structured packed beds with spherical or ellipsoidal particles. *Chemical Engineering Science*, 65, 726-738.

- ZAFARI, M., PANJEPOUR, M., EMAMI, M. D. & MERATIAN, M. 2015. Microtomography-based numerical simulation of fluid flow and heat transfer in open cell metal foams. *Applied Thermal Engineering*, 80, 347-354.
- ZHANG, W., LI, W. & NAKAYAMA, A. 2015. An analytical consideration of steady-state forced convection within a nanofluid-saturated metal foam. *Journal of Fluid Mechanics*, 769, 590-620.

APPENDIX A

DERIVATION OF SLATTERY'S AVERAGING THEOREM

The theory behind obtaining volume averaged equations is explained in Chapter 2 in detail. Divergence theorem is required for derivation of VAM governing equations. For derivation of Slattery's Averaging Theorem (Whitaker, 1969), the general transport theorem can be written as:

$$\frac{\partial}{\partial t} \int_{V(t)} \phi dV = \int_{V(t)} \frac{\partial \phi}{\partial t} dV + \int_{A(t)} \phi \varpi \cdot ndA \quad (\text{A.1})$$

This expression shows the relationship for a volume bounded by a surface and moving with the velocity of ϖ . Now, let's consider an arbitrary point P in the porous media which is on a curve which has an arc length of s . It should be mentioned that the arbitrary point P is passing through the s curve. If a variable, ϕ , is taken and the change of ϕ with s can be expressed by using Eq. (A.1):

$$\frac{\partial}{\partial s} \int_{V_f(s)} \phi dV = \int_{V_f(s)} \frac{\partial \phi}{\partial s} dV + \int_{A(s)} \phi \frac{dr}{ds} \cdot ndA \quad (\text{A.2})$$

It should be mentioned that ϕ is explicit function of time and spatial directions (i.e. $\frac{\partial \phi}{\partial s} = 0$). Therefore, Eq. (A.2) turns into:

$$\frac{\partial}{\partial s} \int_{V_f(s)} \phi dV = \int_{A(s)} \phi \frac{dr}{ds} \cdot ndA \quad (\text{A.3})$$

If the area, $A_f(s)$, decomposed into entrance/exit and interface areas in such way:

$$A_f(s) = A_e(s) + A_{\text{int}}(s) \quad (\text{A.4})$$

And, taking $\frac{dr}{ds} \cdot n$ is zero at solid-fluid interface as it is tangent vector to the interface, Eq. (A.3) can be written by using Eq. (A.4) as:

$$\frac{\partial}{\partial s} \int_{V_f(s)} \phi dV = \int_{A_e(s)} \phi \frac{dr}{ds} \cdot ndA \quad (\text{A.5})$$

$r(s)$ can be decomposed into position reference vector, $r_0(s)$, and position vector, $p(s)$, which refers to the location of points on s curve relative to the position reference vector as:

$$r(s) = r_0(s) + p(s) \quad (\text{A.6})$$

And directional derivative of $r(s)$ can be expressed in a such way:

$$\frac{d}{ds} = \left(\frac{dr_0}{ds} \right) \cdot \nabla \quad (\text{A.7})$$

If we write Eq. (A.5) again, by using Eq. (A.6) and (A.7):

$$\frac{\partial r_0}{\partial s} \cdot \nabla \int_{V_f(s)} \phi dV = \int_{A_e(s)} \phi \frac{dr_0}{ds} \cdot ndA + \int_{A_e(s)} \phi \frac{dp}{ds} \cdot ndA \quad (\text{A.8})$$

$\frac{dr_0}{ds}$ can be taken out of the integrals as it is not a function of the limits of the integral:

$$\frac{\partial r_0}{\partial s} \cdot \left(\nabla \int_{V_f(s)} \phi dV = \int_{A_e(s)} \phi ndA \right) + \int_{A_e(s)} \phi \frac{dp}{ds} \cdot ndA \quad (\text{A.9})$$

$\frac{dp}{ds} \cdot n$ are orthogonal as $\frac{dp}{ds}$ is tangent vector:

$$\nabla \int_{V_f} \phi dV = \int_{A_e} \phi n dA \quad (\text{A.10})$$

Eq. (A.10) can be written as using Eq. (A.2) as:

$$\int_{V_f} \nabla \phi dV = \nabla \int_{V_f} \phi dV + \int_{A_{\text{int}}} \phi n dA \quad (\text{A.11})$$

By using volume-average rule:

$$\langle \phi \rangle = \frac{1}{V} \int_V \phi dV \quad (\text{A.12})$$

Eq. (A.13) can be obtained:

$$\langle \nabla \phi \rangle = \nabla \langle \phi \rangle + \frac{1}{V} \int_{A_{\text{int}}} \phi dA \quad (\text{A.13})$$

VITA

PERSONAL

Date of Birth : 29/07/1987
Place of Birth : Kocaeli, Turkey

EDUCATION

2017 İzmir Institute of Technology, Mechanical Engineering, PhD
2012 İzmir Institute of Technology, Mechanical Engineering, MSc
2010 Atatürk University, Mechanical Engineering, BSc

SCI PUBLICATIONS

- H. Celik, M. Mobedi, A. Nakayama, U. Ozkol, “A study on numerical determination of permeability and inertia coefficient of aluminum foam using X-Ray micro-tomography technique: Focus on Inspection Methods for Reliability”, *Journal of Porous Media*, 2017 (accepted)
- H. Celik, M. Mobedi, O. Manca, U. Ozkol, “Determination of interfacial convective heat transfer coefficient for mixed convection heat transfer in a two-dimensional porous media”, *International Journal of Numerical Methods for Heat and Fluid Flow*, 2017 (accepted)
- H. Celik, M. Mobedi, O. Manca, B. Buonomo, “Enhancement of Heat Transfer in Partially Heated Vertical Channel under Mixed Convection by Using Al₂O₃ Nanoparticles”, *Heat Transfer Engineering*, 2017
- B. Buonomo, H. Celik, D. Ercole, O. Manca, M. Mobedi, “Numerical simulation of latent thermal energy storage systems with aluminum foam in local thermal equilibrium”, *Renewable Energy*, 2016 (submitted)
- H. Celik, M. Mobedi, “Effect of an inserted porous layer on heat and fluid flow in a vertical channel with mixed convection”, *Thermal Science*, (2015), 19/3
- H. Celik, M. Mobedi, “Visualization of heat flow in a vertical channel with fully developed mixed convection”, *International Communications in Heat and Mass Transfer*, 39, 1253-1264 (2012)